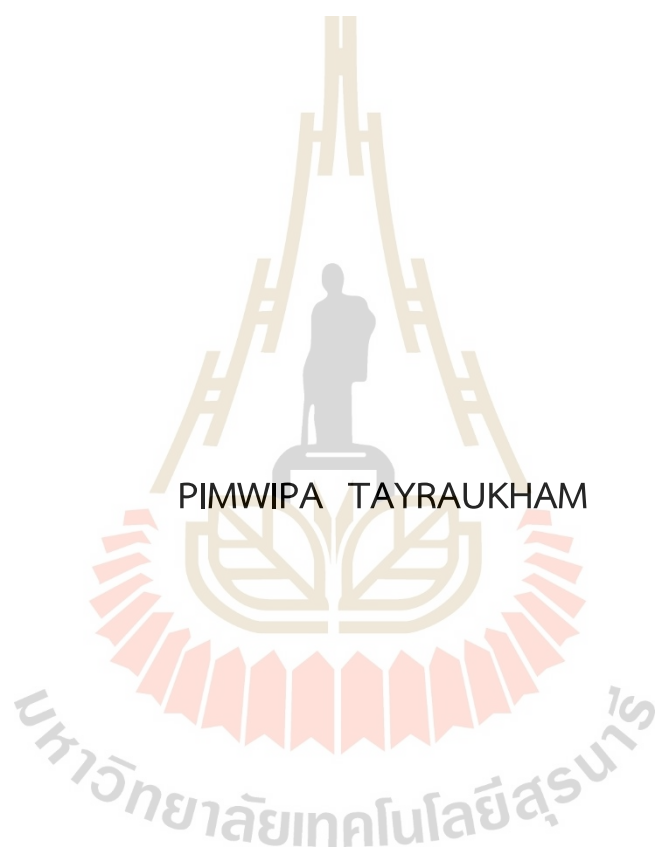


DEVELOPMENT OF HETEROGENEOUS ZEOLITE CATALYST FOR  
RENEWABLE ENERGY PRODUCTION VIA TRANSESTERIFICATION  
OF PALM OIL AND STEAM REFORMING OF ACETIC ACID



A Thesis Submitted in partial Fulfillment of the Requirements for the  
Degree of Doctor of Philosophy in Chemistry  
Suranaree University of Technology  
Academic Year 2022

การพัฒนาตัวเร่งปฏิกิริยาซีโอไลต์วิวิธพันธุ์สำหรับการผลิตพลังงานหมุนเวียน  
ผ่านทรานส์เอสเทอร์ฟิเคชันของน้ำมันปาล์มและ  
รีฟอร์มมิงด้วยไอน้ำของกรดอะซิติก



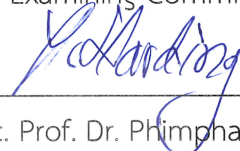
นางสาวพิมพ์วิภา ท้ายเรือคำ

วิทยานิพนธ์นี้เป็นส่วนหนึ่งของการศึกษาตามหลักสูตรปริญญาวิทยาศาสตรดุษฎีบัณฑิต  
สาขาวิชาเคมี  
มหาวิทยาลัยเทคโนโลยีสุรนารี  
ปีการศึกษา 2565

DEVELOPMENT OF HETEROGENEOUS ZEOLITE CATALYST FOR RENEWABLE  
ENERGY PRODUCTION VIA TRANSESTERIFICATION OF PALM OIL AND  
STEAM REFORMING OF ACETIC ACID

Suranaree University of Technology has approved this thesis submitted in  
partial fulfillment of the requirements for the Degree of Doctor of Philosophy.

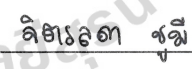
Thesis Examining Committee

  
\_\_\_\_\_  
(Assoc. Prof. Dr. Phimpaka Harding)  
Chairperson

  
\_\_\_\_\_  
(Prof. Dr. Jatuporn Wittayakun)  
Member (Thesis Advisor)

  
\_\_\_\_\_  
(Assoc. Prof. Dr. Sanchai Prayoonpokarach)  
Member (Thesis Co-Advisor)

  
\_\_\_\_\_  
(Prof. Dr. Nurak Grisdanurak)  
Member

  
\_\_\_\_\_  
(Asst. Prof. Dr. Jitlada Chumee)  
Member

  
\_\_\_\_\_  
(Assoc. Prof. Dr. Chaiwat Ruksakulpiwat)  
Member

  
\_\_\_\_\_  
(Assoc. Prof. Dr. Chatchai Jothityangkoon)  
Vice Rector for Academic Affairs  
and Quality Assurance

  
\_\_\_\_\_  
(Prof. Dr. Santi Maensiri)  
Dean of Institute of Science

พิมพ์วิภา ท้ายเรือคำ : การพัฒนาตัวเร่งปฏิกิริยาซีโอไลต์วิวิธพันธุ์สำหรับการผลิตพลังงาน  
หมุนเวียนผ่านทรานส์เอสเทอร์ิฟิเคชันของน้ำมันปาล์มและรีฟอร์มมิงด้วยไอน้ำของกรดอะซิติก  
(DEVELOPMENT OF HETEROGENEOUS ZEOLITE CATALYST FOR RENEWABLE  
ENERGY PRODUCTION VIA TRANSESTERIFICATION OF PALM OIL AND STEAM  
REFORMING OF ACETIC ACID) อาจารย์ที่ปรึกษา : ศาสตราจารย์ ดร.จตุพร วิทยาคุณ,  
103 หน้า.

คำสำคัญ: ตัวเร่งปฏิกิริยาวิวิธพันธุ์; ซีโอไลต์; ไบโอดีเซล; รีฟอร์มมิงด้วยไอน้ำของกรดอะซิติก

ปัจจุบันภาวะโลกร้อนเนื่องจากการปล่อยก๊าซเรือนกระจกเป็นปัญหาระดับนานาชาติที่ต้องเร่ง  
แก้ไข ในงานนี้ได้นำเสนอการพัฒนาตัวเร่งปฏิกิริยาซีโอไลต์วิวิธพันธุ์และการประยุกต์ใช้ในการผลิต  
พลังงานหมุนเวียนซึ่งประกอบด้วยไบโอดีเซลและไฮโดรเจนเพื่อลดผลกระทบนี้ ซึ่งจะช่วยลดการปล่อย  
ก๊าซคาร์บอนไดออกไซด์เมื่อเทียบกับเชื้อเพลิงฟอสซิล โดยไบโอดีเซลจะถูกผลิตจากน้ำมันปาล์มโดย  
กระบวนการทรานส์เอสเทอร์ิฟิเคชันที่อุณหภูมิ 60 °C บนตัวเร่งปฏิกิริยาโพแทสเซียมที่รองรับบน  
โซเดียมเอ็กซ์และโซเดียมพีทูซีโอไลต์ซึ่งเตรียมโดยวิธีทำให้เอิบซุ่ม ความมีรูพรุนสูงของตัวเร่งปฏิกิริยา  
ซีโอไลต์โซเดียมเอ็กซ์แสดงให้เห็นถึงประสิทธิภาพการเร่งปฏิกิริยาที่สูงในขณะที่ตัวเร่งปฏิกิริยาโซเดียม  
พีทู สามารถใช้เพียงพื้นผิวภายนอกเพื่อสร้างส่วนเร่งปฏิกิริยาที่เข้าจับกับสารตั้งต้น ส่งผลให้เกิดผล  
ผลิตไบโอดีเซลลดลง นอกจากนี้ยังได้ปรับปรุงความเสถียรของตัวเร่งปฏิกิริยาดังกล่าวโดยการ  
สังเคราะห์ภายใต้คลื่นไมโครเวฟซึ่งใช้เวลาในการตกผลึกสั้น วัสดุเหล่านี้สร้างชนิดคาร์บอนที่แตกต่าง  
กันซึ่งสามารถต้านทานการยุบตัวของโครงสร้างซีโอไลต์โซเดียมเอ็กซ์ได้ และนอกจากนี้ยังได้ศึกษาการ  
พัฒนาตัวเร่งปฏิกิริยา Ni/MFI ที่ต่างกันสำหรับปฏิกิริยาการปฏิรูปไอน้ำของกรดอะซิติก โดยนิกเกิลมี  
ผลกระทบอย่างมากต่อการผลิตไฮโดรเจน ในขณะที่การรองรับบนซีโอไลต์ช่วยเพิ่มการกระจายตัวของ  
โลหะ ยิ่งไปกว่านั้นการลดลงของปริมาณอลูมิเนียมและนิกเกิลส่งผลกระทบอย่างมากต่อการป้องกันการ  
เกิดผลิตภัณฑ์ที่ไม่ต้องการ การก่อดวงของถ่านโค้ก และการเผาผนึกโลหะ นอกจากนี้สภาวะของ  
ปฏิกิริยายังส่งผลต่อตัวเร่งปฏิกิริยาเช่นเดียวกัน โดยที่สภาวะไอน้ำเข้มข้น (อัตราส่วนไอน้ำต่อคาร์บอน  
เท่ากับ 5) จะสามารถกำจัดคาร์บอนที่สะสมได้ทั้งหมดที่อุณหภูมิ 700 °C หลังจากการทดสอบถึง 5  
ชั่วโมง ตัวเร่งปฏิกิริยา MFI ที่ไม่มีอลูมิเนียมสามารถสร้างผลิตภัณฑ์ด้วยอัตราที่คงที่

สาขาวิชาเคมี

ปีการศึกษา 2565

ลายมือชื่อนักศึกษา

พิมพ์วิภา ท้ายเรือคำ

ลายมือชื่ออาจารย์ที่ปรึกษา

จตุพร วิทยาคุณ

ลายมือชื่ออาจารย์ที่ปรึกษาร่วม

นพดล

PIMWIPA TAYRAUKHAM : DEVELOPMENT OF HETEROGENEOUS ZEOLITE CATALYST FOR RENEWABLE ENERGY PRODUCTION VIA TRANSESTERIFICATION OF PALM OIL AND STEAM REFORMING OF ACETIC ACID. THESIS ADVISOR : PROF. JATUPORN WITTAYAKUN, Ph.D. 103 PP.

Keyword: Heterogeneous catalyst; Zeolite; Biodiesel; Acetic acid steam reforming

Global warming due to emissions of greenhouse gases is presently an international problem that needs to solve urgently. This work presents the development of heterogeneous zeolite catalysts and applications in renewable energy production consisting of biodiesel and hydrogen to mitigate this effect by reducing carbon dioxide emissions compared with fossil fuels. Biodiesel is generated via transesterification of palm oil at 60 °C over potassium supported on NaX and NaP2 zeolite preparing by impregnation. The high porosity of NaX gives a high catalytic performance, while NaP2 catalysts can use only external surfaces to generate active specie and interact with reactants resulting in lower yield. Additionally, the stability of the catalysts is improved by microwave-assisted synthesis with a short crystallization time. These materials generate different types of carbonate that can resist the structure collapse of zeolite NaX. Moreover, the development of heterogeneous Ni/MFI catalysts for acetic acid steam reforming reactions is investigated. Nickel strongly impacts hydrogen production, while zeolite support improves metal dispersion. Moreover, decreasing aluminum and nickel loading has significant impacts on preventing the production of undesired products, coke formation, and metal sintering. In addition, reaction conditions also affect catalysts. Rich-steam condition (steam-to-carbon ratio of 5) eliminates all carbon deposition at 700 °C. After testing for five hours, a silicious MFI catalyst generates a product with a stable rate.

School of Chemistry  
Academic Year 2022

Student's Signature ปณิธิม ทวีรัตน  
Advisor's Signature อ.พร อานน  
Co-Advisor's Signature น.ส.อ.

## ACKNOWLEDGMENTS

Foremost, I would like to express my sincere thank to my thesis advisor Prof. Dr. Jatuporn Wittayakun and my thesis co-advisor Assoc. Prof. Dr. Sanchai Prayoonpokarach. I would not have achieved this far and this thesis would not have been completed without their help and constant encouragement throughout the course of this research and writing.

Additionally, I would like to thank my committee: Prof. Dr. Nurak Grisdanurak, Assoc. Prof. Dr. Phimpaka Harding, Assoc. Prof. Dr. Chaiwat Ruksakulpiwat and Asst. Prof. Dr. Jitlada Chumee, for their insightful comments.

For my overseas research experience, I would like to thank Prof. Dr. Teruoki Tago, Tago lab members, and the Department of Chemical Science and Engineering, Tokyo Institute of Technology, for giving me the opportunity to conduct research of my interest.

Importantly, I appreciate the financial support from the Science Achievement Scholarship of Thailand (SAST), Ministry of Higher Education, Science, Research and Innovation, and Suranaree University of Technology.

I am so grateful to JW&SP research group members for suggestion and helps in the research, especially Mr. Nawe Jantarit for working together in the biodiesel part. I would like to thank my friends, my family, and Ms. Pailin Suwannatri for their encouragement and support.

Last but not least, this thesis is dedicated to my mother for her endless love and overwhelming encouragement.

Pimwipa Tayraukham

# CONTENTS

	Page
ABSTRACT IN THAI .....	I
ABSTRACT IN ENGLISH .....	II
ACKNOWLEDGMENTS .....	III
CONTENTS .....	IV
LIST OF TABLES .....	VII
LIST OF FIGURES .....	IX
LIST OF ABBREVIATIONS AND SYMBOLS .....	XIII
<b>CHAPTER</b>	
<b>I INTRODUCTION .....</b>	<b>1</b>
<b>II LITERATURE REVIEW .....</b>	<b>3</b>
2.1 Renewable energy .....	3
2.2 Transesterification of palm oil .....	4
2.3 Catalyst for transesterification of palm oil.....	5
2.3.1 Conventional and microwave-assisted zeolite crystallization .....	7
2.3.2 Synthesis of NaP2 zeolite from CH and MH methods .....	8
2.4 Acetic acid steam reforming.....	12
2.5 Catalyst for acetic acid steam reforming.....	13
2.6 References.....	15
<b>III SYNTHESIS OF PURE PHASE NAP2 ZEOLITE FROM THE GEL OF SODIUM Y BY CONVENTIONAL AND MICROWAVE-ASSISTED HYDROTHERMAL METHODS.....</b>	<b>22</b>
3.1 Abstract .....	22
3.2 Introduction.....	22
3.3 Materials and Methods.....	24
3.3.1 Materials.....	24
3.3.2 Preparation of Zeolite Synthesis Gel.....	24

## CONTENTS (Continued)

	Page
3.3.3 Single Crystallization .....	25
3.3.4 Double Crystallization via MH Method .....	25
3.3.5 Characterization of Solid Products.....	26
3.4 Results and Discussion.....	26
3.4.1 Comparison of Conventional and Microwave-Assisted Hydrothermal Methods of Single Crystallization .....	26
3.4.2 Effect of Temperature and Time on Single Crystallization by Microwave-Assisted Hydrothermal Methods .....	29
3.4.3 Effect of Double Crystallization by Microwave-Assisted Hydrothermal Methods.....	31
3.5 Conclusion.....	35
3.6 References .....	36
<b>IV BIODIESEL PRODUCTION VIA TRANSESTERIFICATION OF PALM OIL OVER POTASSIUM CATALYSTS SUPPORTED ON ZEOLITE SODIUM X AND P2 FROM CONVENTIONAL AND MICROWAVE-ASSISTED HYDROTHERMAL METHODS.....</b>	<b>41</b>
4.1 Abstract.....	41
4.2 Introduction.....	42
4.3 Materials and Methods.....	43
4.3.1 Chemicals.....	43
4.3.2 Synthesis of NaX supports via CH and MH .....	44
4.3.3 Preparation of potassium catalysts .....	44
4.3.4 Catalyst characterization.....	45
4.3.5 Transesterification reaction .....	46
4.4 Results and Discussion .....	47
4.4.1 Catalyst characterizations.....	47
4.4.2 Determination of basicity and textural parameters of the catalysts.	55
4.4.3 Catalytic performance via transesterification of palm oil.....	57

## CONTENTS (Continued)

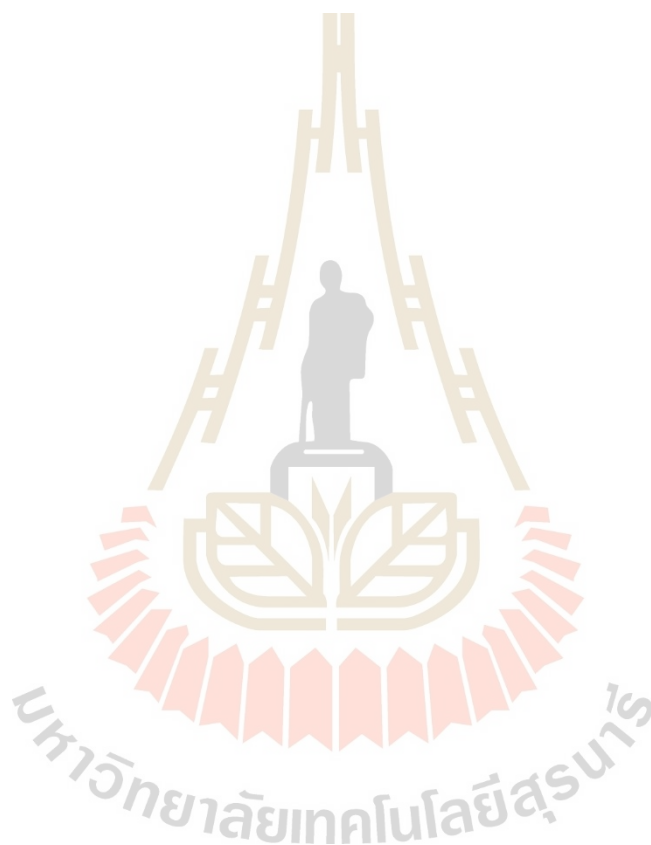
	Page
4.5 Conclusions .....	61
4.6 References .....	62
<b>V HYDROGEN PRODUCTION VIA ACETIC ACID STEAM REFORMING OVER NICKEL SUPPORTED ON MFI CATALYST .....</b>	<b>65</b>
5.1 Abstract .....	65
5.2 Introduction .....	65
5.3 Material synthesis .....	67
5.3.1 Chemicals .....	67
5.3.2 Synthesis of MFI zeolites with different Si/Al ratio .....	67
5.3.3 Ni/MFI zeolite catalysts preparation .....	68
5.3.4 Material characterizations .....	68
5.4 Catalytic testing via Acetic acid steam reforming reaction (AASR) .....	69
5.5 Results and Discussion .....	72
5.5.1 Effect of 5Ni/MFI with different Al content in zeolite .....	72
5.5.2 Effect of Ni weight .....	88
5.6 Conclusion .....	93
5.7 References .....	93
<b>VI CONCLUSIONS .....</b>	<b>97</b>
APPENDIX .....	99
CURRICULUM VITAE .....	103

## LIST OF TABLES

<b>Table</b>		<b>Page</b>
2.1	Gel composition and synthesis parameters of zeolite P from the literature ...	10
3.1	Gel composition and synthesis parameters of zeolite P from the literature ...	23
3.2	Band assignment of FTIR spectra of MH90 (FAU) and MH90A150 (GIS) samples.....	33
3.3	Gel composition, synthesis parameters and phase of the products in this study.....	35
4.1	Relative crystallinity of the potassium catalysts .....	49
4.2	Vibration modes and peak assignments of Zeolite X, Zeolite P2, H <sub>2</sub> O, and K <sub>2</sub> CO <sub>3</sub> .....	52
4.3	Basicity and textural parameters of all catalysts from CO <sub>2</sub> -TPD and N <sub>2</sub> sorption analysis, respectively .....	57
4.4	Retention time, type of methyl ester, number of carbon atoms in each product, and certified value of the mixed standard.....	59
4.5	Comparison of catalytic performance and conditions of the current work with the literature.....	61
5.1	Si/Al ratio and Ni loading of Ni/MFI catalysts.....	72
5.2	Wavenumber and vibration of functional group in catalysts from Figure 5.3..	73
5.3	Crystalline size, diameter, and spherical volume of Ni nanoparticles in Ni/MFI catalysts .....	75
5.4	Surface area and micropore volume of Ni/MFI catalysts.....	79
5.5	Diameter and spherical volume of Ni nano particles in fresh and spent Ni/MFI catalysts with different S/C ratios of reaction condition at 700 °C .....	87
5.6	Ni loading Si/Ni molar ratio, and Ni particle diameter of 1Ni/S-1 and 5Ni/S-1 catalysts.....	88
5.7	Surface area and micropore volume of 5Ni/S-1 and 1Ni/S-1 from N <sub>2</sub> adsorption-desorption.....	89

## LIST OF TABLES (Continued)

Table	Page
5.8 Ni particle diameter in fresh and spent 5Ni/S-1, 1Ni/S-1 catalysts .....	93
A-1 Stoichiometric coefficient, enthalpy change ( $\Delta H$ ), Gibbs free energy ( $\Delta G$ ), entropy change ( $\Delta S$ ), and Heat capacity ( $C_p$ ).....	102



## LIST OF FIGURES

Figure	Page
2.1	Transesterification reaction for methyl ester (biodiesel) production .....5
2.2	Fujasite (FAU) and gismodine (GIS) porous structure of NaX and NaP2, respectively .....6
2.3	The temperature profiles as function with times (left) and modeling of gradient temperature after heating for 1 min (right) in microwave irradiation versus oil bath .....8
2.4	Building units of GIS structure.....8
2.5	The slightly different plane structure of zeolite P1 and P2 from the distorted rotation of 4-MR in the GIS framework.....9
2.6	Reaction pathway of AASR ..... 12
3.1	Powder X-ray diffraction (XRD) patterns of zeolite products from conventional and microwave-assisted hydrothermal methods with single crystallization at 150 °C for 24 hours (CH150) and 1 hour (MH150)..... 27
3.2	A field emission scanning electron microscopy (FESEM) images of the zeolite products from conventional and microwave-assisted hydrothermal methods with single crystallization at 150 °C for 24 hours (CH150) and 1 hour (MH150)..... 28
3.3	Powder XRD patterns of zeolites from single crystallization via MH (a) for 1 hour at 90 °C, 150 °C and 175 °C, (b) at 175 °C, and (c) 150 °C for various times:15, 30, 45 and 60 minutes. .... 30
3.4	FESEM images of zeolite products from microwave-assisted hydrothermal methods with single crystallization at 150 °C for various times: (a) 15, (b) 30, (c) 45 and (d) 60 minutes ..... 31
3.5	XRD patterns of zeolites from microwave-assisted hydrothermal method at 90 °C for 1 hour (MH90), aged at room temperature for 23 hours (MH90A) and crystallized at 150 °C for 1 hour (MH90A150)..... 32

## LIST OF FIGURES (Continued)

Figure	Page
3.6	Fourier-transform infrared spectroscopy (FTIR)–attenuated total reflectance (ATR) spectra of zeolite products: MH90 from the microwave-assisted hydrothermal method at 90 °C for 1 hour and MH90A150 from the microwave-assisted hydrothermal method at 90 °C for 1 hour followed by aging at room temperature for 23 hours and recrystallization at 150 °C for 1 hour..... 32
3.7	FESEM images of zeolites from the microwave-assisted hydrothermal method (a) at 90 °C for 1 hour (MH90), followed by aging at room temperature for 23 hours and recrystallized (b) at 150 °C for 1 hour (MH90A150)..... 34
3.8	Powder XRD patterns of NaP2 zeolites from microwave-assisted double crystallization for repetition at the first time (MH90A150–1) and the second time (MH90A150–2)..... 34
4.1	XRD patterns fresh and spent (S) catalysts on zeolite NaX from (a) CH and (b) MH methods, and (c) zeolite NaP2..... 48
4.2	FTIR-ATR spectra of (a) the bare NaX zeolite, the potassium catalyst of zeolite NaX in a range of (b) 1300-350 cm <sup>-1</sup> , (c) 1800-1200 cm <sup>-1</sup> , and related catalyst of zeolite NaP2 in a range of (d) 1300-350 cm <sup>-1</sup> , (e) 1800-1200 cm <sup>-1</sup> ..... 51
4.3	SEM images of (a) CHX, (b) CHX-U, (c) MHX, (d) MHX-U, (e) K/CHX, (f) K/CHX-U, (g) K/MHX, and (h) K/MHX-U. .... 54
4.4	SEM images of (a) CHP2, (b) MHP2, (c) K/CHP2, (d) K/MHP2 and energy dispersive X-ray spectroscopy (EDS) of (e) K/CHP2, (f) K/MHP2..... 55
4.5	CO <sub>2</sub> TPD curves of K-impregnated NaX catalysts..... 56
4.6	GC chromatogram of (a) hexane, (b) standard of mixed methyl esters, and (c) biodiesel product over potassium catalyst operating at 60 °C for 3 h ..... 58
4.7	Biodiesel yields from catalysts based (a) NaX and (b) NaP2 operating at 60 °C for 3 h ..... 60

## LIST OF FIGURES (Continued)

Figure	Page
5.1 AASR setup: (1) Feed injector: flow acetic acid solution into the flow reactor, (2) Gas tank, (3) Gas valve: open and close gas from tank, (4) Flow meter: setting gas flow rate, (5) Gas line <sub>(in)</sub> : flowing N <sub>2</sub> as carrier gas into flow reactor, (6) Heater: heating all of gas line to 120 °C, (7) Heater: heating of flow reactor, (8) Flow reactor: the quartz tube containing catalyst inside the reactor, (9) GC-FID: analysis of hydrocarbon chemicals, (10) Gas line <sub>(out)</sub> : flowing mixed gas from reactor to analysis part, (11) GC-TCD: analysis of small gas molecules, (12) Start button: button for starting the analysis and data collecting, (13) Computer: processing system.....	69
5.2 Catalytic processing and temperature program of AASR .....	70
5.3 Fourier transform infrared (FTIR) spectra at wide range of (a) S-1, Z50 zeolite supports, and (b) 5Ni/S-1, 5Ni/Z100, 5Ni/Z50 catalysts, and (c-e) narrow range .....	74
5.4 Powder X-Ray diffraction (XRD) patterns of silicalite-1 zeolite and 5Ni/S-1, 5Ni/Z100, 5Ni/Z50 catalysts with different 2 theta: (a) 5-80, and (b) 35-80 degree.....	75
5.5 Transmission electron microscopy (TEM) images of 5Ni/MFI catalysts with different Si/Al in support: (a-d) 5Ni/S-1, (b, e) 5Ni/Z100, (c, f) 5Ni/Z50 .....	77
5.6 The model for the hypothetical distribution of nickel in different polarity zeolites, including 5Ni/Z50, 5Ni/Z100, and 5Ni/S-1 .....	77
5.7 Nitrogen adsorption (ads)-desorption (des) (a) isotherm and (b) hysteresis loop of 5Ni/S-1, 5Ni/Z100, 5Ni/Z50 catalysts .....	78
5.8 H <sub>2</sub> -temperature programmed reduction (H <sub>2</sub> -TPR) profiles of 5Ni/S-1, 5Ni/Z100, 5Ni/Z50 catalysts .....	80
5.9 GC chromatogram with (a) TCD and (b) FID detector over S-1, Z50, 5Ni/S-1, 5Ni/Z100, and 5Ni/Z200 catalysts with reaction condition about 700 °C, 1h, S/C ratio: 5.....	81

## LIST OF FIGURES (Continued)

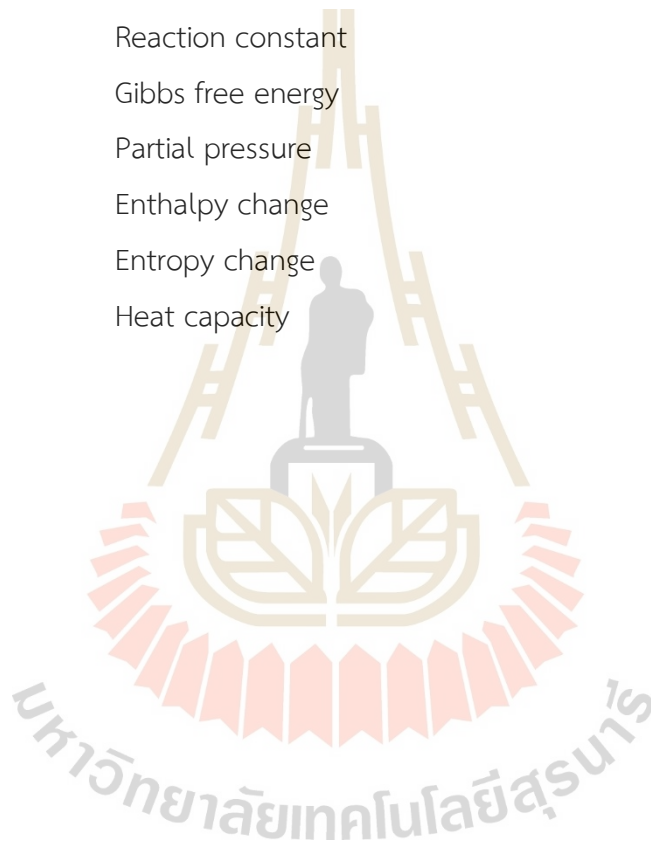
Figure	Page
5.10 %Acetic acid (AcOH) conversion, % C-yield over (a) S-1, (b) Z50 catalysts, and (c) % H <sub>2</sub> -yield over S-1, and Z50 with reaction condition about 700 °C, 1-5 h, S/C ratio: 5, and (d) carbon deposition on spent catalysts from TGA analysis .....	83
5.11 (a) % CO <sub>2</sub> -yield, (b) % CO-yield, (c) % H <sub>2</sub> -yield, (d-e) % CH <sub>4</sub> -yield, and (f) % C <sub>2</sub> H <sub>6</sub> -yield and the products at thermodynamic equilibrium (----) with different S/C ratio of (5), (3) over 5Ni/S-1, 5Ni/Z100, and 5Ni/Z200 catalysts after testing at 700 °C, 1h .....	84
5.12 (a) Thermogravimetric analysis (TGA) with different S/C ratio of (5), (3) and (b) carbon deposition on spent catalysts after testing at 700 °C, 1h .....	85
5.13 TEM images of (a-c) fresh and spent catalyst after testing with S/C ratio about (d-f) 5, (g-i) 3 at 700 °C, 1h .....	86
5.14 Powder XRD patterns of silicalite-1 zeolite, 5Ni/MFI, and 1Ni/MFI catalysts ...	88
5.15 Nitrogen adsorption (ads) -desorption (des) isotherm of 5Ni/S-1, 1Ni/S-1 catalysts .....	89
5.16 H <sub>2</sub> -TPR profiles of 5Ni/S-1 and 1Ni/S-1 catalysts.....	90
5.17 (a-b) % C-yield, (c-d) % H-yield over 5Ni/S-1, 1Ni/S-1 catalysts at 700 °C, 1h, S/C: 5, with different reaction time and the products at thermodynamic equilibrium (Eq).....	91
5.18 TEM images of (a-b) fresh and (c-d) spent 5Ni/S-1, 1Ni/S-1 catalysts after testing with S/C ratio: 5, at 700 °C, 1h .....	92
A-1 standard calibration curve of (a) hydrogen, (b) carbon dioxide, (c) carbon monoxide, and (d) methane. ....	100

## LIST OF ABBREVIATIONS AND SYMBOLS

NaX	Zeolite X in sodium form
NaP2	Zeolite P2 in sodium form
FAU	Faujasite structure of zeolite
GIS	Gismodine structure of zeolite
MFI	Mobil-type five structure of zeolite
SDA	Structure directing agent
CH	Conventional hydrothermal
MH	Microwave-assisted hydrothermal
Si/Al	Silicon-to-alumina atomic ratio
XRD	X-ray diffraction
XRF	X-ray fluorescence analysis
FTIR	Fourier-transform infrared spectroscopy
TEM	Transmission Electron Microscope
SEM/EDS	Scanning Electron Microscope/ Energy Dispersive X-ray Spectroscopy
TGA	Thermogravimetric analysis
CO <sub>2</sub> -TPD	CO <sub>2</sub> -temperature-programmed desorption
H <sub>2</sub> -TPR	Temperature-programmed reduction with hydrogen
GC	Gas chromatography
TCD	Thermal conductivity detector
FID	Flame Ionization Detector
C <sub>2</sub>	Hydrocarbon product with two carbon atoms
C <sub>ester</sub>	Mass concentration of methyl ester
$\rho_{oil}$	Density of the reactant palm oil
$\nu$	FTIR vibration with stretching mode
$\nu_{as}$	FTIR vibration with asymmetric stretching mode
$\nu_s$	FTIR vibration with symmetric stretching mode

## LIST OF ABBREVIATIONS AND SYMBOLS (Continued)

$\delta$	FTIR vibration with bending mode
S/C	Steam-to-carbon ratio
W/F	Catalyst weight-to-acetic acid flow rate ratio
GHSV	Gas hourly space velocity
$F_i$	Molar flow rates of component i
K	Reaction constant
$\Delta G_R$	Gibbs free energy
$p$	Partial pressure
$\Delta H$	Enthalpy change
$\Delta S$	Entropy change
$C_p$	Heat capacity



# CHAPTER I

## INTRODUCTION

This thesis has six chapters; the main research works are in Chapter III, IV and V. Chapters I and II provide an overview and literature review of Chapters III, IV and V. Finally, chapter VI summarizes the conclusions from each part. The work in Chapter III aims to synthesize the pure phase of NaP2 zeolite from NaY gel by conventional hydrothermal (CH) and microwave-assisted hydrothermal (MH) methods with a shorter crystallization time. Zeolite NaP2 was synthesized by adapting the NaY zeolite synthesis method developed by Ginter (2001). The NaY gel was subjected to crystallization by CH and MH. The synthesis conditions such as temperatures, durations, and crystallization steps were optimized. The goal was to achieve a rapid synthesis of NaP2 zeolite with a high crystallinity. The crystallization time of the optimized method was compared to the standard approach (Robson and Lillerud, 2001).

Chapter IV deals with the application of NaP2, synthesized from CH and MH from Chapter III, in the transesterification of palm oil. NaP2 zeolite was used as support for potassium catalysts which were prepared by impregnation as described by Rakmae et al. (2016). As NaP2 and NaX zeolites have different pore sizes and structures, the obtained catalysts (K/NaP) were compared with K/NaX in terms of stability and catalytic performance. The testing conditions were similar to the previous work by Kosawatthanakun et al. (2022).

Chapter V studies Ni supported on MFI, another type of zeolite in acetic acid steam reforming (AASR). The Ni/MFI catalysts were prepared by impregnation method as described by Y. Zhang et al. (2023). The goals were to improve Ni particle dispersion, minimize carbon deposition, and prevent by-product formation. Those goals were achieved by adjusting the synthesis parameters of the materials, including the silicon-to-aluminum (Si/Al) ratio of the MFI zeolite (ranging from No Al, 100, to 50) and the loading of Ni (1 wt.% and 5 wt.%). The AASR reaction testing was adapted from the literature (Phongprueksathat et al., 2019; Z. Zhang et al., 2018). The effects of reaction

conditions, including the steam-to-carbon (S/C) ratio (5 and 3) and reaction time (ranging from 1 to 5 hours) were studied at 700 °C.

## References

- Ginter, D. (2001). *Chapter 46 - FAU Linde type Y Si(71), Al(29)* (H. Robson & K. P. B. T.-V. S. of Z. M. Lillerud (Eds.); pp. 156–158). Elsevier Science.
- Kosawatthanakun, S., Pansakdanon, C., Sosa, N., Chanlek, N., Roessner, F., Prayoonpokarach, S., and Wittayakun, J. (2022). Comparative properties of K/NaX and K/NaY from ultrasound-assisted impregnation and performance in transesterification of palm oil. *ACS Omega*, 7(11), 9130–9141.
- Phongprueksathat, N., Meeyoo, V., and Rirkomboon, T. (2019). Steam reforming of acetic acid for hydrogen production: Catalytic performances of Ni and Co supported on  $Ce_{0.75}Zr_{0.25}O_2$  catalysts. *International Journal of Hydrogen Energy*, 44(18), 9359–9367.
- Rakmae, S., Keawkumay, C., Osakoo, N., Montalbo, K. D., de Leon, R. L., Kidkhunthod, P., Chanlek, N., Roessner, F., Prayoonpokarach, S., and Wittayakun, J. (2016). Realization of active species in potassium catalysts on zeolite NaY prepared by ultrasound-assisted impregnation with acetate buffer and improved performance in transesterification of palm oil. *Fuel*, 184, 512–517.
- Robson, H., and Lillerud, K. P. B. T.-V. S. of Z. M. (Eds.). (2001). *Chapter 51 - GIS zeolite P Si(54), Al(46)* (pp. 169–170). Elsevier Science.
- Zhang, Y., Takahashi, R., Kimura, K., Fujitsuka, H., and Tago, T. (2023). Development of silicalite-1-encapsulated Ni catalyst from Ni phyllosilicate for dry reforming of methane. *Catalysis Surveys from Asia*, 27(1), 56–66.
- Zhang, Z., Hu, X., Li, J., Gao, G., Dong, D., Westerhof, R., Hu, S., Xiang, J., and Wang, Y. (2018). Steam reforming of acetic acid over Ni/Al<sub>2</sub>O<sub>3</sub> catalysts: Correlation of nickel loading with properties and catalytic behaviors of the catalysts. *Fuel*, 217, 389–403.

## CHAPTER II

### LITERATURE REVIEW

#### 2.1 Renewable energy

In an era marked by environmental concerns and the pressing need to address climate change, renewable energy has emerged as a paramount focus for researchers, policymakers, and industries worldwide (Hjeij et al., 2023). The transition to renewable energy sources is crucial to mitigate the harmful effects of fossil fuel consumption, reduce greenhouse gas emissions, and establish a cleaner and more resilient energy future (J. Wang et al., 2023). Among the various pathways to sustainable energy, two key exploration and development areas have gained significant attention: biodiesel generation and hydrogen fuel production (Babatunde et al., 2022). These avenues hold tremendous promise regarding their potential to provide renewable and low-carbon alternatives to traditional fossil fuel-based energy sources (Sandaka and Kumar, 2023).

Biodiesel, derived from renewable feedstocks including vegetable oils or animal fats such as palm oil, has emerged as a viable substitute for petroleum-based diesel fuel. Its production involves a process called transesterification, wherein the feedstock reacts with an alcohol, typically methanol, in the presence of a catalyst (Soly Peter et al., 2021). Biodiesel offers several advantages, including reduced greenhouse gas emissions and toxic gases like carbon dioxide, sulfur, and aromatic compounds because substituting the triglyceride structure of palm oil with shorter alkyl chains, results in easy combustion (Sajjad et al., 2023). Biodiesel is biodegradable, and compatible with existing diesel engines, making it an attractive option for achieving sustainable transportation (Demirbas, 2007) and reducing carbon footprints (Sandaka and Kumar, 2023). While nitrogen oxide ( $\text{NO}_x$ ) emissions may occur and there might be a slight risk of clogging (Jin et al., 2023), these issues can be effectively mitigated by improving engine characteristics (Sajjad et al., 2023).

On the other hand, hydrogen fuel, often hailed as the "ultimate" clean energy carrier, presents a versatile and emission-free alternative to conventional fossil fuels (Koroneos et al., 2004). Hydrogen can be produced through various methods, including electrolysis of water, biomass gasification, or steam reforming of hydrocarbons (Ishaq et al., 2022). One promising approach is acetic acid steam reforming, which utilizes acetic acid as a precursor to generate hydrogen gas (Ding et al., 2022). This method offers the advantage of utilizing readily available and renewable biomass resources. Hydrogen fuel has vast potential in transportation, power generation, and industrial applications (Mio et al., 2023; Rahim Malik et al., 2023), offering zero greenhouse gas emissions when utilized in fuel cells.

The sustainable energy production by focusing on biodiesel generation through transesterification of renewable feedstocks and hydrogen fuel production via acetic acid steam reforming are mainly developed by exploring innovative synthesis techniques, optimizing catalyst performance, and improving the efficiency and lifespan of catalysts. The contribution in these key areas promotes the adoption of clean and efficient energy sources, reduces dependence on fossil fuels, and paves the way toward a more sustainable and environmentally friendly energy landscape.

## 2.2 Transesterification of palm oil

Transesterification is a chemical process of significant importance in the conversion of vegetable oils or animal fats into biodiesel. Palm oil, derived from the fruit of oil palm trees, is a widely used vegetable oil with immense potential as a renewable energy source (X. Wang et al., 2020). The process of transesterification involves the reaction between palm oil and alcohol, typically methanol, in the presence of a catalyst. This chemical transformation leads to the production of fatty acid alkyl esters, commonly known as biodiesel, along with glycerol as a co-product (Prasertsit et al., 2013) following the chemical equation in Figure 2.1 (Widayat et al., 2013).

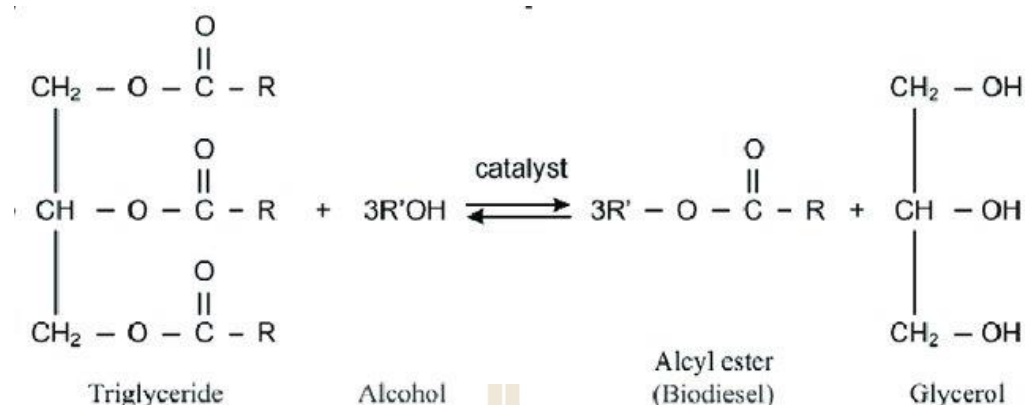


**Figure 2.1** Transesterification reaction for methyl ester (biodiesel) production. Reprinted (adapted) with permission from Widayat et al., 2013. Copyright 2013 the authors and publication by Elsevier Ltd.

The catalyst facilitates the conversion by lowering the activation energy required for the reaction, expediting the formation of esters. In addition, the process requires carefully controlled conditions, such as optimized temperature, pressure, and molar ratio of reactants, to ensure efficient conversion and desirable biodiesel quality (Muppaneni et al., 2013).

### 2.3 Catalyst for transesterification of palm oil

Basic catalyst is widely used in transesterification reaction. In the beginning, homogeneous catalysts such as NaOH and KOH are applied in industrial because they can provide high biodiesel yield (Atadashi et al., 2013; Mekonnen and Sendekie, 2021). However, the separation of the product from the catalyst is the main weakness. Then, heterogeneous catalysts like metal supported on alumina  $\text{M}/\text{Al}_2\text{O}_3$  (M: K, Na, Li, Ca, Ba) prepared by impregnation is used to solve the separation disadvantage and improve the catalyst reusability. Among several types of metal, potassium has the highest biodiesel yield due to strong basicity with low metal loading (Sánchez et al., 2014). However, the metal aggregation in spent catalyst prepared by impregnation inhibits the reusability (Vasić et al., 2020).

To improve the dispersion of potassium, zeolite was applied as catalyst support due to its high porosity and surface area. Zeolite can improve the metal ion distribution compared with non-porous material. NaX zeolite (fujasite structure, FAU) with high Al content (Si/Al ratio of 1-1.5) greatly enhances the dispersion of metals. After impregnation, potassium ion ( $K^+$ ) should diffuse through the zeolite cavity and exchange with counter cation ( $Na^+$ ) around the negative charge of  $AlO_4$  tetrahedra (Ezzeddine et al., 2018). Although high catalytic performance results in high palm oil conversion and biodiesel yield from K/NaX catalyst is reported, the actual active site is not specified in the collapsed spent catalyst (Kosawatthanakun et al., 2022). The role of zeolite pores should be investigated.

Therefore, NaX zeolite (Igarashi et al., 2012) with a pore size of 0.7 nm (12-member ring) should be compared the catalytic performance with NaP2 zeolite (Sharma et al., 2016) which is classified in gismodine (GIS) structure and has small pore size (0.3 nm) of 8-membered ring. The porous structure of both zeolites is revealed in Figure 2.2. The pores of NaP2 are smaller than all precursors in transesterification reaction and its Si/Al ratio is about 1.8. That means the pore size of NaX and NaP2 could be compared without nervousness about zeolite composition. Moreover, the stability of zeolite support with potassium is another concern. It was reported that potassium can break Si-O-Al bond and make zeolite structure collapse (Kosawatthanakun et al., 2022). So, the strategy to prepare strong zeolite support by microwave-assisted hydrothermal synthesis becomes an interest in this research.

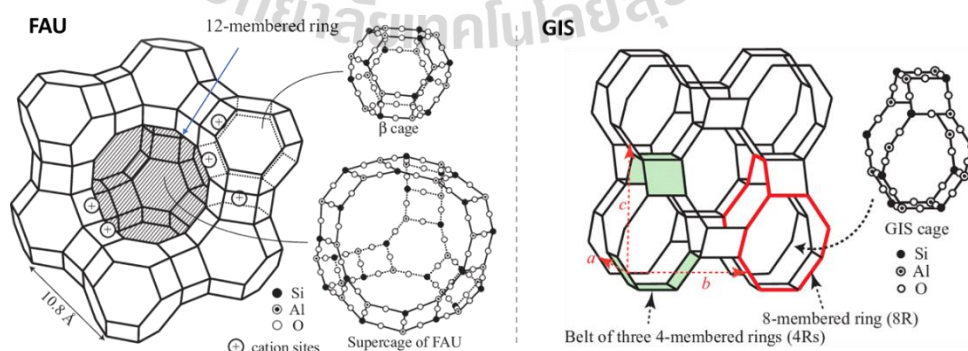


**Figure 2.2** Fujasite (FAU) and gismodine (GIS) porous structure of NaX and NaP2, respectively. Reprinted (adapted) with permission from Hettiarachchi et al., 2015; Igarashi et al., 2012. Copyright 2013 American Physical Society.

### 2.3.1 Conventional and microwave-assisted zeolite crystallization

Conventional and microwave-assisted crystallization are distinct techniques used to synthesize zeolites. They differ primarily in their heating mechanisms, heating efficiency and speed, control over reaction parameters, and the resulting morphology and properties of zeolite crystals and their stability (Le et al., 2019a). In conventional crystallization, external heat sources like ovens or furnaces are employed to heat the reaction mixture. Heat transfer occurs through conduction or convection. Conventional methods may be relatively slow, and temperature distribution within the mixture might be non-uniform. Achieving the desired temperature throughout the sample can take longer, leading to slower crystallization kinetics (Xia et al., 2019). Conversely, microwave-assisted crystallization involves the use of microwave radiation to generate heat directly within the reaction mixture. Microwaves cause rapid rotation of polar molecules, resulting in heat generation through molecular friction. Heat is generated directly within the mixture, ensuring rapid and uniform heating, which accelerates crystallization kinetics, reduces processing time, and improves reproducibility and crystallinity (Zeng et al., 2021).

Kappe (2004) demonstrates the difference in the temperature profiles of the mixture. Figure 2.3 (left) shows high heating speed under microwave radiation. In addition, finite element modeling after heating with microwave radiation and conventional heating (oil bath) for 1 minute is revealed in Figure 2.3 (right). Microwave irradiation raises the temperature of the whole volume simultaneously (bulk heating), whereas, in the oil-heated tube, the reaction mixture in contact with the vessel wall is first heated. So, heat conduction through the vessel is observed when homogeneous heating is not applied.

In the zeolite synthesis part, pure NaX zeolite is produced via conventional hydrothermal (CH) and microwave-assisted hydrothermal (MH) methods according to the literature (Ansari et al., 2014; Jantarit et al., 2020). A slight modification of the mentioned method, pure NaX zeolite can be synthesized by crystallization in hour periods. In contrast, the pure phase of GIS structure especially pure NaP2 zeolite is not easy to produce in a short time due to the flexibility of GIS structure and contaminant of other zeolites.

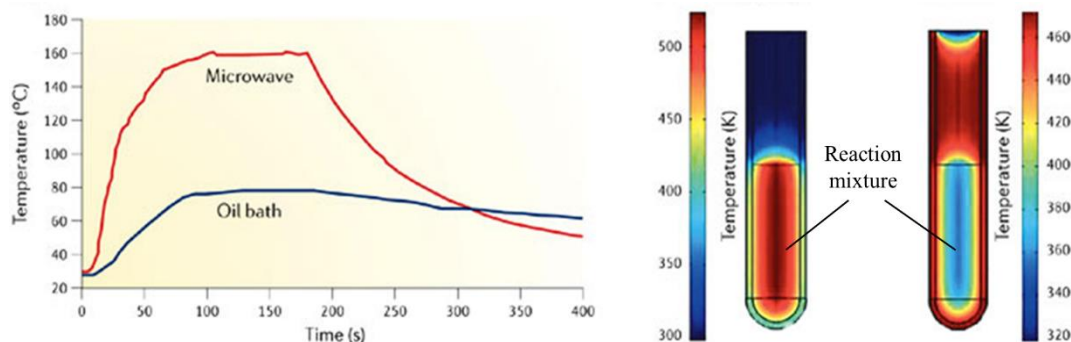
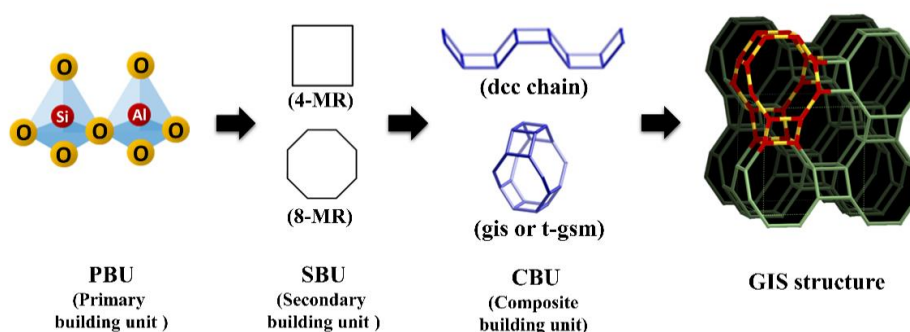


**Figure 2.3** The temperature profiles as function with times (left) and modeling of gradient temperature after heating for 1 min (right) in microwave irradiation versus oil bath. Reprinted (adapted) with permission from Kappe, 2004. Copyright 2004 Wiley-VCH Verlag GmbH & Co. KGaA, Weinheim.

### 2.3.2 Synthesis of NaP2 zeolite from CH and MH methods

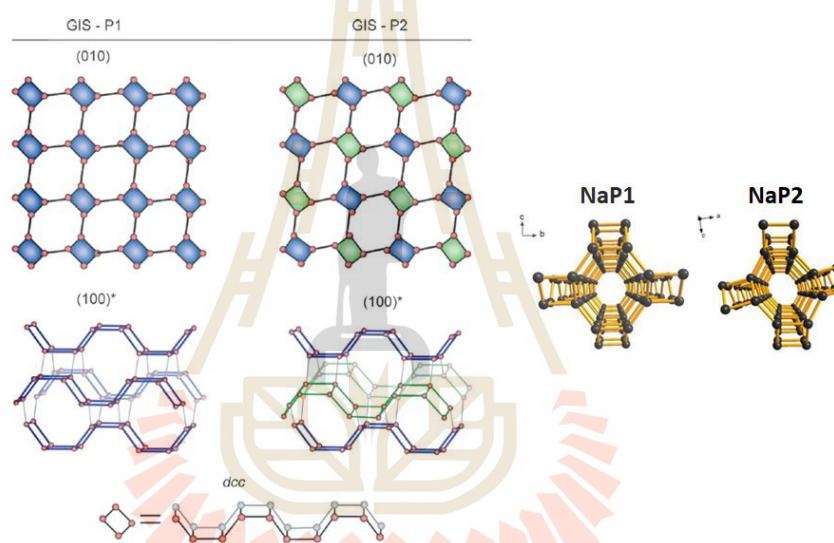
This part focuses on the traditional synthesis of zeolite P, the strategies to reduce hydrothermal time, the effect of microwave radiation and recrystallization in gel composition of zeolite NaY for high purity.

Figure 2.4 shows the building units of zeolite P to produce GIS structure. Zeolite P is a type of zeolite with a gismondine (GIS) framework which is generated from the linkage of silicon and aluminum atoms by oxygen-bridge bonds to form 4 and 8-membered oxygen rings (4-MR and 8-MR) or SBU. The SBUs combine to generate ddc chains and gis cavities. Then, the lower units continuously develop to brew a GIS structure (Meier et al., 2007).



**Figure 2.4** Building units of GIS structure. Reprinted (adapted) with permission from Meier et al., 2007. Copyright 2007 Elsevier B.V.

The flexibility in the unit cell structures of zeolite P was proposed by Oleksiak et al. (2016). The trivial differences in synthesis factors, such as temperatures, times, and gel compositions, produce two types of zeolite P (P1 and P2). Zeolite P2 is generated from the distortion of the 4-MR plane of zeolite P (P1), as revealed in Figure 2.5. From DFT calculation, the rotating for  $\pm 15$  degree of 4-MR (green color) results in the decreased pore size of GIS (less than 0.34 nm). It is smaller than the smallest part of methanol (0.36 nm) and triglyceride (0.7 nm), which are precursors in biodiesel production, to ensure that the chemicals cannot pass through the zeolite cavity.



**Figure 2.5** The slightly different plane structure of zeolite P1 and P2 from the distorted rotation of 4-MR in the GIS framework. Reprinted (adapted) with permission from Oleksiak et al., 2016. Copyright 2016 Wiley-VCH Verlag GmbH & Co. KGaA, Weinheim.

Even though P2-type has interesting advantage, the synthesis requires a long crystallization period. Table 2.1 compares the synthesis of zeolite P from various parameters. The standard synthesis procedure, according to the Synthesis Commission of International Zeolite Association (IZA), is the conventional hydrothermal method (CH) which has a long crystallization time, i.e., 60 days (Robson and Lillerud, 2001), as shown in Table 2.1 (entry 1). Therefore, to improve the conditional process by reducing a hydrothermal time, Albert et al. (1998) synthesized highly crystalline low-silica zeolite

NaP using sodium aluminosilicate gel by CH at 100 °C with increasing nucleation time (Table 2.1, entry 2). Although this condition can decrease the crystallization time, it still takes over 5 days.

**Table 2.1** Gel composition and synthesis parameters of zeolite P from the literature.

Gel composition	Main Product	Crystallization Time	Crystallization Temperature (°C)	Method	References
2.2 SiO <sub>2</sub> : Al <sub>2</sub> O <sub>3</sub> : 5.28 NaF: 105.6 H <sub>2</sub> O	P1	60 days	85	CH <sup>1</sup>	(Robson and Lillerud, 2001)
Na <sub>8</sub> Al <sub>8</sub> Si <sub>8</sub> O <sub>32</sub> · 15.2 H <sub>2</sub> O	P2	5 days	100	CH <sup>1</sup>	(Albert et al., 1998)
3.75 SiO <sub>2</sub> : 0.2 Al <sub>2</sub> O <sub>3</sub> : 4.3 Na <sub>2</sub> O: 220 H <sub>2</sub> O <sup>4</sup>	P1	42 hours	100	CH <sup>1</sup>	(Azizi and Tilami, 2009)
0.0065 NaAlO <sub>2</sub> : 0.023 Na <sub>2</sub> Si <sub>3</sub> O <sub>7</sub> (seed) <sup>3</sup>	P1	24 hours	100	CH <sup>1</sup>	(Yamni et al., 2014a)
0.04 NaAlO <sub>2</sub> :0.147 Na <sub>2</sub> Si <sub>3</sub> O <sub>7</sub> (feed)	P1	3 hours	110	MH <sup>2</sup>	(Sathupunya et al., 2002a)
1 SiO <sub>2</sub> : 0.25 Al <sub>2</sub> O <sub>3</sub> : 3 Na <sub>2</sub> O: 410 H <sub>2</sub> O <sup>5,6</sup>	P1	3 hours	110	MH <sup>2</sup>	(Sathupunya et al., 2002a)
17 Na <sub>2</sub> O: Al <sub>2</sub> O <sub>3</sub> : 17 SiO <sub>2</sub> : 345 H <sub>2</sub> O (seed) <sup>3</sup>	P2	2 hours	150	MH <sup>2</sup>	(Le et al., 2019b)
3 Na <sub>2</sub> O: Al <sub>2</sub> O <sub>3</sub> : 8 SiO <sub>2</sub> : 209 H <sub>2</sub> O (Overall)					

<sup>1</sup> CH = conventional hydrothermal method, <sup>2</sup> MH = microwave-assisted hydrothermal method, <sup>3</sup> use of seeding for nuclei preparation, use of structure-directing agent: <sup>4</sup> D-methionine, <sup>5</sup> triethanolamine, <sup>6</sup> triisopropanolamin.

D-Methionine, a structure directing agent (SDA) which influences zeolite P structure formation, was used to reduce the time to the scale of hour (Azizi and Ehsani Tilami, 2009) (Table 2.1, entry 3). However, the well-known disadvantages of organic SDA in zeolite synthesis are environmental toxicity, high cost, and difficult elimination. The process without SDA was investigated in 2014 (Table 2.1, entry 4). The crystallization time was reduced to 24 hours in zeolite P synthesis with a seeding procedure (Yamni et al., 2014). The appropriate proportion of aluminosilicate gel formed nuclei in the seeding step. It used a shorter time since the existence of seeding

increased the crystallization rate. Moreover, the homogeneity of the final products is a benefit of seeding (Lee et al., 2007). Although organic SDA and seeding were used, CH still required a long crystallization time.

The microwave-assisted hydrothermal method (MH) is an interesting strategy for fast crystallization due to its homogeneous heating system (Yang and Park, 2019). The consequence leads to avoiding the effect of heat conduction resulting in the formation of a uniform morphology and particle with a narrow size distribution. As shown in Table 2.1 (entry 5), Sathupunya et al. (2002) obtained zeolite P1 by using 15 hours in the crystallization process with microwave-assisted heating and an organic template. Le et al. (2019) reported the role of MH in the fast crystallization of zeolite NaP2 (Table 2.1, entry 6). A shorter synthesis time is due to homogeneous heating. However, the zeolite NaP2 samples still have impurities phases, including ANA and FAU zeolites.

In addition, there are reports in many publications (Aldahri et al., 2016, 2017; Belviso et al., 2018; Lv et al., 2020; Murayama et al., 2002; Z. Wang et al., 2013) on the procedures to synthesize mixed phases of zeolite P through different synthesis conditions and composition factors such as time, temperature, type of base, and the ratio of Si/Al/base. The products are mixed structures of GIS with other crystalline zeolites, including FAU, SOD, FER, ANA, and LTA. However, the impurity phases were discovered in the production of zeolite NaP2 when the above factors were applied with improper proportions. Moreover, the slightly different topology between NaP1 and NaP2 types in GIS structure is concerned. Oleksiak et al. (2016) applied the slight difference in zeolite conditions and compositions to create both phases of zeolite NaP. Khabuanchalad et al. (2008) reported the synthesis of NaP2-type zeolite by CH from the standard gel composition of zeolite NaY under high temperatures. The result indicated zeolite NaP2 with an impurity phase.

To produce a pure zeolite phase, recrystallization has been used. ZSM-22 (TON) and ZSM-35 (FER) were desilicated and recrystallized in a basic solution (Sousa et al., 2018). After separating the solid product, the pure phase of zeolite NaP1 was obtained. To reinforce the success in the transformation of FER (10-membered ring) to GIS (8-membered ring), Cheng et al. (2018) demonstrated the effect of NaOH

concentration and crystallization condition on the synthesis of GIS zeolite. FER structure was desilicated in NaOH solution for dissolution and/or depolymerization. Destroying the existing structure and the formation of basic zeolitic construction units might generate a pure phase of GIS structure.

The interest in this study is to synthesize high purity and high Al-content of zeolite NaP2 from the gel of zeolite NaY through double crystallization, recrystallization without separation of solid product from the first heating. Seeding and microwave radiation is used to decrease hydrothermal time and avoid uneven temperature. Moreover, NaP2 zeolite was compared with NaX zeolite in the transesterification reaction.

## 2.4 Acetic acid steam reforming

Acetic acid steam reforming (AASR) is a catalytic process with significant promise to produce hydrogen gas from renewable sources and organic waste streams. Acetic acid, a major component of bio-oil and various industrial waste streams, is converted into hydrogen gas and valuable by-products (Isahak et al., 2012). The primary and secondary reactions in AASR are shown in Figure 2.6 (Chen et al., 2017).

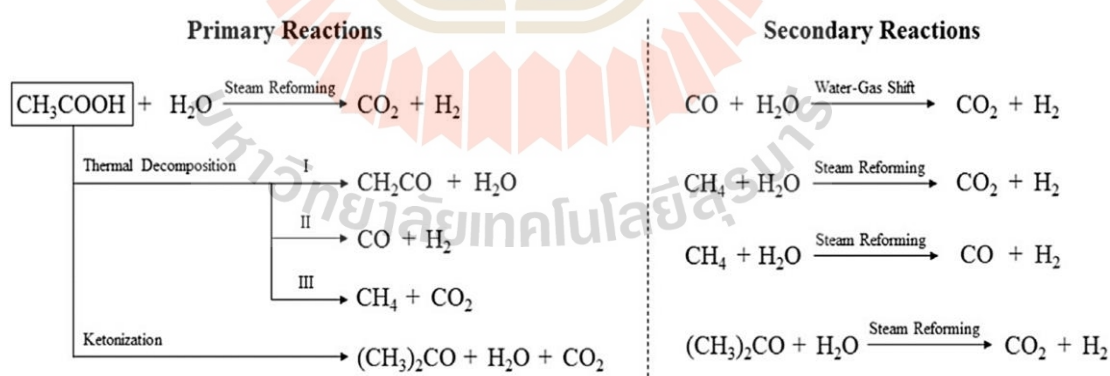


**Figure 2.6** Reaction pathway of AASR. Reprinted (adapted) with permission from Chen et al., 2017. Copyright 2017 Elsevier Ltd.

The relatively stable acetic acid has the potential to undergo transformations leading to various intermediates and products. These interactions are likely influenced by the operating conditions, forming a complex network of reactions. To gain a deeper

understanding of the reaction mechanism involved in AASR, the entire reaction system was partitioned into two components: primary reactions and secondary reactions.

The primary reactions from acetic acid and water are thermal decomposition, including (I) dehydration, (II) dehydrogenation and (III) decarboxylation of acetic acid to generate products and intermediate species, as shown in Figure 2.6 (left). The operating conditions could have significant impacts on these interactions, ultimately leading to the emergence of an intricate network of reactions (Chen et al., 2017). Moreover, a ketonization reaction takes place when the catalyst support has enough acidic sites such as  $\text{Al}_2\text{O}_3$ , the intermediates from this side reaction form acetone as a coke precursor (Z. Li et al., 2012).

The secondary reactions are revealed in Figure 2.6 (right). Under the presence of steam ( $\text{H}_2\text{O}$ ), water gas shift (WGS) and steam reforming (SR) with three sub-reactions occur. The produced carbon monoxide (CO) and methane ( $\text{CH}_4$ ) from the primary reaction interact with steam to generate hydrogen gas and CO or carbon dioxide ( $\text{CO}_2$ ), which can duplicate with other remaining gases, resulting in complex reactions. Additionally, undesired products such as acetone provide hydrogen via SR and originate the coke. So, the catalyst is another essential part of converting acetic acid into hydrogen gas under elevated temperatures and steam-rich conditions to optimize the conversion and selectivity of the desired products (Chen et al., 2017) and reduce coke formation.

## 2.5 Catalysts for acetic acid steam reforming

Coke deposition and sintering are two major culprits behind catalyst deactivation, significantly impairing performance. When a reaction takes place, coke formation and gasification happen simultaneously. To counteract the detrimental impact of coke, catalysts that can either suppress its formation or boost its gasification can be employed as effective measures (M. Li et al., 2021).

Active metal specie and support are two key catalyst compositions generally studied in acetic acid steam reforming. Nickel (Ni) catalysts are commonly used to facilitate these reactions and promote the desired conversions because of their affordable price compared with noble metals (Pt, Ag, Au). It promotes the cracking of

C–C and C-H bond, the resistance of oxidation, which make catalyst stability better (Hu and Lu, 2010).

Additionally, suitable Ni loading is important for initial Ni particle size and metal-support interaction, resulting in an improvement in catalytic performance. Zhang et al. (2018) report relationship between Ni loading and properties of Ni/Al<sub>2</sub>O<sub>3</sub> catalyst. The larger amount of Ni loading provides weak metal-support interaction and increases Ni particle size of fresh and spent catalysts. It also decreases the reduction degree and surface area of the catalyst. In addition, CO yield trends to decrease while the coke with higher carbon content is observed.

Moreover, the support material is important composition to affect carbon deposit for catalyst. Recent publications report the preparation of Ni on Al<sub>2</sub>O<sub>3</sub> support by impregnation (Ibrahim et al., 2021; Reeve et al., 2022; Zhang et al., 2018). This method involves the deposition of nickel species onto the zeolite support. This method is easy to prepare and allows precise control over nickel loading and distribution. However, the catalyst performance is limited by the low surface area of the support. To solve the weakness, Ni supported on porous aluminosilicate like ZSM-5 zeolite, which has MFI (Mobil-type five) structure, is prepared. The Ni/ZSM-5 catalyst provides high stability and low carbon deposition due to its porous structure, larger surface area, and high stability of ZSM-5 zeolite compared with Ni/Al<sub>2</sub>O<sub>3</sub> (Fakeeha et al., 2013). Although Al content enhances the strong interaction between Ni species and alumina, it facilitates the formation of by-products such as CH<sub>4</sub>, CO, and coke (Hu et al., 2012).

Therefore, the properties of the zeolite support, such as the Si/Al ratio, significantly impact the catalytic performance of Ni/MFI zeolite catalysts. The Si/Al ratio governs the framework composition of the zeolite, affecting its acidity, surface area, and pore structure. By varying the Si/Al ratio, it is possible to modulate the acidity of the catalyst and tailor its performance for specific reactions. To decrease side reactions, silicalite-1 support (silicious MFI zeolite) is applied to eliminate this weakness.

In this study, we investigate hydrogen production via acetic acid steam reforming over Ni/MFI zeolite catalysts prepared by the impregnation method. The catalysts are synthesized with varying Si/Al ratios of the zeolite support and different

nickel loadings. By systematically varying these parameters, we aim to explore the influence of zeolite composition and nickel loading on the catalytic activity, catalyst stability, and carbon decomposition.

## 2.6 References

- Albert, B. R., Cheetham, A. K., Stuart, J. A., and Adams, C. J. (1998). Investigations on P zeolites: synthesis, characterisation, and structure of highly crystalline low-silica NaP. *Microporous and Mesoporous Materials*, 21(1), 133–142.
- Aldahri, T., Behin, J., Kazemian, H., and Rohani, S. (2016). Synthesis of zeolite Na-P from coal fly ash by thermo-sonochemical treatment. *Fuel*, 182, 494–501.
- Aldahri, T., Behin, J., Kazemian, H., and Rohani, S. (2017). Effect of microwave irradiation on crystal growth of zeolitized coal fly ash with different solid / liquid ratios. *Advanced Powder Technology*, 28(11), 2865–2874.
- Ansari, M., Aroujalian, A., Raisi, A., Dabir, B., and Fathizadeh, M. (2014). Preparation and characterization of nano-NaX zeolite by microwave assisted hydrothermal method. *Advanced Powder Technology*, 25(2), 722–727.
- Atadashi, I. M., Aroua, M. K., Abdul Aziz, A. R., and Sulaiman, N. M. N. (2013). The effects of catalysts in biodiesel production: A review. *Journal of Industrial and Engineering Chemistry*, 19(1), 14–26.
- Azizi, S. N., and Ehsani Tilami, S. (2009). Recrystallization of zeolite Y to analcime and zeolite P with D-methionine as structure-directing agent (SDA). *Zeitschrift Für Anorganische Und Allgemeine Chemie*, 635(15), 2660–2664.
- Babatunde, A., Oluwoye, J. O., Rukmana, D., Pressley, J. A., and Kassu, A. (2022). Renewable energy system: alternative fuel usage in the energy market of the US public transportation system. *Environment and Ecology Research*, 10(5), 607–613.
- Belviso, C., Kharchenko, A., Agostinelli, E., Cavalcante, F., Peddis, D., Varvaro, G., Yaacoub, N., and Mintova, S. (2018). Red mud as aluminium source for the synthesis of magnetic zeolite. *Microporous and Mesoporous Materials*, 270(April), 24–29.
- Ch. Baerlocher, L. B. M. (2007). *Framework Type GIS*. <http://www.lza-structure.org/Databases/>. <https://asia.iza-structure.org/IZA-SC/framework.php?STC=GIS>

- Chen, G., Tao, J., Liu, C., Yan, B., Li, W., and Li, X. (2017). Hydrogen production via acetic acid steam reforming: a critical review on catalysts. *Renewable and Sustainable Energy Reviews*, 79, 1091–1098.
- Cheng, X., Cacciaguerra, T., Minoux, D., Dath, J.-P., Fajula, F., and Gérardin, C. (2018). Generation of parallelepiped-shaped mesopores and structure transformation in highly stable ferrierite zeolite crystals by framework desilication in NaOH solution. *Microporous and Mesoporous Materials*, 260, 132–145.
- Demirbas, A. (2007). Importance of biodiesel as transportation fuel. *Energy Policy*, 35(9), 4661–4670.
- Ding, Y., Cai, Y., Li, P., Gu, S., Song, S., Guan, J., Shen, Y., Han, Y., and He, W. (2022). Recyclable regeneration of NiO/NaF catalyst: hydrogen evolution via steam reforming of oxygen-containing volatile organic compounds. *Energy Conversion and Management*, 258, 115456.
- Ezzeddine, Z., Batonneau-Gener, I., Pouilloux, Y., Hamad, H., and Saad, Z. (2018). Synthetic NaX zeolite as a very efficient heavy metals sorbent in batch and dynamic conditions. In *Colloids and Interfaces* (Vol. 2, Issue 2).
- Fakeeha, A. H., Khan, W. U., Al-Fatesh, A. S., and Abasaeed, A. E. (2013). Stabilities of zeolite-supported Ni catalysts for dry reforming of methane. *Chinese Journal of Catalysis*, 34(4), 764–768.
- Hettiarachchi, G., Nakano, T., Masaki, Y., Muhid, M., Hamdan, H., and Nozue, Y. (2015). Insulator-to-metal transition in potassium-loaded zeolite P. *Journal of the Physical Society of Japan*, 84, 14702.
- Hjeij, D., Bicer, Y., Al-Sada, M. bin S., and Koç, M. (2023). Hydrogen export competitiveness index for a sustainable hydrogen economy. *Energy Reports*, 9, 5843–5856.
- Hu, X., and Lu, G. (2010). Comparative study of alumina-supported transition metal catalysts for hydrogen generation by steam reforming of acetic acid. *Applied Catalysis B: Environmental*, 99(1), 289–297.
- Hu, X., Zhang, L., and Lu, G. (2012). Pruning of the surface species on Ni/Al<sub>2</sub>O<sub>3</sub> catalyst to selective production of hydrogen via acetone and acetic acid steam reforming. *Applied Catalysis A: General*, 427–428, 49–57.

- Ibrahim, S. A., Ekinçi, E. K., Karaman, B. P., and Oktar, N. (2021). Coke-resistance enhancement of mesoporous  $\gamma$ - $\text{Al}_2\text{O}_3$  and MgO-supported Ni-based catalysts for sustainable hydrogen generation via steam reforming of acetic acid. *International Journal of Hydrogen Energy*, 46(77), 38281–38298.
- Igarashi, M., Nakano, T., Pham, T., Nozue, Y., Goto, A., Hashi, K., Ohki, S., Shimizu, T., Krajnc, A., Jeglič, P., and Arcon, D. (2012). NMR study of thermally activated paramagnetism in metallic low-silica X zeolite filled with sodium atoms. *Physical Review B*, 87.
- Isahak, W. N. R. W., Hisham, M. W. M., Yarmo, M. A., and Yun Hin, T. (2012). A review on bio-oil production from biomass by using pyrolysis method. *Renewable and Sustainable Energy Reviews*, 16(8), 5910–5923.
- Ishaq, H., Dincer, I., and Crawford, C. (2022). A review on hydrogen production and utilization: challenges and opportunities. *International Journal of Hydrogen Energy*, 47(62), 26238–26264.
- Jantarit, N., Tayraukham, P., Osakoo, N., Föttinger, K., and Wittayakun, J. (2020). Formation of EMT/FAU intergrowth and nanosized SOD zeolites from synthesis gel of zeolite NaX containing ethanol. *Materials Research Express*, 7(7).
- Jin, C., Wei, J., Chen, B., Li, X., Ying, D., Gong, L., and Fang, W. (2023). Effect of nanoparticles on diesel engines driven by biodiesel and its blends: a review of 10 years of research. *Energy Conversion and Management*, 291, 117276.
- Kappe, C. O. (2004). Controlled microwave heating in modern organic synthesis. *Angewandte Chemie International Edition*, 43(46), 6250–6284.
- Koroneos, C., Dompros, A., Roumbas, G., and Moussiopoulos, N. (2004). Life cycle assessment of hydrogen fuel production processes. *International Journal of Hydrogen Energy*, 29(14), 1443–1450.
- Kosawatthanakun, S., Pansakdanon, C., Sosa, N., Chanlek, N., Roessner, F., Prayoonpokarach, S., and Wittayakun, J. (2022). Comparative properties of K/NaX and K/NaY from ultrasound-assisted impregnation and performance in transesterification of palm oil. *ACS Omega*, 7(11), 9130–9141.
- Le, T., Wang, Q., Pan, B., Ravindra, A. V., Ju, S., and Peng, J. (2019a). Process regulation of microwave intensified synthesis of Y-type zeolite. *Microporous and Mesoporous*

- Materials*, 284, 476–485.
- Le, T., Wang, Q., Pan, B., Ravindra, A. V, Ju, S., and Peng, J. (2019b). Process regulation of microwave intensified synthesis of Y-type zeolite. *Microporous and Mesoporous Materials*, 284, 476–485.
- Lee, H. J., Kim, Y. M., Kweon, O. S., and Kim, I. J. (2007). Crystal growing and reaction kinetic of large NaX zeolite crystals. *Journal of the European Ceramic Society*, 27(2), 581–584.
- Li, M., Sun, Z., and Hu, Y. H. (2021). Catalysts for CO<sub>2</sub> reforming of CH<sub>4</sub>: a review. *Journal of Materials Chemistry A*, 9(21), 12495–12520.
- Li, Z., Hu, X., Zhang, L., Liu, S., and Lu, G. (2012). Steam reforming of acetic acid over Ni/ZrO<sub>2</sub> catalysts: effects of nickel loading and particle size on product distribution and coke formation. *Applied Catalysis A: General*, 417–418, 281–289.
- Lv, Y., Ye, C., Zhang, J., and Guo, C. (2020). Rapid and efficient synthesis of highly crystalline SSZ-13 zeolite by applying high shear mixing in the aging process. *Microporous and Mesoporous Materials*, 293(October 2019), 109812–109819.
- Mekonnen, K. D., and Sendekie, Z. B. (2021). NaOH-catalyzed methanolysis optimization of biodiesel synthesis from desert date seed kernel oil. *ACS Omega*, 6(37), 24082–24091.
- Mio, A., Barbera, E., Pavan, A. M., Danielis, R., Bertucco, A., and Fermeglia, M. (2023). Analysis of the energetic, economic, and environmental performance of hydrogen utilization for port logistic activities. *Applied Energy*, 347, 121431.
- Muppaneni, T., Reddy, H. K., Ponnusamy, S., Patil, P. D., Sun, Y., Dailey, P., and Deng, S. (2013). Optimization of biodiesel production from palm oil under supercritical ethanol conditions using hexane as co-solvent: a response surface methodology approach. *Fuel*, 107, 633–640.
- Murayama, N., Yamamoto, H., and Shibata, J. (2002). Mechanism of zeolite synthesis from coal fly ash by alkali hydrothermal reaction. *International Journal of Mineral Processing*, 64(1), 1–17.
- Oleksiak, M. D., Ghorbanpour, A., Conato, M. T., McGrail, B. P., Grabow, L. C., Motkuri, R. K., and Rimer, J. D. (2016). Synthesis strategies for ultrastable zeolite GIS polymorphs as sorbents for selective separations. *Chemistry – A European*

- Journal*, 22(45), 16078–16088.
- Prasertsit, K., Mueanmas, C., and Tongurai, C. (2013). Transesterification of palm oil with methanol in a reactive distillation column. *Chemical Engineering and Processing: Process Intensification*, 70, 21–26.
- Rahim Malik, F., Yuan, H.-B., Moran, J. C., and Tippayawong, N. (2023). Overview of hydrogen production technologies for fuel cell utilization. *Engineering Science and Technology, an International Journal*, 43, 101452.
- Reeve, J., Mahmud, T., Twigg, M. V, and Dupont, V. (2022). The kinetics of acetic acid steam reforming on Ni/Ca-Al<sub>2</sub>O<sub>3</sub> catalyst. *International Journal of Hydrogen Energy*, 47(84), 35709–35722.
- Robson, H., and Lillerud, K. P. B. T.-V. S. of Z. M. (Eds.). (2001). *Chapter 51 - GIS zeolite P Si(54), Al(46)* (pp. 169–170). Elsevier Science.
- Sajjad, M. O. A., Sathish, T., Saravanan, R., Asif, M., Linul, E., and Ağbulut, Ü. (2023). Combustion, performance and emission discussion of soapberry seed oil methyl ester blends and exhaust gas recirculation in common rail direct fuel injection system. *Energy*, 278, 127763.
- Sánchez, M., Navas, M., Ruggera, J. F., Casella, M. L., Aracil, J., and Martínez, M. (2014). Biodiesel production optimization using  $\gamma$ -Al<sub>2</sub>O<sub>3</sub> based catalysts. *Energy*, 73, 661–669.
- Sandaka, B. P., and Kumar, J. (2023). Alternative vehicular fuels for environmental decarbonization: a critical review of challenges in using electricity, hydrogen, and biofuels as a sustainable vehicular fuel. *Chemical Engineering Journal Advances*, 14, 100442.
- Sathupunya, M., Gulari, E., and Wongkasemjit, S. (2002a). ANA and GIS zeolite synthesis directly from alumatrane and silatrane by sol-gel process and microwave technique. *Journal of the European Ceramic Society*, 22(13), 2305–2314.
- Sathupunya, M., Gulari, E., and Wongkasemjit, S. (2002b). ANA and GIS zeolite synthesis directly from alumatrane and silatrane by sol-gel process and microwave technique. *Journal of the European Ceramic Society*, 22(13), 2305–2314.
- Sharma, P., Song, J.-S., Han, M. H., and Cho, C.-H. (2016). GIS-NaP1 zeolite microspheres as potential water adsorption material: influence of initial silica concentration on

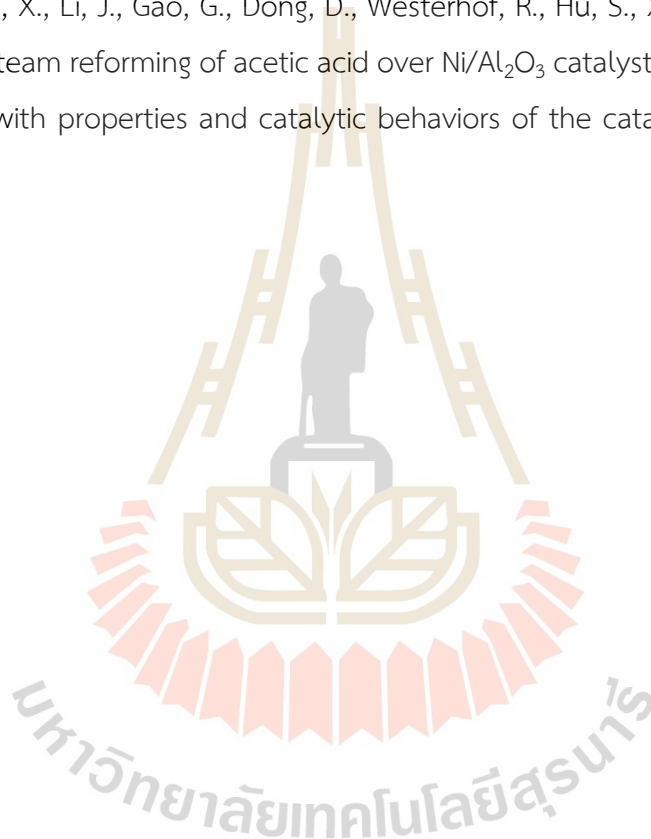
- adsorptive and physical/topological properties. *Scientific Reports*, 6(1), 22734.
- Soly Peter, A., Alias, M. P., Iype, M. P., Jolly, J., Sankar, V., Joseph Babu, K., and Baby, D. K. (2021). Optimization of biodiesel production by transesterification of palm oil and evaluation of biodiesel quality. *Materials Today: Proceedings*, 42, 1002–1007.
- Sousa, L. V., Silva, A. O. S., Silva, B. J. B., Quintela, P. H. L., Barbosa, C. B. M., Fréty, R., and Pacheco, J. G. A. (2018). Preparation of zeolite P by desilication and recrystallization of zeolites ZSM-22 and ZSM-35. *Materials Letters*, 217, 259–262.
- Vasić, K., Hojnik Podrepšek, G., Knez, Ž., and Leitgeb, M. (2020). Biodiesel production using solid acid catalysts based on metal oxides. In *Catalysts* (Vol. 10, Issue 2).
- Wang, J., Usman, M., Saqib, N., Shahbaz, M., and Hossain, M. R. (2023). Asymmetric environmental performance under economic complexity, globalization and energy consumption: evidence from the world's largest economically complex economy. *Energy*, 279, 128050.
- Wang, X., Xu, X., Wang, Q., Huang, Z., He, J., and Qiu, T. (2020). Fatty acid methyl ester synthesis through transesterification of palm oil with methanol in microchannels: flow pattern and reaction kinetics. *Energy & Fuels*, 34(3), 3628–3639.
- Wang, Z., Kumakiri, I., Tanaka, K., Chen, X., and Kita, H. (2013). NaY zeolite membranes with high performance prepared by a variable-temperature synthesis. *Microporous and Mesoporous Materials*, 182, 250–258.
- Widayat, Wibowo, A. D. K., and Hadiyanto. (2013). Study on production process of biodiesel from rubber seed (*Hevea Brasiliensis*) by in situ (trans)esterification method with acid catalyst. *Energy Procedia*, 32, 64–73.
- Xia, S., Chen, Y., Xu, H., Lv, D., Yu, J., and Wang, P. (2019). Synthesis EMT-type zeolite by microwave and hydrothermal heating. *Microporous and Mesoporous Materials*, 278, 54–63.
- Yamni, K., Tijani, N., and Lamsiah, S. (2014a). Influence of the crystallization temperature on the synthesis of Y zeolite. *IOSR Journal of Applied Chemistry*, 7(7), 58–61.
- Yamni, K., Tijani, N., and Lamsiah, S. (2014b). Influence of the crystallization temperature on the synthesis of Y zeolite. *IOSR Journal of Applied Chemistry*, 7(7),

58–61.

Yang, G., and Park, S.-J. (2019). Conventional and microwave hydrothermal synthesis and application of functional materials: a review. *Materials (Basel, Switzerland)*, *12*(7).

Zeng, X., Hu, X., Song, H., Xia, G., Shen, Z.-Y., Yu, R., and Moskovits, M. (2021). Microwave synthesis of zeolites and their related applications. *Microporous and Mesoporous Materials*, *323*, 111262.

Zhang, Z., Hu, X., Li, J., Gao, G., Dong, D., Westerhof, R., Hu, S., Xiang, J., and Wang, Y. (2018). Steam reforming of acetic acid over Ni/Al<sub>2</sub>O<sub>3</sub> catalysts: correlation of nickel loading with properties and catalytic behaviors of the catalysts. *Fuel*, *217*, 389–403.



# CHAPTER III

## SYNTHESIS OF PURE PHASE NaP2 ZEOLITE FROM THE GEL OF SODIUM Y BY CONVENTIONAL AND MICROWAVE-ASSISTED HYDROTHERMAL METHODS

### 3.1 Abstract

The gel of zeolite NaY shows potential as a precursor for other zeolites. In this chapter, the focus is on converting the NaY gel into NaP2. The conventional hydrothermal (CH) method is used to easily obtain pure phase NaP2 by maintaining a crystallization condition of 150 °C for 24 hours. The resulting NaP2 sample, CH150, has an average particle size of 10.3 μm and an Si/Al ratio of 1.82. To achieve single crystallization, the microwave-assisted hydrothermal (MH) method is employed, and various parameters including crystallization temperature (90, 150, 175 °C) and time (15, 30, 45, 60 min) are investigated. X-ray diffraction and scanning electron microscopy are used to analyze the samples. However, mixed phases of P1 and P2 or ANA are observed. Another attempt is made using a double crystallization approach via the MH method. The process involves crystallizing at 90 °C for 1 hour, rapidly cooling down to room temperature in the microwave chamber, aging for 23 hours, and finally crystallizing at 150 °C for 1 hour to obtain MH90A150. It has an average crystal size of 16.45 μm and an Si/Al ratio of 1.85. It is worth noting that both samples, CH150 and MH90A150, exhibit a high aluminum composition in NaP2 which has potential for adsorption applications.

### 3.2 Introduction

Zeolite P in the gismondine (GIS) framework type is composed of secondary building units (SBU) that contain four- and eight-membered rings of T atoms (T = Si or Al) linked together by sharing oxygen atoms. A molecular sieve property (Flanigen, 2001) from small pore diameter of 2.8 x 4.8 Å [010] (Baerlocher et al., 2007c) makes it

suitable for sensing application (Arrigo et al., 2011) and separation of heavy metals (Ali et al., 2015; Nery et al., 2003) or small gases (Dong and Lin, 1998; Fischer and Bell, 2012; Yin et al., 2007). The flexibility in unit cell structures of zeolite P is reported by Baerlocher et al. (1972) and McCusker et al. (1985). The distortion of the SBU planes produces two isotypes, P1 and P2, which have different pore shapes and sizes.

Likewise, publication of Oleksiak et al. (2016) reported the narrower of eight-membered pore of P2 than P1. Consequently, the P2 type has a higher adsorption ability for small gases such as H<sub>2</sub> (Oleksiak et al., 2016).

**Table 3.1** Gel composition and synthesis parameters of zeolite P from the literature.

Gel composition	Main Product	Crystallization Time	Crystallization Temperature (°C)	Method	References
2.2 SiO <sub>2</sub> : Al <sub>2</sub> O <sub>3</sub> : 5.28 NaF: 105.6 H <sub>2</sub> O	P1	60 days	85	CH <sup>1</sup>	(Robson and Lillerud, 2001)
Na <sub>8</sub> Al <sub>8</sub> Si <sub>8</sub> O <sub>32</sub> · 15.2 H <sub>2</sub> O	P2	5 days	100	CH <sup>1</sup>	(Albert et al., 1998)
3.75 SiO <sub>2</sub> : 0.2 Al <sub>2</sub> O <sub>3</sub> : 4.3 Na <sub>2</sub> O: 220 H <sub>2</sub> O <sup>4</sup>	P1	42 hours	100	CH <sup>1</sup>	(Azizi and Tilami, 2009)
0.0065 NaAlO <sub>2</sub> : 0.023 Na <sub>2</sub> Si <sub>3</sub> O <sub>7</sub> (seed) <sup>3</sup>	P1	24 hours	100	CH <sup>1</sup>	(Yamni et al., 2014)
0.04 NaAlO <sub>2</sub> : 0.147 Na <sub>2</sub> Si <sub>3</sub> O <sub>7</sub> (feed)					
1 SiO <sub>2</sub> : 0.25 Al <sub>2</sub> O <sub>3</sub> : 3 Na <sub>2</sub> O: 410 H <sub>2</sub> O <sup>5,6</sup>	P1	3 hours	110	MH <sup>2</sup>	(Sathupunya et al., 2002)
17 Na <sub>2</sub> O: Al <sub>2</sub> O <sub>3</sub> : 17 SiO <sub>2</sub> : 345 H <sub>2</sub> O (seed) <sup>3</sup>					
3 Na <sub>2</sub> O: Al <sub>2</sub> O <sub>3</sub> : 8 SiO <sub>2</sub> : 209 H <sub>2</sub> O (Overall)	P2	2 hours	150	MH <sup>2</sup>	(Le et al., 2019)

<sup>1</sup> CH = conventional hydrothermal method, <sup>2</sup> MH = microwave-assisted hydrothermal method, <sup>3</sup> use of seeding for nuclei preparation, use of structure-directing agent: <sup>4</sup> D-methionine, <sup>5</sup> triethanolamine, <sup>6</sup> triisopropanolamin.

Despite the interesting benefit, the synthesis of P2 requires a long crystallization period and produces impurity phases. The synthesis of zeolite P with several parameters are compared in Table 3.1. The standard method from the International Zeolite Association Synthesis Commission (IZA) is the conventional hydrothermal

method (CH) which has a long crystallization time, i.e., 60 days (Table 3.1, entry 1) (Robson and Lillerud, 2001). Numerous researchers have improved the synthesis by extending the nucleation time (Table 3.1, entry 2) (Albert et al., 1998), using a structure-directing agent (SDA) (Table 3.1, entry 3) (Azizi and Tilami, 2009) and seeding (Table 3.1, entry 4) (Yamni et al., 2014). Although the time is shortened, it still takes several days. An strategy for the fast synthesis is the microwave-assisted hydrothermal method (MH (Table 3.1, entry 5–6) (Le et al., 2019; Sathupunya et al., 2002) due to its rapid and homogeneous heating (Yang and Park, 2019).

The impurity phases from the conventional synthesis method can be reduced by recrystallization, also called double crystallization. For example, Sousa et al. (Sousa et al., 2018) recrystallized ZSM-22 (structure type TON) and ZSM-35 (structure type FER) by basic treatment to generate a pure phase of zeolite NaP1. However, there are no reports about the synthesis of zeolite NaP2 from recrystallization. Although zeolite NaP2 has been synthesized from NaY gel, the mixed zeolite phases were obtained (Khabuanchalad et al., 2008). Consequently, this present work aimed to synthesize the high purity of zeolite NaP2 from the gel of zeolite NaY through double crystallization without the separation of solid product after the first heating. Seeding and microwave radiation will be used to decrease hydrothermal time and avoid irregular temperature.

### 3.3 Materials and Methods

#### 3.3.1 Materials

Chemicals in this study were silicon dioxide ( $\text{SiO}_2$ , 99%, Carlo Erba), sodium hydroxide anhydrous pellets ( $\text{NaOH}$ , 97%, Carlo Erba) and sodium aluminate ( $\text{NaAlO}_2$ , 95%, Sigma Aldrich). Sodium silicate ( $\text{Na}_2\text{SiO}_3$ ), which was a silicon source precursor had chemical composition about 28.7 wt%  $\text{SiO}_2$ , 8.9 wt%  $\text{Na}_2\text{O}$ . Moreover, hydrofluoric acid (HF, 49% QRëC), hydrochloric acid (HCl, 37%, ACI Labscan), boric acid ( $\text{H}_3\text{BO}_3$ , 99.5%, Merck), and nitric acid ( $\text{HNO}_3$ , 69%, ANaPURE) were used in the digestion step.

#### 3.3.2 Preparation of Zeolite Synthesis Gel

The overall gel with the molar ratio of  $10\text{SiO}_2:\text{Al}_2\text{O}_3:4.62\text{Na}_2\text{O}:180\text{H}_2\text{O}$  was prepared by the method from that of zeolite NaY (Robson et al., 2001) with the

scale on-fourth, from a seed gel ( $10\text{SiO}_2:\text{Al}_2\text{O}_3:10.67\text{Na}_2\text{O}:180\text{H}_2\text{O}$ ) and feedstock gel ( $10\text{SiO}_2:\text{Al}_2\text{O}_3:4.30\text{Na}_2\text{O}:180\text{H}_2\text{O}$ ). It was aged for 24 h before crystallization. All the gel ratios were calculated from the weight of each component.

### 3.3.3 Single Crystallization

The overall gel was crystallized by conventional and microwave-assisted hydrothermal methods (CH and MH, respectively). In the CH method, the overall gel was poured into a Teflon-lined autoclave (250 mL) and heated with a rate of  $5\text{ }^\circ\text{C}/\text{min}$  to  $150\text{ }^\circ\text{C}$  and kept for 24 h in a muffle furnace (Carbolite, CWF 12/23) and cooled down outside the furnace to room temperature. This sample was labeled CH150. In the MH method, the overall gel was transfused into two microwave tubes (100 mL) with equal amount and heated by microwave (Anton Paar, Multiwave 3000) with XF-100 rotor and the power of 900 W to  $150\text{ }^\circ\text{C}$  within 4 minutes, kept for the anticipated period of 1 hour and cooled down rapidly in the microwave chamber to obtain MH150 sample.

To investigate the temperature effect, the samples MH90 and MH175 were prepared by microwave-assisted method and crystallized for 1 hour at  $90\text{ }^\circ\text{C}$  and  $175\text{ }^\circ\text{C}$ , respectively. The result of the time was studied by heating at  $150\text{ }^\circ\text{C}$  and  $175\text{ }^\circ\text{C}$ , held for 15, 30, 45 and 60 minutes.

### 3.3.4 Double Crystallization via MH Method

There were three steps to investigate the phase alteration from each step. Firstly, the overall gel was transferred into the microwave tubes with an equal amount for evenness. The sample was heated by microwave from room temperature up to  $90\text{ }^\circ\text{C}$  and crystallized for 1 hour before cooling down. This sample was named MH90. Secondly, the sample was kept unopened (aged) for 23 hours at room temperature in the same microwave tubes. This sample was named MH90A. Finally, the sample after aging was recrystallized again at  $150\text{ }^\circ\text{C}$  for 1 hour to obtain MH90A150 sample.

After heating, all solid products were separated by centrifugation, washed several times with deionized (DI) water until the pH of the filtrates was 7, and dried at  $90\text{ }^\circ\text{C}$  overnight to acquire white powder samples.

### 3.3.5 Characterization of Solid Products

Powder X-ray diffraction (XRD) analysis was conducted on a Bruker (AXS D8) diffractometer using Cu K $\alpha$  radiation with a current of 40 mA and a potential of 40 kV to analyze the phases and structures of the crystalline products. This analysis was performed on all samples on the same day to ensure accurate comparison of crystallinity. The functional groups present in the samples were determined using Fourier-transform infrared spectroscopy (FTIR) on a Bruker (Tensor 27) instrument. The attenuated total reflectance (ATR) mode was utilized with a resolution of 4 cm<sup>-1</sup>. Morphology studies were carried out using a field emission scanning electron microscope (FESEM), specifically the JEOL (JSM -7800F) model. The silicon-aluminum (Si/Al) mole ratios in the solid products were determined using inductively coupled plasma optical emission spectrometry (ICP-OES) with a Perkin Elmer (Optima 8000) instrument. Argon was used as the carrier gas during the analysis. To prepare the samples for analysis, a digestion method described by Bunmai et al. (2018) was followed. Each sample, weighing fifty milligrams, was mixed with 0.5 mL of aqua regia (1HNO<sub>3</sub>:3HCl volumetric ratio) and 3.0 mL of HF. The mixture was then placed in a 250 mL polypropylene (PP) bottle and heated at 110 °C for one hour. After cooling to room temperature, 2.8 g of H<sub>3</sub>BO<sub>3</sub> and 10 mL of deionized (DI) water were added to the mixture. The volume was adjusted to 100 mL using DI water in a PP volumetric flask. The emission wavelengths of silicon and aluminum in the solid samples were measured at 251.611 nm and 396.153 nm, respectively.

## 3.4 Results and Discussion

### 3.4.1 Comparison of Conventional and Microwave-Assisted Hydrothermal Methods of Single Crystallization

In Figure 3.1, the XRD patterns of sample from single crystallization by the CH method at 150 °C for 24 hours (CH150) and MH method at 150 °C for 1 hour (MH150) are revealed. The pattern of CH150 corresponds to the phase of zeolite NaP2. The splitting of peaks in the GIS structure refers to the presence of two distinct types of secondary building units (SBUs) that rotate within the framework. These SBUs can be classified as either planes or four-membered rings (4MR). This phenomenon

contributes to the unique structural of the GIS framework (Oleksiak et al., 2016). No other phases of zeolite were observed in the sample. In contrast to the findings of Khabuanchalad et al. (2008), this study successfully synthesized pure phase NaP2 from the NaY gel through conventional hydrothermal crystallization at a higher temperature of 150 °C for a shorter duration of 24 hours and phase of NaY is not observed.

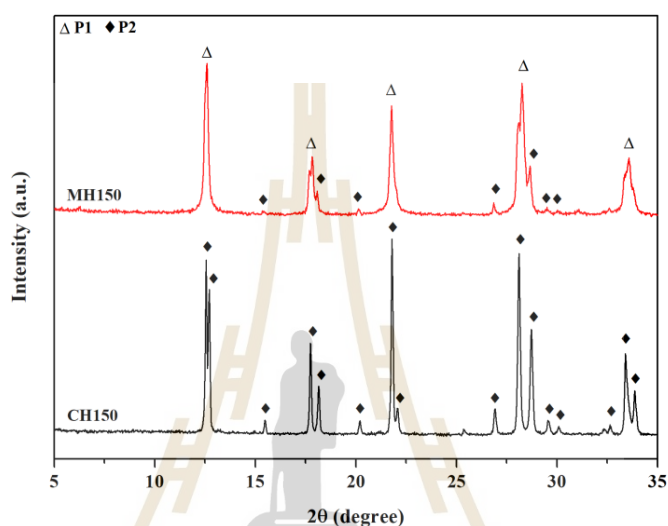


**Figure 3.1** Powder X-ray diffraction (XRD) patterns of zeolite products from conventional and microwave-assisted hydrothermal methods with single crystallization at 150 °C for 24 hours (CH150) and 1 hour (MH150).

The XRD pattern of MH150 reveals the presence of mixed zeolite phases, with NaP1 as the main phase and NaP2 as the minor phase. This is in contrast to the findings of Le et al. (2019), that obtained NaP2 as the main phase with a trace of NaY using a different gel composition, higher microwave power (1600 W), and longer crystallization time (2 hours) at the same temperature. Additionally, Le et al. (2019) reported that crystallization at 100 °C and 120 °C only resulted in the formation of zeolite NaY. However, when they used a gel with a Si/Al ratio of 5 and a shorter crystallization time of 0.5 hour, they were able to obtain pure phase NaP2.

The SEM image of CH150 is showed in Figure 3.2a. The polycrystals with polygons shape, some with diamond-like shapes, and trisecting cracks. This morphology is similar to that reported for zeolite P2 in the literature (Le et al., 2019;

Oleksiak et al., 2016). The particle size distribution of the CH150 sample was determined by measuring the size of 50 particles using SEM analysis. The results showed that the particle size ranged from 4  $\mu\text{m}$  to 14  $\mu\text{m}$ , with an average size of 10.3  $\mu\text{m}$ . Based on the ICP analysis, the Si/Al ratio of this particular sample was determined to be 1.82. Despite the sample exhibiting diverse shapes and morphology, the XRD results exclusively confirmed the presence of the pure phase of NaP2. Consequently, one could conclude that NaP2 had various morphology. In the case of MH150, the SEM image (refer to Figure 3.2b) revealed larger particles with a distinct morphology compared to CH150. The average particle size of MH150 was measured to be 17.4  $\mu\text{m}$ , and the Si/Al ratio was found to be 1.77. The primary phase exhibited a cheese ball-like morphology similar to those reported in previous studies (Azizi et al., 2013; Sharma et al., 2016). These zeolite microcrystals were well-developed on the surface of the microspheres, with each particle measuring less than one micrometer in size. The SEM analysis, which identified mixed phases, was consistent with the XRD findings.

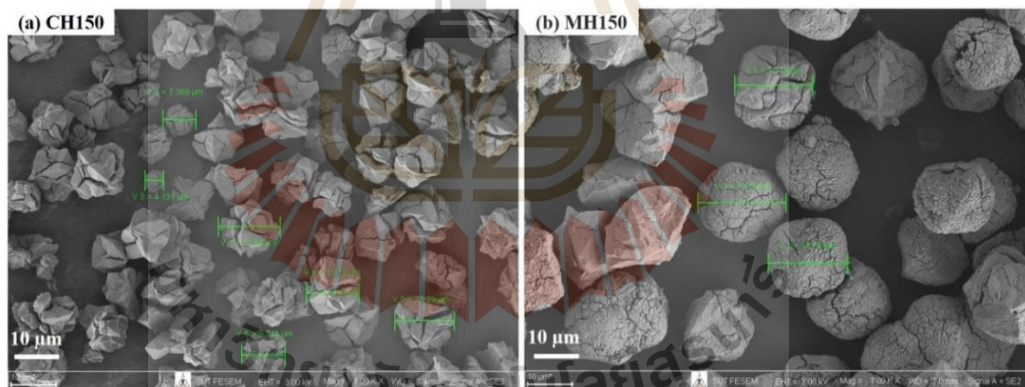


**Figure 3.2** A field emission scanning electron microscopy (FESEM) images of the zeolite products from conventional and microwave-assisted hydrothermal methods with single crystallization at 150 °C for 24 hours (CH150) and 1 hour (MH150).

The heating method used during the synthesis process had a significant impact on the phase of the products, as observed from the XRD and SEM results. The MH method, which involved faster heating rates, led to a faster crystal growth rate and larger particle sizes compared to the CH method. This phenomenon was also observed in the synthesis of zeolite NaY using both CH and MH methods (Panzarella et al., 2007).

Additionally, the homogeneous heating provided by microwave radiation resulted in the homogeneous growth of nuclei, leading to a narrower particle size distribution in MH150. Consequently, the crystallization process in MH was approximately 24 times faster than in CH at the same temperature. The use of microwave radiation significantly reduced the crystallization time by rapidly spreading heat to all positions (Li and Yang, 2008). However, the fast-heating rate also resulted in the formation of mixed phases.

### 3.4.2 Effect of Temperature and Time on Single Crystallization by Microwave-Assisted Hydrothermal Methods

Figure 3.3a shows the XRD patterns of MH90, MH150 and MH175 which are the products from crystallization by microwave heating at 90, 150 and 175 °C, respectively. The MH90 sample had pure phase NaY zeolite (Bunmai et al., 2020a). This result was consistent with the work by Le et al. (2019) that NaY was obtained at 100 and 120 °C. The sample MH150 had mixed phases of NaP1 and NaP2 zeolites. Finally, the MH175 sample displayed the mixed phases of NaP2 as the major phase and Anacime (ANA) zeolite as the minor phase (Gu et al., 2019). The densities of faujasite (FAU) (Baerlocher et al., 2007), GIS (Baerlocher et al., 2007c) and ANA (Baerlocher et al., 2007) zeolites are 13.3, 16.4 and 19.2 T/1000 Å<sup>3</sup>, respectively. The results confirm that the higher crystallization temperature produces zeolite with a higher framework density (Le et al., 2019). Although the exact densities of the two GIS zeolites are not clear, our results imply that the density of NaP2 is higher than NaP1 due to the smaller pore size (Oleksiak et al., 2016). From these results, the suitable crystallization temperature for NaP2 is 175 °C. However, the product still contains ANA zeolite as an impurity. Consequently, the shorter crystallization time and lower temperature to improve purity was investigated.

Figure 3.3b illustrates the XRD patterns of zeolites obtained through single crystallization by MH at 175 °C for different durations: 15, 30, 45, and 60 minutes. All samples exhibited the presence of an ANA phase, with the 60-minute sample displaying a higher concentration of ANA phase compared to the others. This observation aligns with previous literature findings that longer crystallization times yield products with higher density (Maldonado et al., 2013), accompanied by a competitive phase. Consequently, crystallization at 150 °C to reduce the ANA phase is

investigated. Figure 3.3c displays the XRD patterns of samples crystallized for 15, 30, 45, and 60 minutes. In all samples, the main phase was NaP1, as reported by Oleksiak et al. (2016), along with NaP2.

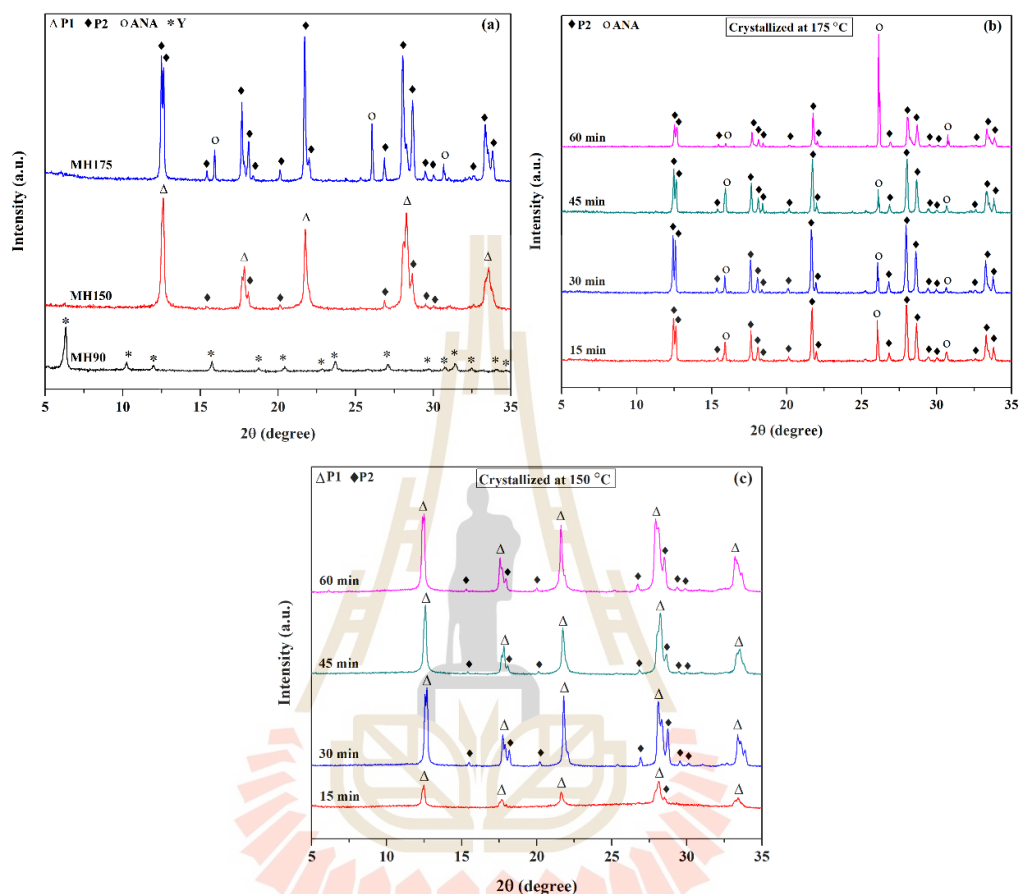


**Figure 3.3** Powder XRD patterns of zeolites from single crystallization via MH (a) for 1 hour at 90 °C, 150 °C and 175 °C, (b) at 175 °C, and (c) 150 °C for various times: 15, 30, 45 and 60 minutes.

Figure 3.4 showcases the SEM images of zeolites obtained through single crystallization via MH at 150 °C for different durations: 15, 30, 45, and 60 minutes. The sample crystallized for 15 minutes exhibited an amorphous phase due to the short duration of crystallization. On the other hand, the remaining samples displayed a mixed phase consisting of NaP1 (cheese ball-like) (Azizi et al., 2013; Sharma et al., 2016) and NaP2 (polygonal) (Le et al., 2019; Oleksiak et al., 2016) which is consistent with the

XRD patterns. The presence of this mixed phase suggests that a longer aging time is required for the crystallization process.

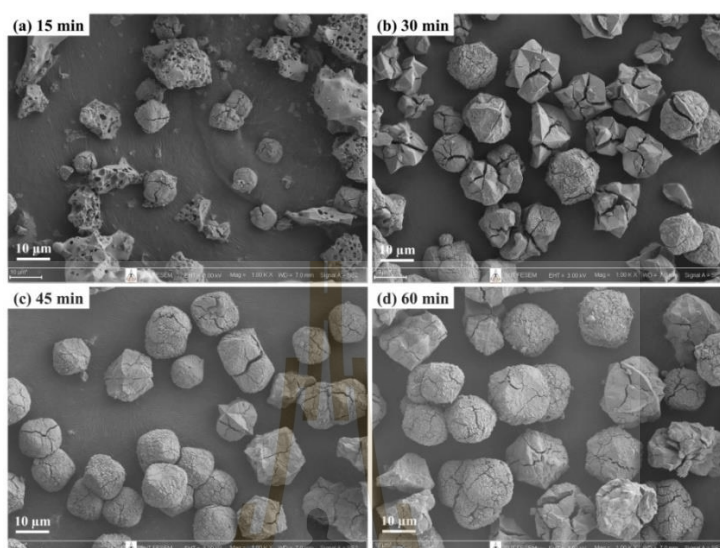


**Figure 3.4** FESEM images of zeolite products from microwave-assisted hydrothermal methods with single crystallization at 150 °C for various times: (a) 15, (b) 30, (c) 45 and (d) 60 minutes.

### 3.4.3 Effect of Double Crystallization by Microwave-Assisted Hydrothermal Methods

Figure 3.5 illustrates a comparison between the XRD patterns of MH90 and two other samples: the further aged sample (MH90A) and the sample recrystallized at 150 °C (MH90A150). The XRD patterns of MH90 and MH90A are consistent with the NaY structure, as reported by Bunmai et al. (2020). However, the peaks observed in MH90A are more intense than those in MH90, indicating that a longer aging time enhances the crystallinity of the sample. Upon crystallization at 150 °C, the XRD pattern of MH90A150 reveals the presence of pure NaP2 zeolite phase. These findings suggest that the synthesis conditions of MH90A150 are suitable for transforming the NaY zeolite gel into NaP2. Additionally, the second crystallization process, facilitated by microwave heating, leads to the depolymerization of the small building units of NaY, as reported by Sousa et al. (2018). This depolymerization results in the formation of NaP2, which possesses a denser structure.

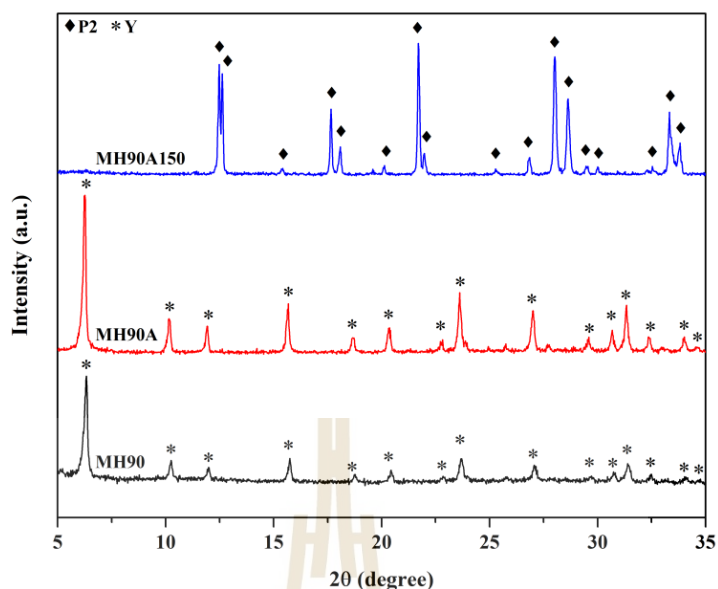


**Figure 3.5** XRD patterns of zeolites from microwave-assisted hydrothermal method at 90 °C for 1 hour (MH90), aged at room temperature for 23 hours (MH 90A) and crystallized at 150 °C for 1 hour (MH90A150).

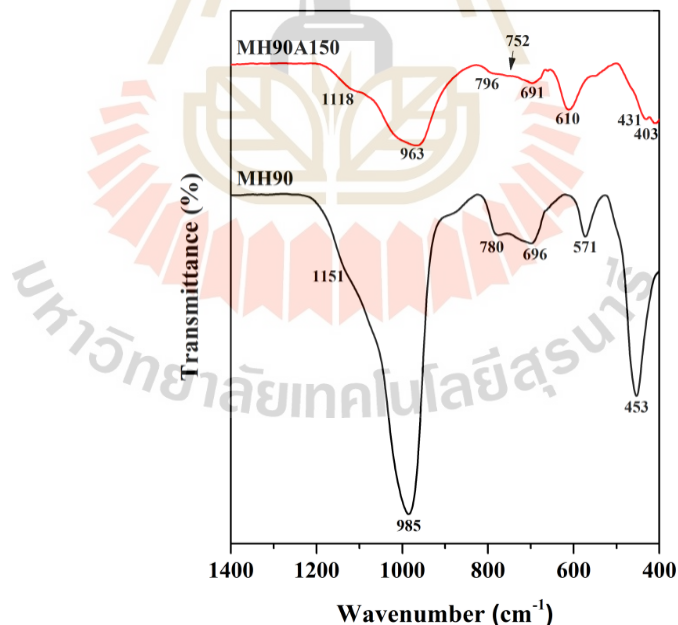


**Figure 3.6** Fourier-transform infrared spectroscopy (FTIR)–attenuated total reflectance (ATR) spectra of zeolite products: MH90 from the microwave-assisted hydrothermal method at 90 °C for 1 hour and MH90A150 from the microwave-assisted hydrothermal method at 90 °C for 1 hour followed by aging at room temperature for 23 hours and recrystallization at 150 °C for 1 hour.

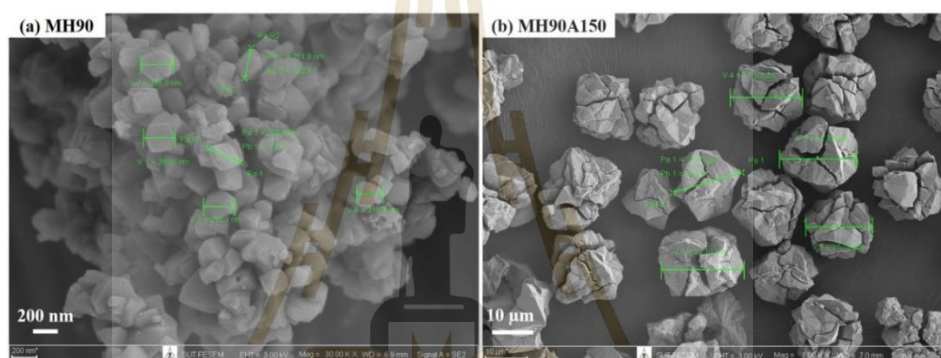
Figure 3.6 compares the FTIR spectra of MH90 and MH90A150 and the interpretations are summarized in Table 3.2. The spectra of MH90 and MH90A150 correspond to the functional groups of zeolite NaY (Kulawong et al., 2020; Mozgawa et al., 2011; Shariatinia and Bagherpour, 2018) and NaP (Chandrasekhar and Pramada, 2004; Flanigen et al., 1974; Mozgawa et al., 2011; Sharma et al., 2013), consistent with the XRD results.

**Table 3.2** Band assignment of FTIR spectra of MH90 (FAU) and MH90A150 (GIS) samples.

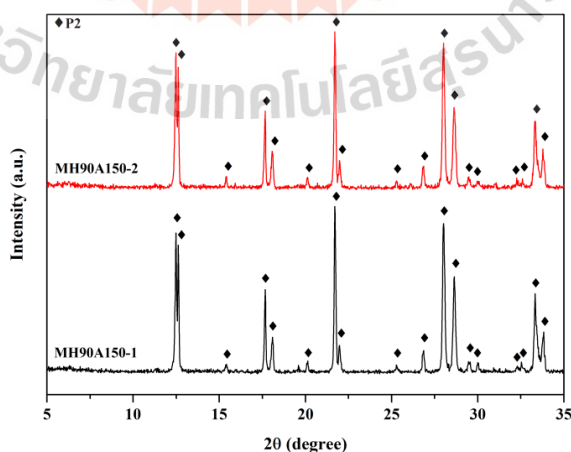
Wavenumber ( $\text{cm}^{-1}$ )	Assignment	References
FAU zeolite		
1151	Asymmetric stretching vibration of external linkage $\text{TO}_4$ (T=Si, Al)	(Kulawong et al., 2020;
985	Asymmetric stretching vibration of internal tetrahedral $\text{TO}_4$	Mozgawa et al., 2011;
780	Symmetric stretching vibration of external linkage $\text{TO}_4$	Shariatinia and
696	Symmetric stretching vibration of internal linkage $\text{TO}_4$	Bagherpour,
571	Vibration of double-6-membered ring (D6R)	2018)
453	Bending vibration of T-O bond in internal tetrahedron	
GIS zeolite		
1118	Asymmetric stretching vibration of external linkage $\text{TO}_4$	(Chandrasekhar
963	Asymmetric stretching vibration of internal tetrahedral $\text{TO}_4$	and Pramada,
796	Symmetric stretching vibrations of external linkage $\text{TO}_4$	2004; Flanigen
752	Vibration of 4-membered ring (4MR)	et al., 1974;
691	Symmetric stretching vibration of internal linkage $\text{TO}_4$	Mozgawa et
610	Double ring vibration in GIS zeolite framework	al., 2011;
431, 403	Bending vibration of T-O	Sharma et al.,
		2013)

Figure 3.7 displays the scanning electron microscope (SEM) images of MH90 and MH90A150. The morphology of MH90 (Figure 3.7a) resembles a polygon shape similar to the NaY zeolite described in the literature (Qamar et al., 2016). The average particle size of MH90 is 230 nm, and it has a Si/Al ratio of 1.88. On the other hand, the particles of MH90A150 (Figure 3.7b) also exhibit a polygonal morphology,

similar to the NaP2 zeolite reported in previous studies (Le et al., 2019; Oleksiak et al., 2016). To ensure the reproducibility of obtaining pure phase NaP2 zeolite using our synthesis method, we conducted the synthesis again following the same procedure. The similar X-ray diffraction (XRD) patterns (Figure 3.8) indicate that our synthesis method can indeed produce pure NaP2 zeolite. The average particle size of MH90A150 is 16.45  $\mu\text{m}$ , and it has a Si/Al ratio of 1.85. These results are consistent with the XRD and FTIR data. Comparing between NaP2 from CH150 and MH90A150, the particle size distribution of MH90A150 is narrower than that of CH150 (standard deviation of 7.5% vs. 27.6%).



**Figure 3.7** FESEM images of zeolites from the microwave-assisted hydrothermal method (a) at 90 °C for 1 hour (MH90), followed by aging at room temperature for 23 hours and recrystallized (b) at 150 °C for 1 hour (MH90A150).



**Figure 3.8** Powder XRD patterns of NaP2 zeolites from microwave-assisted double crystallization for repetition at the first time (MH90A150-1) and the second time (MH90A150-2).

The findings and outcomes of this study are presented in Table 3.3. The synthesis of pure phase NaP2 can be achieved through two methods: the CH method at 150 °C for 24 hours and the double crystallization method via MH at 90 °C and 150 °C. Single crystallization via MH at 90 °C resulted in pure phase NaY, while at 150 °C and 175 °C, it led to the formation of mixed phases of NaP2 and NaP1 or ANA.

**Table 3.3** Gel composition, synthesis parameters and phase of the products in this study.

Sample name	Crystallization Conditions				Phase of Product <sup>4</sup>	
	Method	Synthesis process	Temperature (°C)	Time (min)	Major	Minor
CH150	CH <sup>1</sup>	Single	150	1440	NaP2	-
MH90	MH <sup>2</sup>	Single	90	60	NaY	-
MH150	MH <sup>2</sup>	Single	150	15–60	NaP1	NaP2
MH175	MH <sup>2</sup>	Single	175	15–60	NaP2	ANA
MH90A	MH <sup>2</sup>	Single	90 and aged <sup>3</sup>	60	NaY	-
MH90A150	MH <sup>2</sup>	Double	90, 150	60, 60	NaP2	-

<sup>1</sup> CH=conventional hydrothermal method, <sup>2</sup> MH=microwave-assisted hydrothermal method, <sup>3</sup> crystallization at 90 °C followed by aging at room temperature for 23 hours, <sup>4</sup> measurement by XRD technique.

### 3.5 Conclusion

The NaY synthesis gel (10SiO<sub>2</sub>:Al<sub>2</sub>O<sub>3</sub>:4.62Na<sub>2</sub>O: 180H<sub>2</sub>O) used to prepare zeolite NaP. Pure phase of NaP2 zeolite was obtained after crystallization by conventional hydrothermal (CH) at a temperature of 150 °C for 24 hours. The resulting sample, CH150, exhibited polycrystals with various shapes, including polygons, diamond-like shapes, and some with trisecting cracks. The average particle size of the crystals was measured to be 10.3 μm, and the Si/Al ratio was determined to be 1.82.

The MH method was used to perform single crystallization, resulting in the production of different phases at varying temperatures and times. Crystallization at 90 °C for 1 hour yielded the pure phase NaY. Crystallization at 150 °C for 1 hour

resulted in a mixed phase of NaP1 (major) and NaP2 (minor), while at 175 °C, it produced a mixed phase of NaP2 (major) and ANA (minor). Additionally, when the crystallization process was conducted for various times (15-60 minutes) at 150 °C and 175 °C, mixed phases were also obtained.

In double crystallization, the pure phase zeolite NaP2 was successfully synthesized using the microwave-assisted hydrothermal (MH) method through a three-step process. Firstly, crystallization was carried out at 90 °C for 1 hour, followed by rapid cooling to room temperature in the microwave chamber. Secondly, the sample was aged at room temperature for 23 hours. Finally, a second crystallization step was performed at 150 °C for 1 hour. The resulting NaP2 sample exhibited a similar morphology to the CH150 sample, with an average crystal size of 16.45  $\mu\text{m}$  and a Si/Al ratio of 1.85.

### 3.6 References

- Albert, B. R., Cheetham, A. K., Stuart, J. A., and Adams, C. J. (1998). Investigations on P zeolites: synthesis, characterisation, and structure of highly crystalline low-silica NaP. *Microporous and Mesoporous Materials*, 21(1), 133–142.
- Ali, I. O., El-sheikh, S. M., Salama, T. M., Bakr, M. F., and Fodial, M. H. (2015). Controllable synthesis of NaP zeolite and its application in calcium adsorption. *Microporous and Mesoporous Materials*, 58(8), 621–633.
- Arrigo, I., Capri, M., Corigliano, F., Bonavita, A., Rizzo, G., Neri, G., and Donato, N. (2011). *An exploratory study on the potential of zeolite P-based materials for sensing applications BT - sensors and microsystems* (G. Neri, N. Donato, A. D'Amico, & C. Di Natale (Eds.); pp. 67–71). Springer Netherlands.
- Azizi, S. N., Alavi Daghigh, A., and Abrishamkar, M. (2013). Phase transformation of zeolite P to Y and analcime zeolites due to changing the time and temperature. *Journal of Spectroscopy*, 2013, 428216.
- Azizi, S. N., and Tilami, S. E. (2009). Recrystallization of zeolite Y to analcime and zeolite P with D-methionine as structure-directing agent (SDA). *Zeitschrift Fur Anorganische Und Allgemeine Chemie*, 635(15), 2660–2664.
- Baerlocher, C., McCusker, L. B., and Olson, D. H. (2007a). ANA -  $1a3^-d$  (C. Baerlocher, L.

- B. McCusker, & D. H. B. T.-A. of Z. F. T. (Sixth E. Olson (Eds.); pp. 46–47). Elsevier Science B.V.
- Baerlocher, C., McCusker, L. B., and Olson, D. H. (2007b). *FAU -  $Fd\bar{3}m$*  (C. Baerlocher, L. B. McCusker, & D. H. B. T.-A. of Z. F. T. (Sixth E. Olson (Eds.); pp. 140–141). Elsevier Science B.V.
- Baerlocher, C., McCusker, L. B., and Olson, D. H. (2007c). *GIS -  $I41/amd$*  (C. Baerlocher, L. B. McCusker, & D. H. B. T.-A. of Z. F. T. (Sixth E. Olson (Eds.); pp. 146–147). Elsevier Science B.V.
- Baerlocher, C., and Meier, W. M. (1972). The crystal structure of synthetic zeolite Na-P1, an isotype of gismondine. *Zeitschrift Für Kristallographie - Crystalline Materials*, 135(1–6), 339–354.
- Bunmai, K., Osakoo, N., Deekamwong, K., Kosri, C., Khemthong, P., and Wittayakun, J. (2020a). Fast synthesis of zeolite NaP by crystallizing the NaY gel under microwave irradiation. *Materials Letters*, 272, 127845.
- Bunmai, K., Osakoo, N., Deekamwong, K., Kosri, C., Khemthong, P., and Wittayakun, J. (2020b). Fast synthesis of zeolite NaP by crystallizing the NaY gel under microwave irradiation. *Materials Letters*, 272, 127845.
- Bunmai, K., Osakoo, N., Deekamwong, K., Rongchapo, W., Keawkumay, C., Chanlek, N., Prayoonpokarach, S., and Wittayakun, J. (2018). Extraction of silica from cogon grass and utilization for synthesis of zeolite NaY by conventional and microwave-assisted hydrothermal methods. *Journal of the Taiwan Institute of Chemical Engineers*, 83, 152–158.
- Chandrasekhar, S., and Pramada, P. N. (2004). Kaolin-based zeolite Y, a precursor for cordierite ceramics. *Applied Clay Science*, 27(3), 187–198.
- Dong, J., and Lin, Y. S. (1998). In situ synthesis of P-type zeolite membranes on porous  $\alpha$ -alumina supports. *Industrial & Engineering Chemistry Research*, 37(6), 2404–2409.
- Fischer, M., and Bell, R. G. (2012). Influence of zeolite topology on  $\text{CO}_2/\text{N}_2$  separation behavior: force-field simulations using a DFT-derived charge model. *The Journal of Physical Chemistry C*, 116(50), 26449–26463.

- Flanigen, E. M. (2001). Chapter 2 zeolites and molecular sieves: an historical perspective. In H. van Bekkum, E. M. Flanigen, P. A. Jacobs, & J. C. B. T.-S. in S. S. and C. Jansen (Eds.), *Introduction to Zeolite Science and Practice* (Vol. 137, pp. 11–35). Elsevier.
- Flanigen, E. M., Khatami, H., and Szymanski, H. A. (1974). Infrared structural studies of zeolite frameworks. In *Molecular Sieve Zeolites-I* (Vol. 101, pp. 16–201). AMERICAN CHEMICAL SOCIETY.
- Ginter, D. (2001). *Chapter 46 - FAU Linde type Y Si(71), Al(29)* (H. Robson & K. P. B. T.-V. S. of Z. M. Lillerud (Eds.); pp. 156–158). Elsevier Science.
- Gu, B., Bai, J., Yang, W., and Li, C. (2019). Synthesis of ANA-zeolite-based Cu nanoparticles composite catalyst and its regularity in styrene oxidation. *Microporous and Mesoporous Materials*, 274, 318–326.
- Khabuanchalad, S., Khemthong, P., Prayoonpokarach, S., and Wittayakun, J. (2008). Transformation of zeolite NaY synthesized from rice husk silica to NaP during hydrothermal synthesis. *Suranaree Journal of Science and Technology*, 15(3), 225–231.
- Kulawong, S., Chanlek, N., and Osakoo, N. (2020). Facile synthesis of hierarchical structure of NaY zeolite using silica from cogon grass for acid blue 185 removal from water. *Journal of Environmental Chemical Engineering*, 8(5), 104114.
- Le, T., Wang, Q., Pan, B., Ravindra, A. V., Ju, S., and Peng, J. (2019). Process regulation of microwave intensified synthesis of Y-type zeolite. *Microporous and Mesoporous Materials*, 284, 476–485.
- Li, Y., and Yang, W. (2008). Microwave synthesis of zeolite membranes: a review. *Journal of Membrane Science*, 316(1), 3–17.
- Maldonado, M., Oleksiak, M. D., Chinta, S., and Rimer, J. D. (2013). Controlling crystal polymorphism in organic-free synthesis of Na-zeolites. *Journal of the American Chemical Society*, 135(7), 2641–2652.
- McCusker, L. B., Baerlocher, C., and Nawaz, R. (1985). Rietveld refinement of the crystal structure of the new zeolite mineral gobbinsite. *Zeitschrift Für Kristallographie - Crystalline Materials*, 171(1–4), 281–290.

- Mozgawa, W., Król, M., and Barczyk, K. (2011). FT-IR studies of zeolites from different structural groups. *Chemik*, 65(7), 671–674.
- Nery, J. G., Mascarenhas, Y. P., and Cheetham, A. K. (2003). A study of the highly crystalline, low-silica, fully hydrated zeolite P ion exchanged with ( $Mn^{2+}$ ,  $Cd^{2+}$ ,  $Pb^{2+}$ ,  $Sr^{2+}$ ,  $Ba^{2+}$ ) cations. *Microporous and Mesoporous Materials*, 57(3), 229–248.
- Oleksiak, M. D., Ghorbanpour, A., Conato, M. T., McGrail, B. P., Grabow, L. C., Motkuri, R. K., and Rimer, J. D. (2016). Synthesis strategies for ultrastable zeolite GIS polymorphs as sorbents for selective separations. *Chemistry – A European Journal*, 22(45), 16078–16088.
- Panzarella, B., Tompsett, G. A., Yngvesson, K. S., and Conner, W. C. (2007). Microwave synthesis of zeolites. 2. effect of vessel size, precursor volume, and irradiation method. *The Journal of Physical Chemistry. B*, 111(44), 12657–12667.
- Qamar, M., Baig, I., Azad, A.-M., Ahmed, M. I., and Qamaruddin, M. (2016). Synthesis of mesoporous zeolite Y nanocrystals in octahedral motifs mediated by amphiphilic organosilane surfactant. *Chemical Engineering Journal*, 290, 282–289.
- Robson, H., and Lillerud, K. P. B. T. V. S. of Z. M. (Eds.). (2001). *Chapter 51 - GIS zeolite P Si(54), Al(46)* (pp. 169–170). Elsevier Science.
- Sathupunya, M., Gulari, E., and Wongkasemjit, S. (2002). ANA and GIS zeolite synthesis directly from alumatrane and silatrane by sol-gel process and microwave technique. *Journal of the European Ceramic Society*, 22(13), 2305–2314.
- Shariatnia, Z., and Bagherpour, A. (2018). Synthesis of zeolite NaY and its nanocomposites with chitosan as adsorbents for lead(II) removal from aqueous solution. *Powder Technology*, 338, 744–763.
- Sharma, P., Song, J. S., Han, M. H., and Cho, C. H. (2016). GIS-NaP1 zeolite microspheres as potential water adsorption material: Influence of initial silica concentration on adsorptive and physical/topological properties. *Scientific Reports*, 6(1), 22734.
- Sharma, P., Yeo, J., Han, M. H., and Cho, C. H. (2013). Knobby surfaced, mesoporous, single-phase GIS-NaP1 zeolite microsphere synthesis and characterization for  $H_2$  gas adsorption. *Journal of Materials Chemistry A*, 1, 2602–2612.

- Sousa, L. V, Silva, A. O. S., Silva, B. J. B., Quintela, P. H. L., Barbosa, C. B. M., Fréty, R., and Pacheco, J. G. A. (2018). Preparation of zeolite P by desilication and recrystallization of zeolites ZSM-22 and ZSM-35. *Materials Letters*, 217, 259–262.
- Yamni, K., Tijani, N., and Lamsiah, S. (2014). Influence of the crystallization temperature on the synthesis of Y zeolite. *IOSR Journal of Applied Chemistry*, 7(7), 58–61.
- Yang, G., and Park, S. (2019). Conventional and microwave hydrothermal synthesis and application of functional materials : a review. *Materials*, 12(7), 1177–1194.
- Yin, X., Zhu, G., Wang, Z., Yue, N., and Qiu, S. (2007). Zeolite P / NaX composite membrane for gas separation. *Microporous and Mesoporous Materials*, 105, 156–162.



## CHAPTER IV

# BIODIESEL PRODUCTION VIA TRANSESTERIFICATION OF PALM OIL OVER POTASSIUM CATALYSTS SUPPORTED ON ZEOLITE SODIUM X AND P2 FROM CONVENTIONAL AND MICROWAVE-ASSISTED HYDROTHERMAL METHODS

### 4.1 Abstract

Using zeolite as catalyst support sometimes suffers from active phase aggregates and the collapse of zeolite structure during an impregnation process resulting in low catalytic performance. Zeolite NaX is an attractive support due to its high surface area and pore volume. In this work, NaX synthesized from microwave-assisted hydrothermal (MH) method was applied to enhance the stability of the zeolite structure, which could improve the catalyst performance. Sonication was used in catalyst preparation to improve potassium dispersion and zeolite stability. Moreover, zeolite NaP2, which has a smaller pore size than reaction precursors, was applied to confirm the excellent high porosity of zeolite NaX. The results from characterization by XRD, FTIR-ATR, SEM-EDS, CO<sub>2</sub>-TPD, and N<sub>2</sub> sorption analysis revealed that zeolite from MH method had high stability. Although the catalytic performances of NaX catalysts from MH method were worse than those of the conventional hydrothermal (CH) method, their structure were more stable due to different carbonate species and catalyst basicity. Although sonication did not affect bare zeolite from CH and MH synthesis, its influences led to the collapse of the NaX structure due to the presence of potassium species, especially from CH method. This phenomenon led to different catalytic performances due to the collapse of the zeolite structure. Compared to zeolite types, the properties and yield of NaP2 catalyst from MH were not significantly different from CH. These indicate the prominence of zeolite NaX in the reaction testing.

## 4.2 Introduction

Biodiesel is an alternative energy resource to overcome many pollution problems because its combustion gives less carbon monoxide and smoke and smaller particles, which are more environmentally friendly than fossil fuel. Biodiesel can be synthesized by the transesterification reaction of alcohols and triglycerides from animal and vegetable fats under the presence of basic catalysts. Among various kinds of basic catalysts, heterogeneous catalysts prepared by loading basic species on porous materials are widely used because they can be easily separated from the reaction mixture at the end of the reaction. Moreover, they can be regenerated for the next reaction cycles. Such advantages make them more environmentally friendly than homogeneous catalysts (Lam and Lee, 2012). Among several oils, a large quantity of palm oil in Thailand can serve as raw material for biodiesel production.

Zeolites are attractive supports for basic catalysts because of their high surface area and highly uniform pores. Researchers have reported the preparation of potassium catalysts on NaX zeolite for the transesterification of plant oils (Peña et al., 2013; Supamathanon et al., 2011; Xie et al., 2007) with methanol. Xie et al. (2007) prepared the catalysts by impregnating KOH on NaX zeolite for transesterification of soybean oil. They found that 10 wt.% K/NaX catalyst gave the highest biodiesel yield of 85.6% at 65 °C in 8 h with the catalyst amount of 3 wt% and a 10:1 molar ratio of methanol to soybean oil. However, it takes a long time to reach the highest yield. In addition, the high amount of potassium loading could cause agglomeration of active phases on the support surface.

Sonication could be adopted in catalyst preparation to increase the distribution of active species on zeolite surfaces (Rakmae et al., 2016; Vafaeian et al., 2013). Rakmae et al. (2016) loaded 12 wt.% of potassium on NaY zeolite with and without sonication to prepare K/NaY-U and 12K/NaY catalysts, respectively, for transesterification of palm oil. The 12K/NaY-U gives a higher biodiesel yield at 60 °C and 2 hours compared with the 12K/NaY catalysts because of a better distribution of the active species.

Besides the agglomeration of active species, the collapse of the support structure reduces the performance of the prepared catalysts. To prevent the

mentioned problems, the potassium catalysts were prepared by impregnation with potassium acetate buffer (Manadee et al., 2017; Montalbo et al., 2013; Rakmae et al., 2016; Supamathanon et al., 2011). The catalysts with 4, 8, 12, 16 wt.% of potassium loaded on NaX for transesterification of jatropha seed oil were prepared (Manadee et al., 2017). The results showed that the 16 wt.% K/NaX catalyst gives the highest biodiesel yield of 95.2% at 60 °C for 3 hours resulting from the highest basicity. Despite high biodiesel yield, the more significant collapses of NaX structure were observed according to higher potassium loading. Moreover, the collapse of the structure with the presence of high yield raises a question of catalytic performance on zeolite porosity after loading with potassium in the reaction. Another effort for reducing the structural collapse of the support is the synthesis of zeolite by microwave heating method. There is a report that zeolite from microwave-assisted hydrothermal method has a higher thermal stability compared with zeolite from conventional hydrothermal method (Le et al., 2019). Consequently, this alternative method to preserve the potassium catalyst's support structure

In this work, the NaY support was replaced by NaX. Both zeolites have a FAU-type structure, but NaX has higher Al incorporation and higher basicity. NaX zeolite was synthesized by the microwave-assisting hydrothermal method and the catalyst was prepared with sonication. Both approaches were expected to improve the catalytic performance of the potassium catalyst in the transesterification of palm oil. The effect of sonication on the properties and catalytic performance of the potassium catalysts on NaX-MH in the transesterification of palm oil compared with those on NaX-CH were investigated. Additionally, NaP2 zeolite, which has a smaller pore size than reaction precursor and carbonate active species, was compared to investigate the effect of zeolite pore size after potassium loading.

## 4.3 Materials and Methods

### 4.3.1 Chemicals

Chemicals used in this work were fumed silica ( $\text{SiO}_2$ , 99%, Carlo Erba), sodium hydroxide pellet (NaOH, analytical grade, Carlo Erba), sodium aluminate ((NaAlO<sub>2</sub> containing Al<sub>2</sub>O<sub>3</sub> ~55–56%, Riedel-de Haën<sup>®</sup>), potassium acetate (CH<sub>3</sub>COOK,

99%, Carlo Erba), methanol ( $\text{CH}_3\text{OH}$ , Carlo Erba), and palm oil (commercial palm oil, Morakot). Additionally, n-hexane ( $\text{CH}_3(\text{CH}_2)_4\text{CH}_3$ , 99.0%, CRI Labscan), standard methyl nonadecanoate (C19-internal standard, Sigma-Aldrich), and standard fatty acid methyl ester, (C8-C24, Sigma-Aldrich) were used in product analysis. In addition, synthesized zeolite NaP2 from CH and MH methods in Chapter III were applied in this study as named CHP2 and MHP2, respectively.

#### 4.3.2 Synthesis of NaX supports via CH and MH

The molar composition of the synthesis gel of NaX from both CH and MH methods was  $\text{NaAlO}_2: 4\text{SiO}_2: 16\text{NaOH}: 325\text{H}_2\text{O}$ , following the literature (Jantarit et al., 2020). For CHX by conventional hydrothermal method (CH), the gel in a 250-mL PP bottle was transferred to an oven and crystallized at 90 °C for 18 hours. For MHX by microwave-assisted hydrothermal method (MH), 30 mL of the reaction gel was transferred to a 100-mL Teflon vessel and crystallized at 90 °C for 2.5 hours by Multiwave 3000, Anton Paar with a frequency 2.5 GHz, power 900 W, and XF-100 rotor. Both samples were separated by centrifugation, washed with DI water, and dried at 110 °C for 24 hours.

#### 4.3.3 Preparation of potassium catalysts

NaX and NaP2 supports (CHX, MHX, CHP2, MHP2) were dried before use in a vacuum oven at 120 °C for 2 hours to eliminate adsorbed impurities. Potassium acetate solution was prepared by dissolving potassium acetate (2.225 g,  $\text{CH}_3\text{COOK}$ , 99%, Carlo Erba) in deionized water and the final volume was adjusted to 25.00 mL. Six weight percent of potassium catalysts were prepared by impregnation adapted from the literature (Rakmae et al., 2016) to obtain K/zeolite in various types. Potassium acetate solution (1.8 mL) was added dropwise on 1.0 g of dried zeolites to produce a well-mixed slurry. Then, it was aged without sonication for 10 minutes. To investigate the effect of sonication, Ultrasonication (U) was applied in this part. Only zeolite NaX samples were sonicated under an ultrasound generator with a frequency of 28 kHz and power of 100W for 10 minutes. After that, the obtained mixtures were dried in the vacuum oven at 100 °C for 6 hours and calcined at 550 °C for 3 hours under atmosphere. The catalysts without sonication were designated K/CHX, K/MHX, K/CHP2 and K/MHP2. The samples with sonication were named K/CHX-U and K/MHX-U. The

control catalysts were prepared by dropping water into the zeolite supports instead of the potassium acetate solution with and without sonication.

#### 4.3.4 Catalyst characterization

The remaining phase of the supports from fresh and spent catalysts was determined by X-ray diffraction (XRD) using a Bruker D8 ADVANCE with Cu K $\alpha$  radiation ( $\lambda = 1.5418 \text{ \AA}$ ) operating at the voltage of 40 kV and the current of 40 mA. The XRD patterns were collected at 2 $\theta$  of 5-50 degree with an increment of  $0.02^\circ$  at a scan rate of 0.2 s/step. The relative crystallinity of the catalysts was estimated by following equation 4.1:

$$\text{Relative crystallinity (\%)} = \frac{\text{The sum of peak area of potassium catalyst}}{\text{The sum of peak area of bare support}} \times 100 \quad (4.1)$$

The morphology and chemical compositions of the catalysts were investigated by scanning electron microscopy (SEM) with energy-dispersive X-ray spectroscopy (EDS) using JEOL JSM 7800F field-emission scanning electron microscope (FE-SEM). The samples were spread on a carbon tape and coated with gold by sputtering. Functional groups of zeolite support and active species were analyzed by Fourier-transform infrared spectroscopy (FTIR) on a Bruker Tensor 27 using attenuated total reflectance (ATR) mode with a resolution of  $4 \text{ cm}^{-1}$  for 64 scans.

The basicity of the obtained catalysts was determined by carbon dioxide temperature-programmed desorption (CO<sub>2</sub>-TPD) in a Belcat-B equipped with a thermal conductivity detector (TCD). Each catalyst (50 mg) was loaded into a tubular U-shaped quartz cell. The prepared sample was preheated at  $300^\circ\text{C}$  under a He atmosphere with a flow rate of 50 mL/min for 600 min to eliminate physisorbed species and cooled to  $70^\circ\text{C}$ . Next, the sample was constantly flowed by a CO<sub>2</sub>/Ar gas mixture with 50 mL/min for 30 min to saturate the sample. Then, the saturated sample was purged with He for 30 minutes, heated to  $100^\circ\text{C}$  with a rate of  $10^\circ\text{C}/\text{min}$ , and held for 3 hours to remove physisorbed CO<sub>2</sub> species. The amount of desorbed CO<sub>2</sub> measurement was detected from 130 to  $800^\circ\text{C}$  with a heating rate of  $10^\circ\text{C}/\text{min}$  under

a flow of He gas. The amount of basicity was calculated from the peak area compared with that of a bared support.

Surface area and pore volume of the samples were determined by N<sub>2</sub> adsorption/desorption analysis. One hundred milligrams of the samples were characterized using a Micromeritics ASAP 2020 at -196 °C (77 K). Prior to the analysis, each sample was degassed at 350 °C under vacuum for 5 hours. The obtained data were calculated using t-plot for micropore surface area and volume, Brunauer-Emmett-Teller (BET) for specific surface area, and Barrett-Joyner-Halenda (BJH) method for mesopore volume.

#### 4.3.5 Transesterification reaction

Transesterification of palm oil and methanol for testing the catalyst performance was adapted from the procedure reported by Manadee et al. (2017) and Rakmae et al. (2016). Firstly, palm oil (5.0 g), methanol (2.9 g) and the prepared catalyst (0.2 g) were mixed in a 50-mL round-bottom flask equipped with a reflux condenser. The mixture was heated to 60 °C for 3 hours in a silicon oil bath with stirred magnetically at 250 rpm. After finished, the reaction mixture was cooled down to room temperature. Then, the catalyst was separated from the liquid mixture by centrifugation at 4500 rpm for 5 min. The biodiesel in the top layer was collected and the remaining methanol was removed in a rotary evaporator at 65 °C. The remaining liquid was transferred to a separatory funnel and placed in a hood to lead the phase separation of the biodiesel and glycerol. Only the biodiesel phase was further analyzed to determine the compositions by the internal standard method using an Agilent 7890 series gas chromatography equipped with a flame ionization detector (FID) and capillary column (non-polar, polyethylene glycol (PEG) packing material, and DB-wax stationary phase). The column temperature was operated with initial temperature at 70 °C for 4 minutes, ramped to 175 °C with a rate of 13 °C/min and held for 27 minutes, then, ramped to 215 °C with a rate of 4 °C/min and held for 17 minutes and finally, ramped to 240 °C with a rate of 4 °C/min and held for 10 minutes at the final temperature. The total biodiesel yields were determined by equation 4.2:

$$\text{Biodiesel yield (\%)} = \frac{C_{\text{ester}} \times n}{\rho_{\text{oil}}} \times 100 \quad (4.2)$$

Where  $C_{\text{ester}}$  (g/mL) is a mass concentration of methyl ester determined by GC,  $n$  is a dilution factor of methyl ester which can be calculated by the total volume of hexane and methyl ester divided by the volume of methyl ester, and  $\rho_{\text{oil}}$  (g/mL) is the density of the reactant palm oil.

## 4.4 Results and Discussion

### 4.4.1 Catalyst characterizations

XRD patterns of all catalysts are shown in Figure 4.1. The patterns of all potassium catalysts are similar to those of the bare supports but significantly lower in intensity, as shown in Figure 4.1a-c. A possible reason for the lower peak intensities of potassium catalysts is that active species cover zeolite crystal planes. Another possibility could be due to the decrease in crystallinity of the supports, which could result from the hydrolysis of Si-O-Al bonds in the presence of potassium species during the calcination process (Montalbo et al., 2013; Rakmae et al., 2016). Additionally, the splitting XRD peaks in Figure 4.1c of potassium catalyst supported on NaP2 zeolite indicate distorted zeolite NaP2 structure. This phenomenon occurs due to the zeolite flexibility of NaP2 with unfamiliar active species (Oleksiak et al., 2016). However, the patterns of all catalysts do not observe the peaks corresponding to potassium phases. This result indicated that potassium species had good distribution on the support surfaces.

Moreover, when comparing the relative crystallinities of potassium catalysts from different supports, as shown in Table 4.1, the relative crystallinities of the potassium catalysts from MH were higher than those of the catalysts from CH, resulting from higher structural stability of MHX and MHP2 than others. It could be that zeolite NaX and NaP2 prepared by MH method rapidly formed nuclei and completely grown crystals under highly uniform heat (Le et al., 2019), leading to high crystallinity and stability.

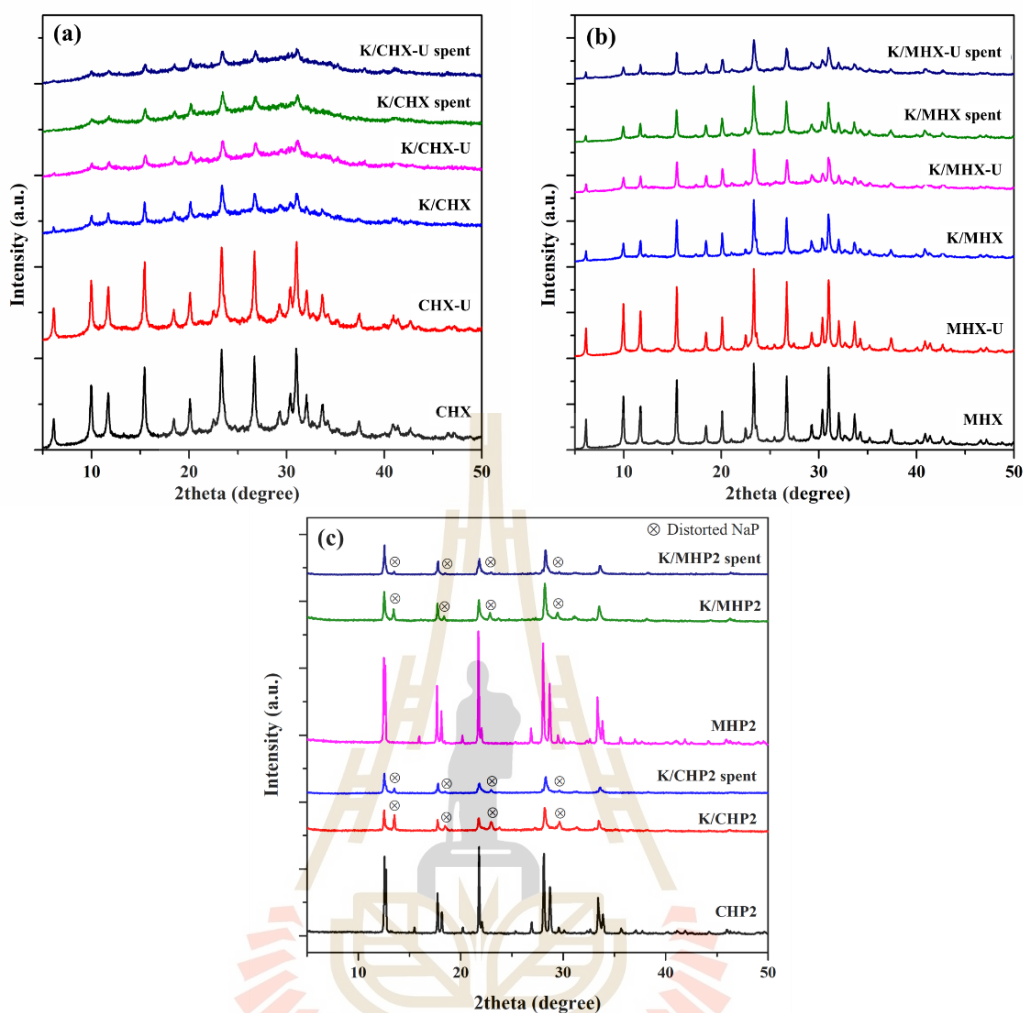


**Figure 4.1** XRD patterns fresh and spent (S) catalysts on zeolite NaX from (a) CH and (b) MH methods, and (c) zeolite NaP<sub>2</sub>.

In addition, the crystallinities of bare zeolite NaX with and without ultrasonication were not significantly different, as shown in Figure 4.1a-b. The intensity of K/CHX-U and K/MHX-U with sonication slightly drops compared with K/CHX and K/MHX, respectively. Thus, ultrasonication does not significantly affect the zeolite NaX structure. Nevertheless, it influences the zeolite structure with the presence of K species by hydrolysis of the Si-O-Al bond (Montalbo et al., 2013). However, after testing the transesterification reaction, the peak intensities of all spent catalysts were not different from those of the fresh catalysts. This result indicated that NaX supports from both synthesis methods were thermally stable and could be used as catalyst support.

**Table 4.1** Relative crystallinity of the potassium catalysts.

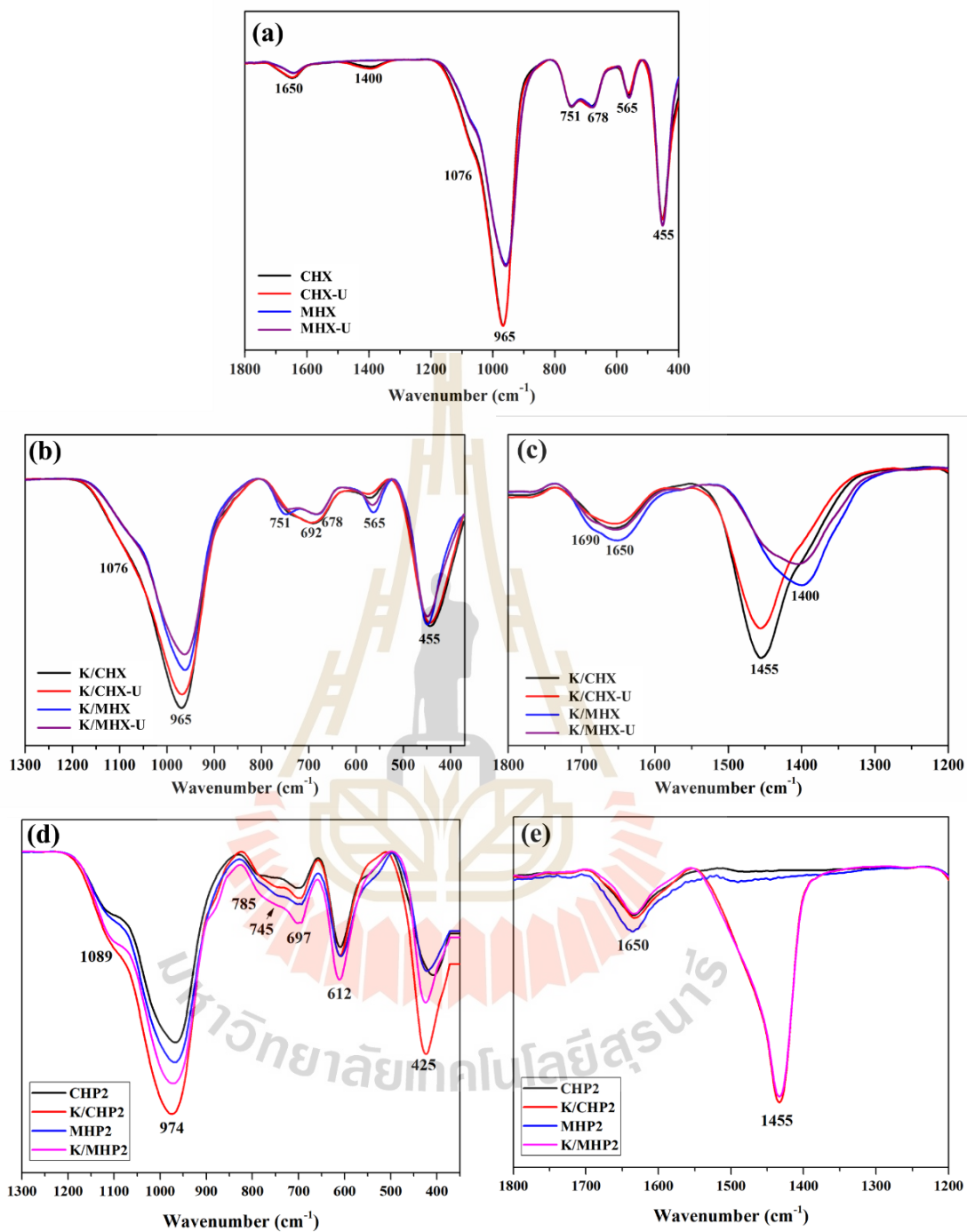
Sample	Relative crystallinity (%)
K/CHX	37.2
K/CHX-U	32.5
K/MHX	66.7
K/MHX-U	56.4
K//CHP2	40.5
K/MHP2	48.5

Figure 4.2 shows FTIR spectra of all samples. The vibrations of functional groups of the samples are assigned as shown in Table 4.2. The spectra of the bare supports with and without sonication (Figure 4.2a) are similar to that of NaX in the literature (Zhou et al., 2018). In addition, the additional peak at  $1400\text{ cm}^{-1}$  of CHX and CHX-U corresponds to the vibrational mode of carbonate (Busca and Lorenzelli, 1982; Coenen et al., 2018), while that peak were not observed in the spectra of MHX and MHX-U. This result indicates that CHX support could strongly adsorb  $\text{CO}_2$  while MHX does not. Figure 4.2b shows the spectra of the potassium catalysts in a region of  $1300\text{--}350\text{ cm}^{-1}$ . The spectrum features at  $678$  and  $751\text{ cm}^{-1}$  of K/MHX and K/MHX-U were quite similar to those of the bare supports indicating the remaining NaX structure after impregnation with potassium acetate solution. On the other hand, the spectra of K/CHX and K/CHX-U show a broader peak at  $692\text{ cm}^{-1}$  compared with the bare supports resulting from a partial collapse of NaX support from CH. In addition, the lower spectral intensity of the catalysts with sonication compared with those of the catalysts without sonication could be from accelerating the collapse of NaX structure by sonication in the presence of potassium species, consistent with the XRD result.

Figure 4.2c shows the spectra of all potassium zeolite NaX catalysts in a region of  $1800\text{--}1200\text{ cm}^{-1}$ . The spectral features of the CH catalysts significantly differ from those of MH. The spectra of K/MHX and K/MHX-U exhibit peaks at  $1400$  and  $1690\text{ cm}^{-1}$  corresponding to mono- and bidentate potassium carbonate, respectively (You et al., 2015), while the K/CHX and K/CHX-U spectra show the peaks at  $1455$  and  $1690\text{ cm}^{-1}$  assigned to free potassium carbonate (Coenen et al., 2018; Prescott et al., 2005)

and bidentate potassium carbonate, respectively. These results indicate different coordination of potassium carbonate species on both NaX supports, which could affect the basicity of the catalysts. The presence of free carbonate species in the K/CHX and K/CHX-U could imply that there is no interaction between the active species and zeolite NaX from CH, which may cause by the collapse of NaX structure. Consequently, the FTIR results indicate that the coordination types of the active phases depend on NaX stability.

Figure 4.2d reveals the vibration feature of zeolite NaP2 according to the literature (Chandrasekhar and Pramada, 2004; Flanigen et al., 1974; Mozgawa et al., 2011; Sharma et al., 2013). Peaks at 612, and 745  $\text{cm}^{-1}$  indicate double ring vibration in GIS zeolite framework and vibration of 4MR, respectively. In contrast to zeolite NaX results, Figure 4.2e shows FTIR of NaP2 catalysts in the range of 1800-1200  $\text{cm}^{-1}$ . There is no difference between CHP2 and MHP2 vibration. The peaks at 1400  $\text{cm}^{-1}$  were observed in both supports, indicating no  $\text{CO}_2$  physisorption in the zeolite NaP2 structure due to its smaller pore size than the kinetic diameter of  $\text{CO}_2$  (Oleksiak et al., 2016). Furthermore, it is worth noting that in both K/CHP2 and K/MHP2, the sole peak observed corresponds to the free carbonate species at 1455  $\text{cm}^{-1}$ . Consequently, the carbonate species bonded with MHP2 support exhibit a weaker interaction than MHX. This disparity arises because the carbonate is unable to traverse the GIS cage. Still, it can penetrate the FAU supercage, leading to the formation of mono- and bi-carbonate species on MHX support. This phenomenon has direct implications for the strength of zeolites NaP2. Table 4.1 also reveals a slight difference in relative crystallinity between K/CHP2 and K/MHP2 because unfamiliar species cannot disturb the structure.



**Figure 4.2** FTIR-ATR spectra of (a) the bare NaX zeolite, the potassium catalyst of zeolite NaX in a range of (b) 1300-350 cm<sup>-1</sup>, (c) 1800-1200 cm<sup>-1</sup>, and related catalyst of zeolite NaP2 in a range of (d) 1300-350 cm<sup>-1</sup>, (e) 1800-1200 cm<sup>-1</sup>.

**Table 4.2** Vibration modes and peak assignments of Zeolite X, Zeolite P2, H<sub>2</sub>O, and K<sub>2</sub>CO<sub>3</sub>.

Wavenumber (cm <sup>-1</sup> )	Assignment	References
<hr/>		
K <sub>2</sub> CO <sub>3</sub>		(You et al., 2015);
1400	Vibration of monodentate carbonate	(Coenen et al., 2018;
1690	$\nu$ of C=O bond in bridging bidentate carbonate	Prescott et al., 2005)
1455	$\nu_{as}$ of OCO bond in free carbonate	
<hr/>		
H <sub>2</sub> O		(Linares et al., 2008)
1650	$\delta_s$ of O-H bond of water	
<hr/>		
Zeolite X		(Zhou et al., 2018);
455	$\delta$ of tetrahedral TO <sub>4</sub> (T=Si, Al)	(Kwaky-Awuah et al.,
565	Vibration of double-6-ring (D6R)	2016)
678, 751	External linkage vibrations of the FAU structure	
965, 1076	$\nu_{as}$ of Si-O bond of tetrahedron	
692	$\delta$ of T-O tetrahedral	
<hr/>		
Zeolite P2		(Chandrasekhar and
425	$\delta$ of tetrahedral TO <sub>4</sub>	Pramada, 2004; Flanigen
612	Double ring vibration in GIS zeolite framework	et al., 1974; Mozgawa et
697	$\nu_s$ of internal linkage TO <sub>4</sub>	al., 2011; Sharma et al.,
745	Vibration of 4-membered ring (4MR)	2013)
785	$\nu_s$ of external linkage TO <sub>4</sub>	
974	$\nu_{as}$ of internal tetrahedral TO <sub>4</sub>	
1089	$\nu_{as}$ of external linkage TO <sub>4</sub>	
<hr/>		

Morphologies and surface roughness of all samples based on NaX zeolite are exhibited in Figure 4.3. There is no agglomeration of any particles on the support surfaces implying good dispersion of active species. The morphology and surface roughness of the same bare supports with and without sonication are similar as shown in Figure 4.3a-d. The morphologies of the potassium catalysts are quite similar to those of the bare supports, as shown in Figure 4.3e-h. However, their surfaces are corrosive due to the hydrolysis of NaX structure in the presence of potassium species or others which lose from the catalyst structure. Moreover, the support surfaces of the sonicated catalysts, including K/CHX-U and K/MHX-U are rougher and more corrosive than those without sonication. These results are consistent with the XRD and FT-IR results that applying sonication without potassium species does not affect the collapse of both NaX-CH and NaX-MH structures, while sonication accelerates the hydrolysis of Si-O-Al bond, resulting in a more collapsed structure of NaX as mentioned above. Moreover, NaX-CH crystals from K/CHX-U partially lose their edges, whereas those of NaX-MH from K/MHX-U remain. This result could imply the heavier collapse of the NaX-CH structure compared with the NaX-MH structure. Consequently, the result could confirm that NaX-MH is more stable than NaX-CH.

Figures 4.4a-d also reveal SEM images of support and NaP<sub>2</sub>-based potassium catalyst. Polygonal morphology was observed in all NaP<sub>2</sub> catalysts. Samples from MH have a larger size than CH due to the fast crystallization rate under microwave radiation. Cracks along the crystalline line are observed in bare zeolites (Figure 4.4a-b), while fracture on the zeolite surface was noticed in K/CHP<sub>2</sub> and K/MHP<sub>2</sub> catalysts (Figure 4.4c-d). In addition, Figure 4.4c shows weathered sticks on the surface of zeolite NaP<sub>2</sub>. Energy dispersive X-ray spectroscopy (EDS) with point analysis in Figure 4.4e determined the composition of the stick, which had a high weight percent of sodium. Adulterated things, which consisted of sodium and potassium, were also observed on the surface of NaP<sub>2</sub> in K/MHP<sub>2</sub>, as revealed in Figure 4.4d, but in lesser amounts than K/CHP<sub>2</sub>. This result indicates the hydrolysis of Si-O-Al bond, resulting in a more collapsed structure of NaP<sub>2</sub> in K/CHP<sub>2</sub>. The results correspond to its XRD patterns and results in the case of zeolite NaX.

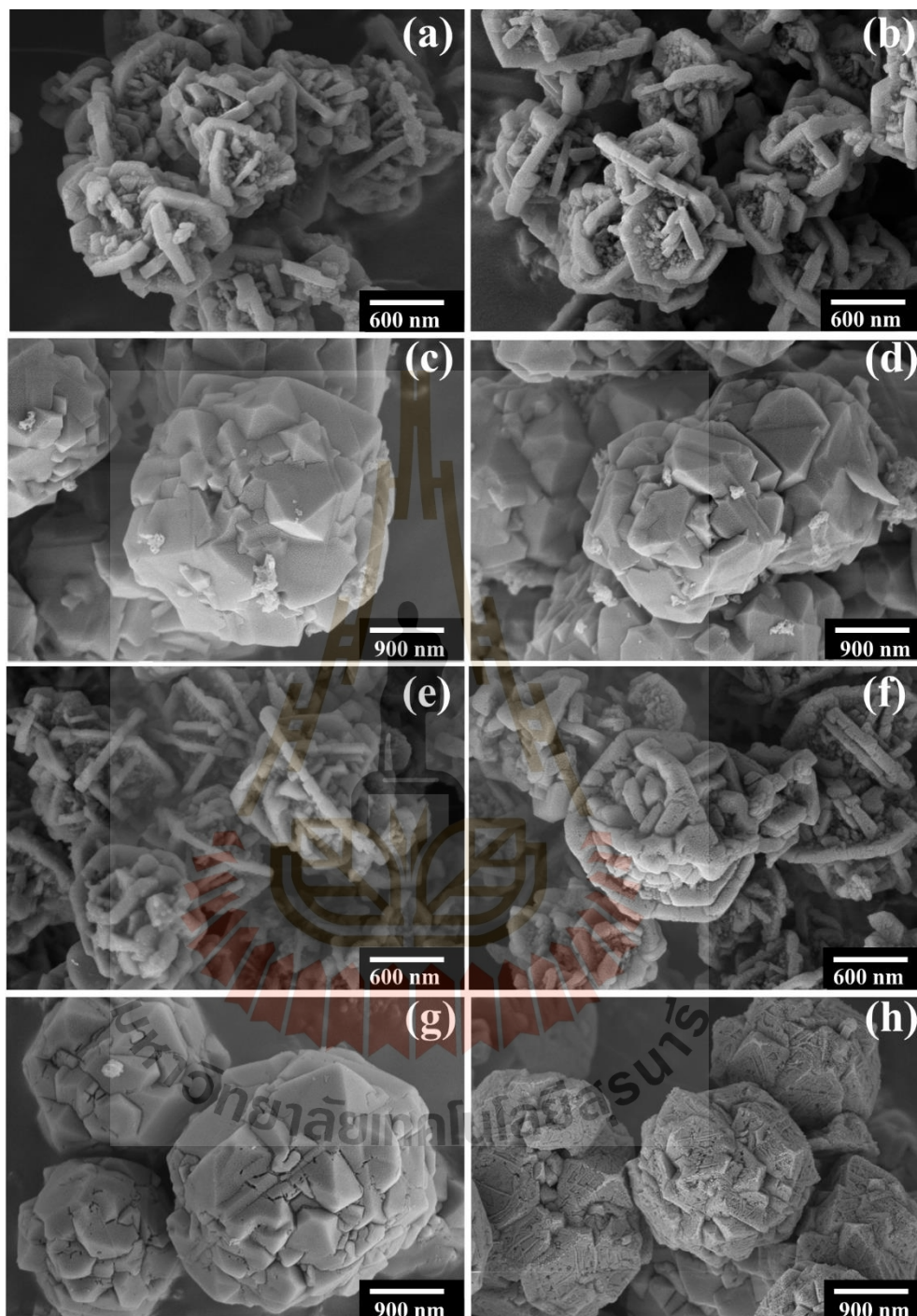


**Figure 4.3** SEM images of (a) CHX, (b) CHX-U, (c) MHX, (d) MHX-U, (e) K/CHX, (f) K/CHX-U, (g) K/MHX, and (h) K/MHX-U.

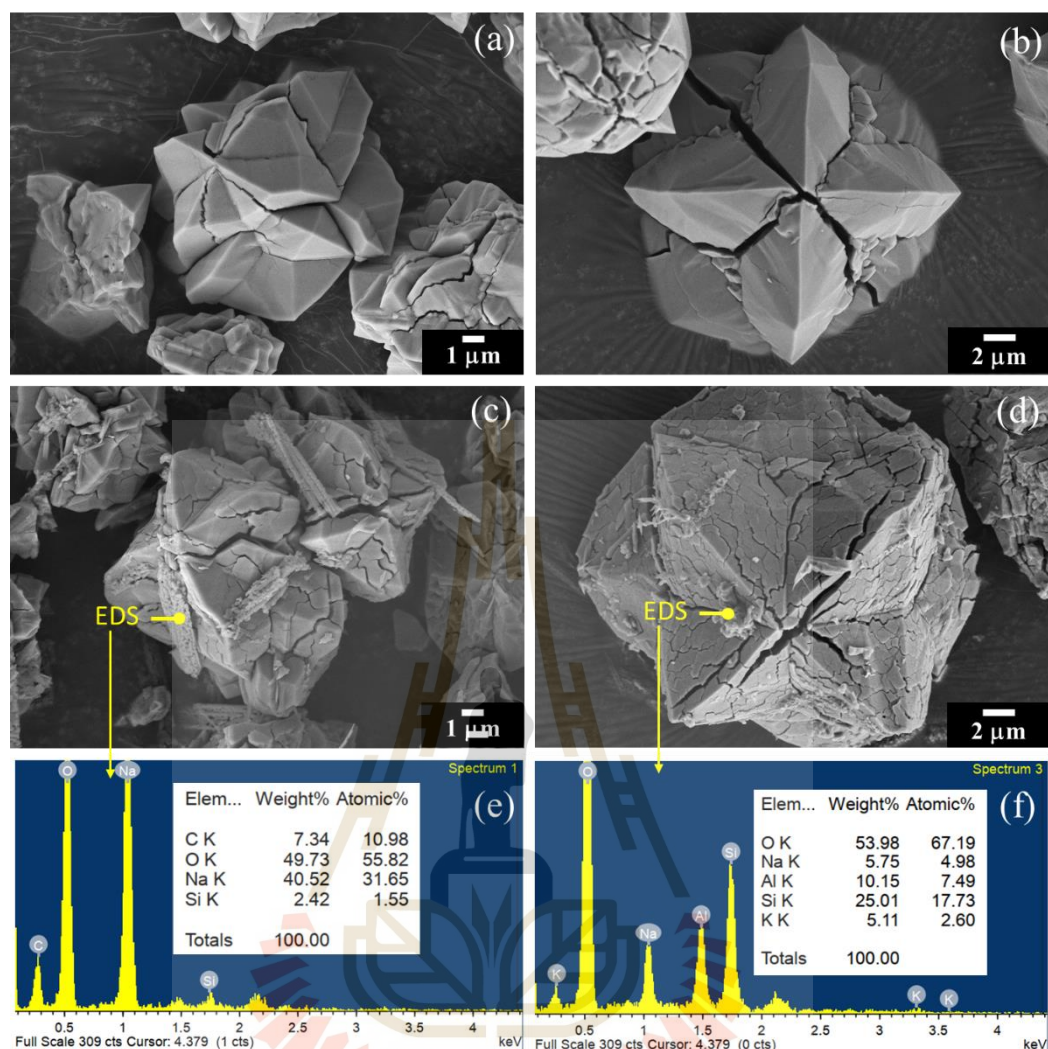


Figure 4.4 SEM images of (a) CHP2, (b) MHP2, (c) K/CHP2, (d) K/MHP2 and energy dispersive X-ray spectroscopy (EDS) of (e) K/CHP2, (f) K/MHP2.

#### 4.4.2 Determination of basicity and textural parameters of the catalysts

The CO<sub>2</sub> TPD profiles of all potassium catalysts are similar, as shown in Figure 4.5. Their profiles contain three peak regions, including a small peak between 100-200 °C, a broad peak between 200-550 °C and a large between 550-750 °C. These peaks corresponded to weak, medium and strong basic sites, respectively (Rakmae et al., 2016). The basicity and textural parameters of all catalysts are listed in Table 4.3. Loading potassium on the supports enhances the total basicity of the catalysts. The highest total basicity of 671 mmol/g is from K/CHX, which may be from the presence of free carbonate, higher surface areas and pore volume compared with K/CHX-U. In

the case of the potassium catalysts from NaX-MH support, the total basicity of K/MHX and K/MHX-U are similar. However, K/MHX has a higher micropore volume and surface but lower mesopore volume and surface than K/MHX-U. These results confirm the enhancement of the NaX structural collapse by sonication in the presence of potassium which generates higher mesopore in K/MHX-U as expected. Moreover, the results could also imply that mesopore and micropore affect the basicity of the catalysts.

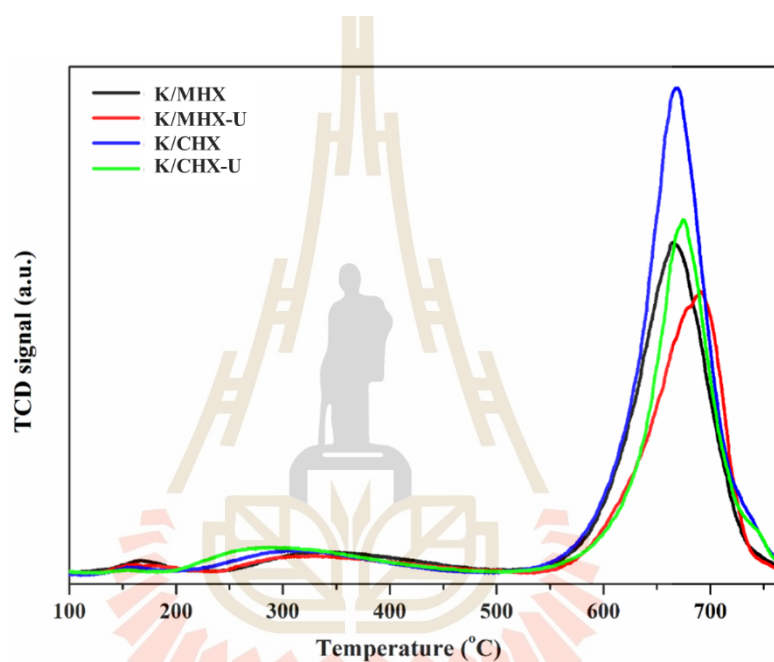


Figure 4.5 CO<sub>2</sub> TPD curves of K-impregnated NaX catalysts.

The sonication leads to a largely decrease of both micropore and mesopore of the catalysts on NaX-CH due to the low stability of the zeolite structure. On the other hand, the sonication reduces the micropore but enhances the mesopore of the catalysts from NaX-MH. It could imply that the sonication causes a partial collapse of the NaX-MH structure generating the additional mesopore. The additional mesopores could improve the diffusion of the reactants and products.

However, CO<sub>2</sub>-TPD and N<sub>2</sub> adsorption-desorption NaP2 catalysts were not measurable, as shown in Table 4.3. Gases cannot enter the NaP2 cavity because the kinetic diameters of those gases are larger than the pore size. So, this can confirm that methanol and triglyceride cannot flow into the pores of NaP2.

**Table 4.3** Basicity and textural parameters of all catalysts from CO<sub>2</sub>-TPD and N<sub>2</sub> sorption analysis, respectively.

Sample	<sup>a</sup> S <sub>BET</sub> (m <sup>2</sup> /g)	<sup>b</sup> S <sub>Micro</sub> (m <sup>2</sup> /g)	<sup>c</sup> S <sub>Ext</sub> (m <sup>2</sup> /g)	<sup>d</sup> V <sub>meso</sub> (m <sup>3</sup> /g)	<sup>e</sup> V <sub>Micro</sub> (m <sup>3</sup> /g)	Basicity (mmol/g)
CHX	703	550	153	0.271	0.26	0.170
CHX-U	241	152	89	0.183	0.07	0.146
MHX	453	442	11	0.023	0.23	0.185
MHX-U	429	417	12	0.027	0.23	0.158
K/CHX	39	2	37	0.122	0.00	0.671
K/CHX-U	21	4	17	0.093	0.00	0.516
K/MHX	119	92	27	0.051	0.04	0.532
K/MHX-U	77	37	41	0.079	0.01	0.531
CHP2	0.6	1	0.6	-	0.00	-
MHP2	-	-	1.7	-	-	-

<sup>a</sup>S<sub>BET</sub>: specific surface area calculated by the BET method, <sup>a</sup>S<sub>Micro</sub>: surface area of micropore calculated by the *t*-plot method, <sup>c</sup>S<sub>Ext</sub>: external surface area., <sup>d</sup>V<sub>Mes</sub>: Mesopore volume calculated by the BJH method., <sup>e</sup>V<sub>Mic</sub>: Micropore volume calculated by the *t*-plot method.

#### 4.4.3 Catalytic performance via transesterification of palm oil

Figure 4.6a-b reveals GC chromatograms of hexane and mixed methyl ester from C8 – C24 which are solvent and standard for biodiesel investigation, respectively. The details of the commercial standard are included in Table 4.4. Moreover, the type of biodiesel product over potassium catalyst is also observed in Figure 4.6c. The number of methyl ester products is in the range of C8 – C18 and C16 - C18 are the main products from the reaction.

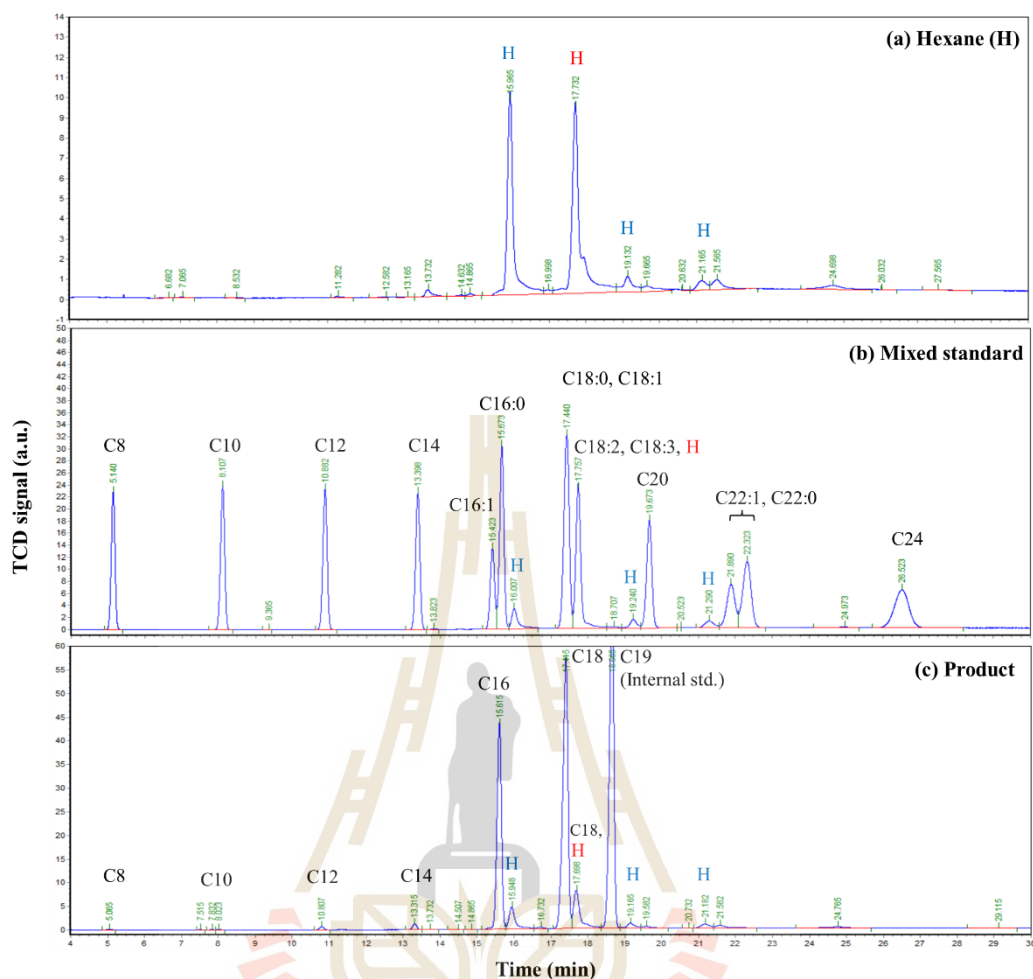


**Figure 4.6** GC chromatogram of (a) hexane, (b) standard of mixed methyl esters, and (c) biodiesel product over potassium catalyst operating at 60 °C for 3 h.

The biodiesel yields from all catalysts and bare supports are shown in Figure 4.7a. The yields of CHX and CHX-U are higher than those of MHX and MHX-U, which could be from the higher amount of mesopore for enhancing the diffusion of reactants and products during the reaction. When comparing the yield and basicity of the bare supports with and without sonication, there were slightly different, implying that sonication did not affect these properties of the bare supports.

**Table 4.4** Retention time, type of methyl ester, number of carbon atoms in each product, and certified value of the mixed standard.

No.	Retention time	Type of methyl ester	Number of C atom	Certified value $\pm$ SD (wt.%)
1	5.1	Methyl octanoate	C8	7.99 $\pm$ 0.27
2	8.1	Methyl decanoate	C10	7.99 $\pm$ 0.27
3	10.9	Methyl laurate	C12	7.99 $\pm$ 0.26
4	13.4	Methyl myristate	C14	8.00 $\pm$ 0.28
5	15.4	Methyl palmitoleate	C16:1	5.00 $\pm$ 0.18
6	15.7	Methyl palmitate	C16:0	11.0 $\pm$ 0.4
7	17.4	Methyl stearate, Methyl cis-9 oleate	C18:0, C18:1	7.98 $\pm$ 0.28, 4.98 $\pm$ 0.18
8	17.8	Methyl linoleate, Methyl linolenate	C18:2, C18:3	4.95 $\pm$ 0.19 4.95 $\pm$ 0.18
9	19.6	Methyl arachidate	C20	7.99 $\pm$ 0.24
10	21.9	Methyl erucate	C22:1	4.97 $\pm$ 0.14
11	22.3	Methyl behenate	C22:0	7.92 $\pm$ 0.20
12	26.5	Methyl lignocerate	C24	7.99 $\pm$ 0.18

Compared to the catalytic performance of the catalysts from the same support, the catalysts without sonication, K/CHX and K/MHX, provide higher yields compared with the catalysts with sonication (K/CHX-U and K/MHX-U) due to the collapse of zeolite NaX structure by the sonication. The biodiesel yield in the catalysts from NaX-MH (about 10%) was lower than that from NaX-CH (about 20%), which might be from the more stable structure of NaX-MH. However, the biodiesel yields of the potassium catalysts from NaX-CH are largely higher than those from NaX-MH. The main active species on K/CHX and K/CHX-U might be free potassium carbonate which could provide high basicity and behaves like a homogeneous catalyst, while the active phases on K/MHX and K/MHX-U are mono- and bidentate carbonates, which provided lower catalytic performance. Although the basicities of K/MHX and K/MHX-U were not significantly different, the yield of K/MHX was higher than that of K/MHX-U, possibly

due to higher micropore compared with K/MHX-U. It could imply that the micropore of zeolite plays a crucial role in the transesterification reaction.

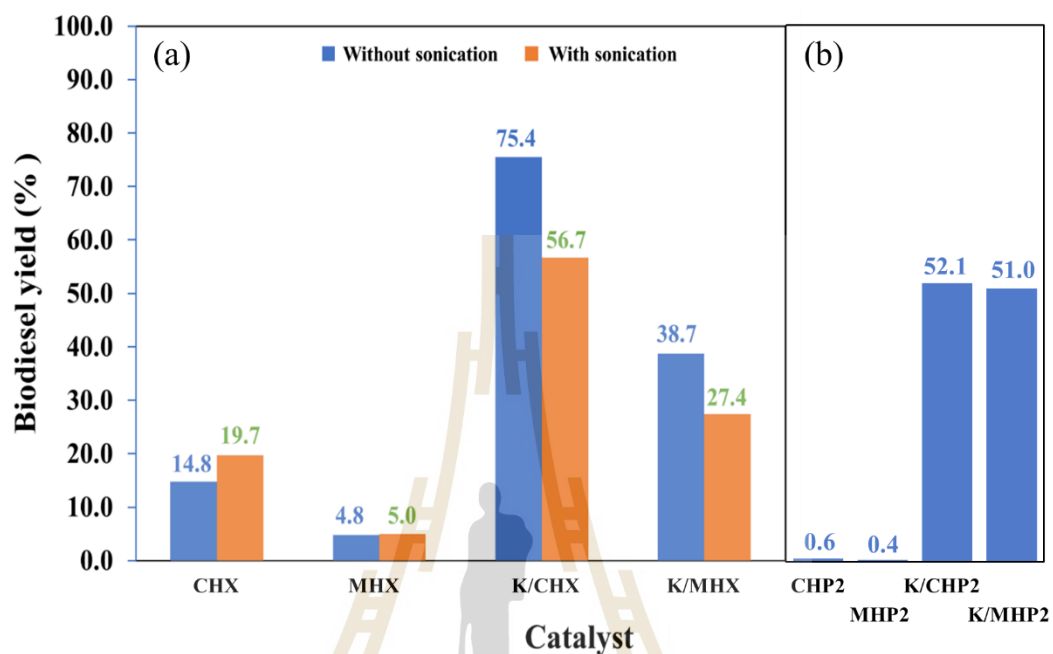


Figure 4.7 Biodiesel yields from catalysts based (a) NaX and (b) NaP2 operating at 60 °C for 3 h.

To confirm the effect of porosity and collapsed structure of zeolite NaX on the catalytic performance, the percent yield of NaP2 catalysts with small pore size is revealed in Figure 4.7b. CHP2 and MHP2 provided very low yields of biodiesel products because of their low external surface area, and the precursors could not pass through the zeolite cavity. K/CHP2 and K/MHP2 also gave similar yields, consistent with the similar FTIR intensity of free carbonate species in both samples. Moreover, their yields were close to yield from K/CHX-U, but lower than reaction over K/CHX. These results indicated that the collapse of the NaX structure due to sonication could inhibit the catalytic performance, and the porosity of NaX improved the catalytic activity.

As revealed in Table 4.5, the use of NaX-CH as catalyst support and lower potassium loading (6 wt.%) of K/CH in this work gives a higher biodiesel yield compared with 12 wt.% of potassium K/NaY and K/NaY-U [5]. The prepared catalysts

in this work could be further applied in the transesterification reaction of jatropha seed oil. NaX was the catalyst support reported in the literature (Manadee et al., 2017).

**Table 4.5** Comparison of catalytic performance and conditions of the current work with the literature.

Catalyst	Precursor	Oil type	Temperature (°C)/ time (h)	Biodiesel yield (%)	Reference
8K/NaX	CH <sub>3</sub> COOK/CH <sub>3</sub> COOH	Jatropha seed oil	60 / 3	73	(Manadee et al., 2017)
12K/NaX	CH <sub>3</sub> COOK/CH <sub>3</sub> COOH	Jatropha seed oil	60 / 3	83	(Manadee et al., 2017)
6K/CH	CH <sub>3</sub> COOK	Palm oil	60 / 3	75.4	This work
6K/CH-U	CH <sub>3</sub> COOK	Palm oil	60 / 3	56.7	This work
6K/MH	CH <sub>3</sub> COOK	Palm oil	60 / 3	38.7	This work
6K/MH-U	CH <sub>3</sub> COOK	Palm oil	60 / 3	27.4	This work
12K/NaY	CH <sub>3</sub> COOK/CH <sub>3</sub> COOH	Palm oil	60 / 3	68.6	(Rakmae et al., 2016)
12K/NaY-U	CH <sub>3</sub> COOK/CH <sub>3</sub> COOH	Palm oil	60 / 3	72.4	(Rakmae et al., 2016)

#### 4.5 Conclusions

This chapter exhibits the effect of ultrasonication in catalyst preparation, a heating source in zeolite synthesis, and the type of zeolite on catalyst properties and catalytic performance in the transesterification reaction of palm oil. Firstly, ultrasonication does not affect the morphology change and the collapse of any bare NaX supports. However, in the presence of potassium species, the sonication accelerates corrosion. It enhances the hydrolysis of both NaX-CH and NaX-MH supports, which causes the low surface area and pore volume of micropores. Additionally, NaX from different heating methods results in different coordination of potassium carbonate on the support surfaces, including bidentate potassium

carbonate on NaX-CH and mono- and bidentate potassium carbonate on NaX-MH, which affects the basicity of the obtained catalysts. In addition, larger remaining surface areas of the potassium catalysts from NaX-MH compared with those on NaX-CH result from higher stability of NaX-MH.

In catalytic performance, K/CHX gives the highest biodiesel yield which is consistent with the highest amount of total basicity and containing free carbonate species. The yields of the potassium catalysts with sonication are lower than those without sonication, which supports the conclusion that the sonication enhances the structural collapse of NaX. Moreover, potassium catalysts on NaP2 from CH and MH provide similar properties and catalytic performances to those on NaX with collapse structure and lower than K/CHX. Although the catalytic performances of the catalysts on NaX-MH are worse, their structures are more stable than those of the catalysts on NaX-CH.

#### 4.6 References

- Busca, G., and Lorenzelli, V. (1982). Infrared spectroscopic identification of species arising from reactive adsorption of carbon oxides on metal oxide surfaces. *Materials Chemistry*, 7, 89–126.
- Chandrasekhar, S., and Pramada, P. N. (2004). Kaolin-based zeolite Y, a precursor for cordierite ceramics. *Applied Clay Science*, 27(3), 187–198.
- Coenen, K., Gallucci, F., Mezari, B., Hensen, E., and Annaland, M. V. S. (2018). An in-situ IR study on the adsorption of CO<sub>2</sub> and H<sub>2</sub>O on hydrotalcites. *Journal of CO<sub>2</sub> Utilization*, 24(November 2017), 228–239.
- Flanigen, E. M., Khatami, H., and Szymanski, H. A. (1974). Infrared structural studies of zeolite frameworks. In *Molecular Sieve Zeolites-I* (Vol. 101, pp. 16–201). American Chemical Society.
- Jantarit, N., Tayraukham, P., Osakoo, N., Föttinger, K., and Wittayakun, J. (2020). Formation of EMT / FAU intergrowth and nanosized SOD zeolites from synthesis gel of zeolite NaX containing ethanol formation of EMT / FAU intergrowth and nanosized SOD zeolites from synthesis gel of zeolite NaX containing ethanol. *Materials Research Express*, 7, 1–9.

- Kwakye-Awuah, B., Von-Kiti, E., Nkrumah, I., Erdoo Ikyreve, R., Radecka, I., and Williams, C. (2016). Parametric, equilibrium, and kinetic study of the removal of salt ions from Ghanaian seawater by adsorption onto zeolite X. *Desalination and Water Treatment*, 57(45), 21654–21663.
- Lam, M. K., and Lee, K. T. (2012). Microalgae biofuels: a critical review of issues, problems and the way forward. *Biotechnology Advances*, 30(3), 673–690.
- Le, T., Wang, Q., Pan, B., Ravindra, A. V., Ju, S., and Peng, J. (2019). Process regulation of microwave intensified synthesis of Y-type zeolite. *Microporous and Mesoporous Materials*, 284, 476–485.
- Linares, C. F., Valenzuela, E., Ocanto, F., Pérez, V., Valbuena, O., and Goldwasser, M. R. (2008). K<sup>+</sup> and Ca<sup>2+</sup> modified Na-X zeolites as possible bile acids sequestrant. *Journal of Materials Science: Materials in Medicine*, 19(5), 2023–2028.
- Manadee, S., Sophiphun, O., Osakoo, N., Supamathanon, N., Kidkhunthod, P., Chanlek, N., Wittayakun, J., and Prayoonpokarach, S. (2017). Identification of potassium phase in catalysts supported on zeolite NaX and performance in transesterification of Jatropha seed oil. *Fuel Processing Technology*, 156, 62–67.
- Montalbo, K. D., De Leon, R. L., Sophiphun, O., Manadee, S., Prayoonpokarach, S., and Wittayakun, J. (2013). Characterization and catalytic performance of potassium loaded on rice husk silica and zeolite NaY for transesterification of jatropha seed oil. *Quimica Nova*, 36(8), 1116–1120.
- Mozgawa, W., Król, M., and Barczyk, K. (2011). FT-IR studies of zeolites from different structural groups. *Chemik*, 65(7), 671–674.
- Oleksiak, M. D., Ghorbanpour, A., Conato, M. T., McGrail, B. P., Grabow, L. C., Motkuri, R. K., and Rimer, J. D. (2016). Synthesis strategies for ultrastable zeolite GIS polymorphs as sorbents for selective separations. *Chemistry – A European Journal*, 22(45), 16078–16088.
- Peña, R., Romero, R., Martínez, S. L., Natividad, R., and Ramírez, A. (2013). Characterization of KNO<sub>3</sub>/NaX catalyst for sunflower oil transesterification. *Fuel*, 110, 63–69.
- Prescott, H. A., Li, Z., Kemnitz, E., Trunschke, A., and Deutsch, J. (2005). *Application of calcined Mg – Al hydrotalcites for Michael additions : an investigation of*

*catalytic activity and acid – base properties. 234, 119–130.*

- Rakmae, S., Keawkumay, C., Osakoo, N., Montalbo, K. D., de Leon, R. L., Kidkhunthod, P., Chanlek, N., Roessner, F., Prayoonpokarach, S., and Wittayakun, J. (2016). Realization of active species in potassium catalysts on zeolite NaY prepared by ultrasound-assisted impregnation with acetate buffer and improved performance in transesterification of palm oil. *Fuel, 184*, 512–517.
- Sharma, P., Yeo, J., Han, M. H., and Cho, C. H. (2013). Knobby surfaced, mesoporous, single-phase GIS-NaP1 zeolite microsphere synthesis and characterization for H<sub>2</sub> gas adsorption. *Journal of Materials Chemistry A, 1*, 2602–2612.
- Supamathanon, N., Wittayakun, J., and Prayoonpokarach, S. (2011). Properties of Jatropha seed oil from Northeastern Thailand and its transesterification catalyzed by potassium supported on NaY zeolite. *Journal of Industrial and Engineering Chemistry, 17*(2), 182–185.
- Vafaeian, Y., Haghghi, M., and Aghamohammadi, S. (2013). Ultrasound assisted dispersion of different amount of Ni over ZSM-5 used as nanostructured catalyst for hydrogen production via CO<sub>2</sub> reforming of methane. *Energy Conversion and Management, 76*, 1093–1103.
- Xie, W., Huang, X., and Li, H. (2007). Soybean oil methyl esters preparation using NaX zeolites loaded with KOH as a heterogeneous catalyst. *Bioresource Technology, 98*(4), 936–939.
- You, R., Zhang, Y., Liu, D., Meng, M., Jiang, Z., Zhang, S., and Huang, Y. (2015). A series of ceria supported lean-burn NO<sub>x</sub> trap catalysts LaCoO<sub>3</sub>/K<sub>2</sub>CO<sub>3</sub>/CeO<sub>2</sub> using perovskite as active component. *Chemical Engineering Journal, 260*, 357–367.
- Zhou, Y., Chen, W., Wang, P., and Zhang, Y. (2018). EMT-type zeolite for deep purification of trace polar-oxygenated compounds from light olefins. *Microporous and Mesoporous Materials, 271*(April), 273–283.

## CHAPTER V

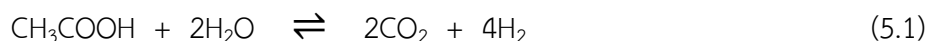
### HYDROGEN PRODUCTION VIA ACETIC ACID STEAM REFORMING OVER NICKEL SUPPORTED ON MFI CATALYST

#### 5.1 Abstract

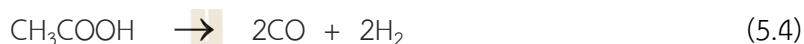
This investigation explored the acetic acid steam reforming (AASR) process over Ni/MFI catalysts prepared via the impregnation method. The catalytic performance was systematically analyzed with respect to key parameters, namely the Si/Al ratio in the MFI support, steam-to-carbon ratio, reaction time, and nickel loading. Extensive characterization techniques were employed to gain insights into the structural and chemical properties of the catalysts. The results underscored the substantial impact of the Si/Al ratio on the catalytic activity, selectivity, and carbon deposition of Ni/MFI catalysts. Higher Si/Al ratios notably enhanced acetic acid conversion and hydrogen yield at longer reaction time. Furthermore, elevating the steam-to-carbon ratio exhibited improved catalytic performance by promoting the water gas shift reaction and mitigating coke formation. Adjusting the nickel loading allowed for fine-tuning of the catalytic activity, with optimal performance achieved at specific nickel loadings. These findings provide valuable guidance for the design and optimization of Ni/MFI catalysts in AASR, emphasizing the crucial role of controlling the Si/Al ratio, steam-to-carbon ratio, reaction time, and nickel loading to attain decreasing of coke formation and superior catalytic performance.

#### 5.2 Introduction

Acetic acid steam reforming (AASR) is a catalytic process that holds significant promise to produce hydrogen gas from renewable sources and organic waste streams. Acetic acid, a major component of bio-oil and various industrial waste streams, is converted into hydrogen gas and valuable byproducts (Isahak et al., 2012). The AASR reaction with molar balancing can be represented by equation 5.1 (Guo et al., 2012).



The relatively stable acetic acid has the potential to undergo transformations leading to various intermediates and products. AASR is a combination of steam reforming (Eq. 5.1), water gas shift reaction (WGS, Eq. 5.2), and thermal decomposition reaction (Eq. 5.3-5.4) (Chen et al., 2017).



The operating conditions such as steam-to-carbon (S/C) ratio reaction time and temperature are likely to significantly impact these interactions, ultimately leading to the emergence of an intricate network of reactions (Chen et al., 2017). Additionally, in the presence of catalyst support with sufficient acidic sites, such as  $\text{Al}_2\text{O}_3$ , a ketonization reaction (Eq. 5.5) occurs.



This side reaction leads to the formation of acetone as an intermediate, which serves as a precursor for coke production (Li et al., 2012). Hence, it is crucial to explore the reaction conditions and the composition of catalysts, encompassing both the choice of metal and support materials, to investigate their significance in enhancing both catalyst activity and mitigating coke formation.

Nickel (Ni) catalysts are commonly used in steam reforming industries because of their affordable price compared with noble metals. It promotes the cracking of C–C and C–H bond, the oxidation resistance, which improves catalyst stability (Hu and Lu, 2010). In addition, the suitable Ni weight also reduces coke formation and aggregation of Ni particles (Z. Zhang et al., 2018).

Moreover, support is an important composition affecting carbon deposits for spent catalysts. Recent publications report the preparation of Ni on  $\text{Al}_2\text{O}_3$  prepared by impregnation (Ibrahim et al., 2021; Reeve et al., 2022; Z. Zhang et al., 2018). However, the performance of the catalysts is limited by the low surface area of the support. To solve the weakness, Ni supported on aluminosilicate porous like ZSM-5 zeolite which has MFI (Mobil-type five) structure is prepared. The Ni/ZSM-5 catalyst provides high stability and low carbon deposition due to its porous structure, larger surface area, and

high stability of ZSM-5 zeolite compared with Ni/Al<sub>2</sub>O<sub>3</sub> (Fakeeha et al., 2013). Although the presence of Al content enhances the strong interaction between Ni species and alumina, it facilitates the formation of byproducts such as CH<sub>4</sub>, CO, and coke (Hu et al., 2012).

Therefore, Ni supported on silicalite-1, also known as siliceous ZSM-5 zeolite in the MFI family, (Ni/S-1), is investigated to reduce coke formation in AASR. Because there are no reports of Ni on the support with different silicon-to-aluminum (Si/Al) ratios in AASR, it is studied in this work. Moreover, Ni loading by the impregnation method, reaction conditions including S/C ratio, and reaction time are investigated to optimize AASR condition.

### 5.3 Material synthesis

#### 5.3.1 Chemicals

The chemicals for catalysts synthesis are tetraethyl orthosilicate (TEOS, special grade), tetrapropylammonium hydroxide solution (TPAOH, 10%, structure directing agent), nitric acid (HNO<sub>3</sub>, 35%), sodium chloride (NaCl, 99.0%), aluminum nitrate nonahydrate (Al(NO<sub>3</sub>)<sub>3</sub>·9H<sub>2</sub>O, 98.0 wt.%), ethanol (CH<sub>3</sub>CH<sub>2</sub>OH, 99.5%), nickel (II) nitrate hexahydrate (Ni(NO<sub>3</sub>)<sub>2</sub>·6H<sub>2</sub>O, 1 and 0.1 M), ammonia solution (NH<sub>3</sub>, 28 wt.%), and acetic acid (CH<sub>3</sub>COOH, 99.9%). All chemicals were produced by FUJIFILM Wako company.

#### 5.3.2 Synthesis of MFI zeolites with different Si/Al ratio

The TPAOH solution, distilled water, Al(NO<sub>3</sub>)<sub>3</sub>·9H<sub>2</sub>O, and NaCl were mixed in a 300-mL Teflon beaker. Then, TEOS, which is the Si source, was poured into the mixture and kept stirring for 24 h. The compositions of H<sub>2</sub>O/Si, Na/Al, Si/TPAOH are 50, 3, and 3 mol/mol, respectively. In a condition without Al, Al(NO<sub>3</sub>)<sub>3</sub>·9H<sub>2</sub>O, and NaCl were not added. The Si/Al mol ratios varied as ∞ (no Al added), 100, and 50. The solution was heated for hydrothermal synthesis (HTS) at 180 °C for 72 h in a 200-mL Teflon-line autoclave reactor and a tumbling oven (ADVANTEC, DRM6200B). Afterward, the pH was adjusted to 8.5 by adding HNO<sub>3</sub> dropwise with pH monitoring to further precipitate the zeolite. Then, the solid was separated by centrifugation, washed with distilled water 3 times, dried at 110 °C overnight, and calcined at 550 °C for 12 h in an

atmospheric condition to remove the structure directing agent. The obtained powder was named S-1, Z100, and Z50, respectively.

### 5.3.3 Ni/MFI zeolite catalysts preparation

The Ni catalysts supported on MFI (Ni/MFI) were prepared by incipient wetness impregnation method adapted from Zhang et al. (2023). The nickel solution, 0.1 M  $\text{Ni}(\text{NO}_3)_2$  in ethanol, was added dropwise on dried zeolite supports (S-1, Z100, Z50) to obtain 5 wt.% of Ni. Then, the wet powder was dried at room temperature in a fume hood for 3 h, and hot air oven at 110 °C overnight before calcination at 550 °C for 12 h. The samples were named xNi/y where x is different wt.% of Ni and y is MFI zeolite with different Al content.

### 5.3.4 Material characterizations

The crystallinity of powder products was confirmed by X-ray powder diffraction (XRD) on a Rigaku X-ray diffractometer (Smart Lab) using  $\text{Cu K}\alpha$  radiation with a current of 40 mA, a potential of 40 kV, a step of 0.01°, and a speed of 50  $\text{min}^{-1}$ . All of the samples were analyzed on the same day to compare crystallinity with a more confident result. Moreover, the percent crystallinity and crystal size of each sample was calculated by equation 5.6 and Scherrer equation (Yao et al., 2018).

$$\text{Crystallinity (\%)} = \frac{\text{Area of crystalline peaks}}{\text{Total peak area}} \times 100 \quad (5.6)$$

The Si/Al mole ratio and percent weight of Ni (from Ni and supports) was analyzed by X-ray fluorescence (XRF) on X-Ray Fluorescence Spectrometer (Rigaku, Supermini) with Pd X-ray source about 50 kV, 4 mA. The particle size and morphology were observed by scanning electron microscopy (SEM) on a HITACHI, S-5200 scanning electron microscope. The functional group of catalyst supports with different Si/Al ratios were determined by Fourier-transform infrared spectroscopy (FTIR) on a Bruker, Tensor 27 using attenuated total reflectance (ATR) mode with a resolution of 4  $\text{cm}^{-1}$ . All catalysts were dried at 100 °C before being immediately measured to reduce interference from water. The Ni particle size was revealed by Transmission electron microscopy (TEM) on a HITACHI, H-7650 at 120 kV. The samples were dispersed in propanol on a copper grid and vacuumed before measuring. The surface

area and porosity properties were investigated by Nitrogen adsorption-desorption on a MICROTRAC MRB, BELSORP Mini X. 30 mg of each sample was pretreated at 300 °C, 18 h in vacuum before analysis. The suitable temperature for catalyst reduction was determined by Temperature-programmed reduction by hydrogen ( $H_2$ -TPR) connected with a mass spectrometer (MS) detector. The sample was measured under the same condition as reaction testing.

#### 5.4 Catalytic testing via Acetic acid steam reforming reaction (AASR)

Figure 5.1 shows the AASR setup, which consists of 13 parts. In each catalytic testing, 0.1 g of catalyst was packed in a quartz tube (inner diameter and length were 4 mm and 1.5 cm) between quartz wool. Then, the tube was inserted into the fixed-bed flow reactor (part 8 in Figure 5.1). The catalyst was oxidized at 850 °C under air, reduced under 50 %v/v  $H_2/N_2$  at the same temperature to generate the catalytic active form and cooled down to 700 °C. The temperature programs are shown in Figure 5.2. Then, the acetic acid solution was injected and flowed through the catalyst by  $N_2$  carrier gas at 700 °C.



**Figure 5.1** AASR setup: (1) Feed injector: flow acetic acid solution into the flow reactor, (2) Gas tank, (3) Gas valve: open and close gas from tank, (4) Flow meter: setting gas flow rate, (5) Gas line<sub>(in)</sub>: flowing  $N_2$  as carrier gas into flow reactor, (6) Heater: heating

all of gas line to 120 °C, (7) Heater: heating of flow reactor, (8) Flow reactor: the quartz tube containing catalyst inside the reactor, (9) GC-FID: analysis of hydrocarbon chemicals, (10) Gas line<sub>(out)</sub>: flowing mixed gas from reactor to analysis part, (11) GC-TCD: analysis of small gas molecules, (12) Start button: button for starting the analysis and data collecting, (13) Computer: processing system.

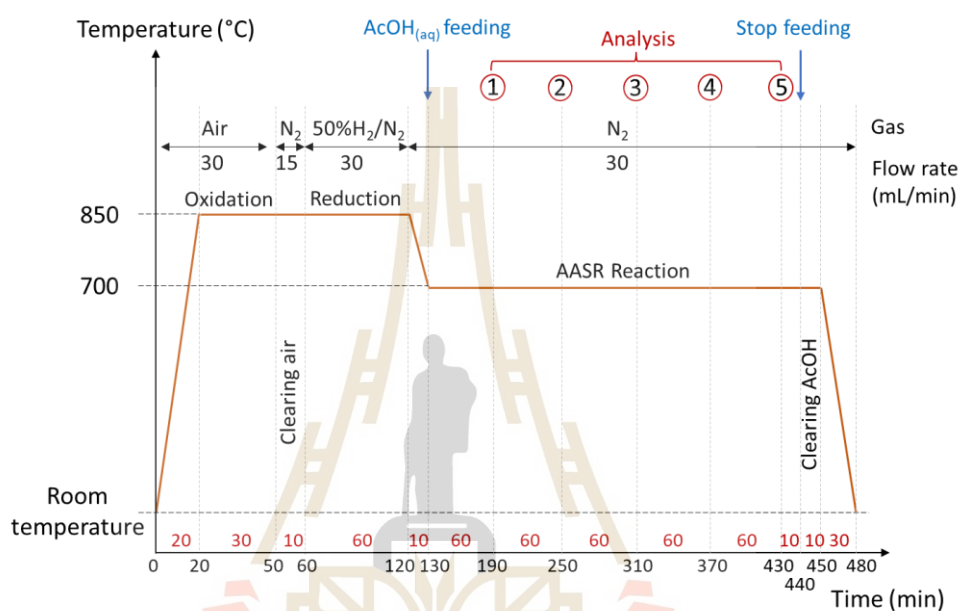


Figure 5.2 Catalytic processing and temperature program of AASR.

The impact of the steam-to-carbon (S/C) ratio of acetic acid solution and reaction time were investigated under constant molar flow rates of acetic acid (0.006 mol/h), catalyst weight-to-acetic acid flow rate ratio (W/F, 0.283) and the molar fraction of acetic acid to water and nitrogen carrier gas (0.043). Notably, the nitrogen gas flow rate varied between 30 and 40 mL/h, corresponding to different S/C ratios of 5 and 3, respectively. In simpler terms, the gas hourly space velocity (GHSV), calculated at standard temperature and pressure (STP), was modified to 19,084 and 13,987 h<sup>-1</sup> when the S/C ratio changed to 5 and 3, respectively. The calculations were performed according to equations 5.7 - 5.10.

$$\text{S/C ratio} = \frac{\text{Moles of water in feedstock}}{\text{Moles of carbon in feedstock}} \quad (5.7)$$

$$\text{W/F ratio} = \frac{\text{Catalyst weight (g)}}{\text{Acetic acid flow rate (g/h)}} \quad (5.8)$$

$$\text{Mole fraction of acetic acid} = \frac{\text{Volume of acetic acid at STP (mL/h)}}{\sum \text{Volume of initial gases in system (mL/h)}} \quad (5.9)$$

$$\text{GHSV (h}^{-1}\text{)} = \frac{\text{Total gaseous flow rate including inert gases at STP (mL/h)}}{\text{Volume of catalyst (cm}^3\text{)}} \quad (5.10)$$

Subsequently, the hydrocarbons ( $C_1$ - $C_2$ ) products ( $CH_4$ ,  $CH_3COOH$ ,  $(CH_3)_2CO$ ,  $C_2H_4$ ,  $C_2H_6$ ) were analyzed from 1 to 5 hours by online gas chromatography with a flame ionization detector (GC-FID) on a SHIMADZU, GC-8A with Porapak-Q column under nitrogen gas, while the small gas molecules ( $CH_4$ ,  $CO_2$ ,  $CO$ ,  $H_2$ ) were measured by GC with thermal conductivity detector (GC-TCD) with ShinCarbonST column under argon gas.

$$\% \text{ Conversion of AcOH} = \left(1 - \frac{F_{\text{AcOH, out}}}{F_{\text{AcOH, in}}}\right) \times 100 \quad (5.11)$$

$$\% \text{ Yield of H}_2 \text{ (single-H)} = \frac{2 F_{\text{H}_2, \text{out}}}{4 F_{\text{AcOH, in}} \times (1 + \text{S/C ratio})} \times 100 \quad (5.12)$$

$$\% \text{ Yield of CO}_2, \text{ CO, CH}_4 \text{ (single-C)} = \frac{F_{\text{CO}_2, \text{CO, CH}_4, \text{out}}}{2 F_{\text{AcOH, in}}} \times 100 \quad (5.13)$$

Percent conversions of  $CH_3COOH$  and % yield of  $H_2$ ,  $CO_2$ ,  $CO$ ,  $C_2$  products were calculated using equations 5.11 - 5.13 where  $F_{i, \text{in}}$  and  $F_{i, \text{out}}$  ( $i = CH_3COOH, H_2O, CO_2, H_2, CO$ , and  $C_2$  gases products) are the inlet and outlet molar flow rates of component  $i$  in term of mol/h. The peak area was compared with the standard calibration curve. Moreover, the quantity of product at thermal equilibrium was estimated by the NASA Computer program CEA (Chemical Equilibrium with Applications). The type and molar ratio of initial chemicals, type of final product, reaction temperature and pressure are required to complete the calculation. The details of the calculation are explained in Appendix A.

The weight of carbon deposition of spent catalyst (15 mg) was determined by Thermogravimetric Analysis (TGA) on a Rigaku, Thermo plus evo from 250 -900 °C (10 °C/min) under airflow (80 mL/min). The samples were heated at 250 °C with a heating rate of 10 °C/min for 1 h before ramping to 900 °C with a heating rate of 10 °C/min and held for 1 h. The weight difference was assumed to be the amount of carbon deposited on the catalyst.

## 5.5 Results and Discussion

### 5.5.1 Effect of 5Ni/MFI with different Al content in zeolite

Table 5.1 reveals Si/Al ratio of zeolite supports and the percent weight of Ni in catalysts from XRF technique. The averaged quantity of Si/Al ratio and Ni were marginally higher than the initial composition. Thus, silanol groups and Ni particles were probably on the zeolite surface.

**Table 5.1** Si/Al ratio and Ni loading of Ni/MFI catalysts.

Sample name	Si/Al mole ratio <sup>a</sup>	Ni loading (wt.%) <sup>a</sup>
5Ni/Z50	62	5.32
5Ni/Z100	118	5.43
5Ni/S-1	-	5.44

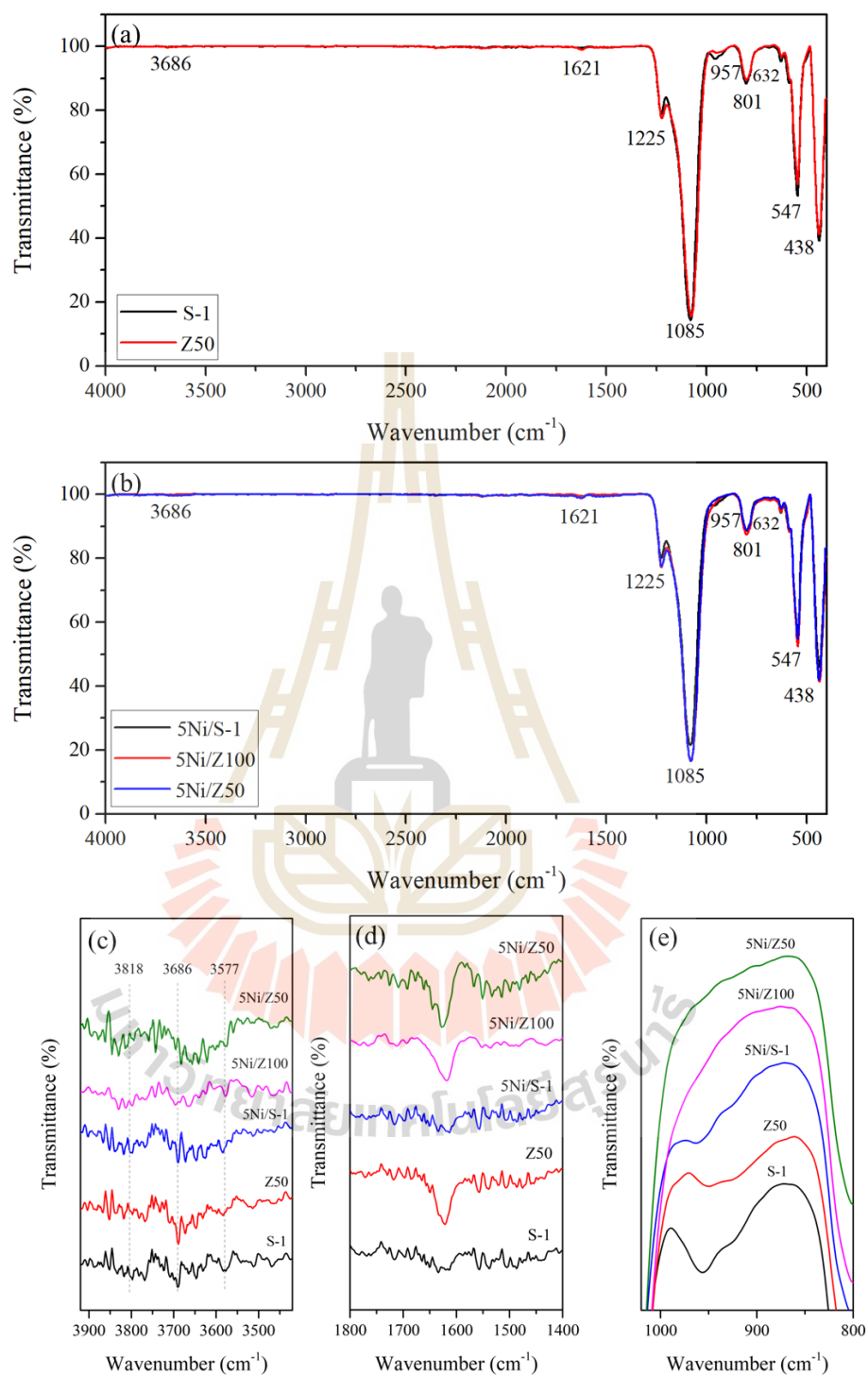
<sup>a</sup>Averaged percent weight of Ni, Al, and Si, analyzed 3 times by XRF.

Figure 5.3 displays FTIR spectra of both zeolite supports and Ni/MFI catalysts. Figure 5.3a presents the FTIR spectrum of the zeolite supports and Figure 5.3b shows the corresponding spectra of the Ni/MFI catalysts. The samples were dried to eliminate physically adsorbed water, resulting in small O-H stretching bands at higher wavenumbers. Figure 5.3c highlights vibrations at 3818 cm<sup>-1</sup> and 3686 cm<sup>-1</sup>, corresponding to the O-H stretching of external Si-OH and Brønsted acid, respectively. These vibrations exhibited a slight increase in the high Al-support samples. In contrast, the vibration of internal Si-OH networks at 3577 cm<sup>-1</sup> was observed more prominently in zeolites with higher silica content (Hong et al., 2021). A peak at 1621 cm<sup>-1</sup> was noticeable in samples with a higher aluminum content (Figure 5.3d). This O-H bending

vibration was likely associated with the hydroxyl group in silanol or chemisorbed water (Ghasemi and Younesi, 2012). Another silanol (Si-OH) bending mode, linked to silicon atoms connected to a hydroxyl group, was observed at  $957\text{ cm}^{-1}$  in Figure 5.3e. This peak was more pronounced in siliceous zeolites compared to others. Moreover, the vibration patterns confirm the structure of the zeolite, as outlined in Table 5.2. Notably, the double ring vibration of D5R at  $547\text{ cm}^{-1}$  were the characteristics of the MFI zeolite framework (dos Santos et al., 2020).

**Table 5.2** Wavenumber and vibration of functional group in catalysts from Figure 5.3.

No.	Wavenumber ( $\text{cm}^{-1}$ )	Functional vibration	Reference
1	3818	O-H stretching of external Si-OH	(Hong et al., 2021)
2	3686	O-H stretching of Brønsted acid	
3	3577	O-H stretching of internal Si-OH nets	
4	1621	O-H bending vibration	
5	1225	Asymmetric stretch of external linkage T-O-T (T = Si, Al)	(Ghasemi and Younesi, 2012)
6	1085	Asymmetric stretch of internal linkage T-O-T (T = Si, Al)	
7	957	Silanol (Si-OH) bending mode associated with the silicon atoms linked to one hydroxyl group	
8	801	External symmetrical stretching bands of T-O-T	(dos Santos et al., 2020)
9	632	Symmetric stretching vibration of internal linkage $\text{TO}_4$	
10	547	Double ring vibration of D5R in MFI zeolite framework	(Ghasemi and Younesi, 2012)
11	438	T-O bending vibration of the $\text{SiO}_4$ and $\text{AlO}_4$ internal tetrahedral	



**Figure 5.3** Fourier transform infrared (FTIR) spectra at wide range of (a) S-1, Z50 zeolite supports, and (b) 5Ni/S-1, 5Ni/Z100, 5Ni/Z50 catalysts, and (c-e) narrow range.

The structure of MFI zeolite was confirmed by powder XRD patterns. Figure 5.4a reveals the crystal structure of MFI zeolite (Ojeda et al., 2018). The intensity slightly decreased as the Si/Al ratio of the support increased. Moreover, the phase of NiO was observed in the patterns, as shown in Figure 5.4b. The peaks at 37°, 43°, 63°, 75°, and 79° corresponded to NiO, indicating some aggregation of NiO particles and Ni particles after reduction (Fujitsuka et al., 2021; Qiao et al., 2009). The main peak at 43° of NiO was used to imply the trend of nickel crystal size in oxide form, as shown in Table 5.3. The crystal sizes of nickel in 5Ni/S-1 and 5Ni/Z50 were similar and smaller than that in 5Ni/Z100.

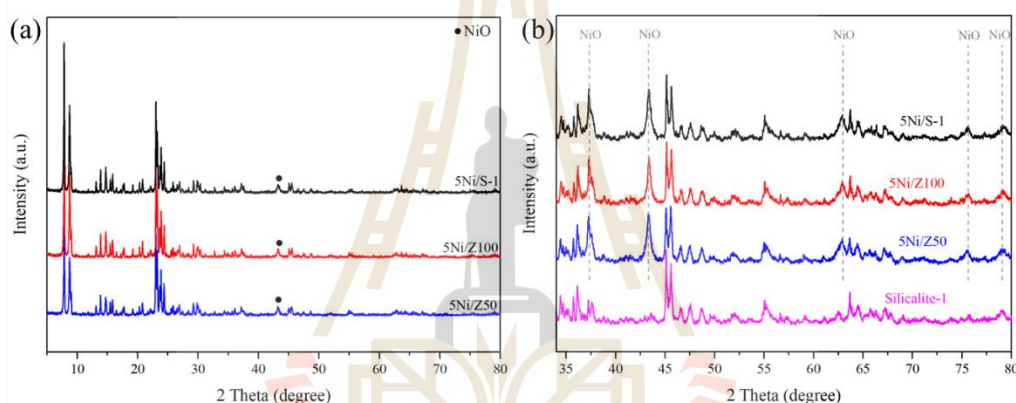


**Figure 5.4** Powder X-Ray diffraction (XRD) patterns of silicalite-1 zeolite and 5Ni/S-1, 5Ni/Z100, 5Ni/Z50 catalysts with different 2 theta: (a) 5-80, and (b) 35-80 degree.

**Table 5.3** Crystalline size, diameter, and spherical volume of Ni nanoparticles in Ni/MFI catalysts.

Sample name	Ni crystalline size (nm) <sup>a</sup>	Ni particle diameter, $d_{\text{TEM}}$ (nm) <sup>b</sup>	Ni particle volume, $V_{\text{TEM}}$ (nm <sup>3</sup> ) <sup>b</sup>
5Ni/Z50	17.5	15.0	$7.3 \times 10^3$
5Ni/Z100	19.9	15.6	$14.2 \times 10^3$
5Ni/S-1	17.9	11.7	$6.1 \times 10^3$

<sup>a</sup>Ni crystalline size calculated by Scherrer equation from the XRD peak at 43 degree in Figure 5.4 (b), <sup>b</sup>Averaged Ni particle diameter and volume from 100 particles in TEM images.

TEM images in Figure 5.5 reveals the feature of Ni<sup>0</sup> particles which are black spots and disperse differently on each zeolite support. There were two particle size distributions of Ni<sup>0</sup> in the coffin-like shape of MFI zeolite (Fujitsuka et al., 2021) of 5Ni/Z50, including big size on the edge and middle size on the surface of zeolite as shown in Figure 5.5a and 5.5d. The particle distribution, measuring from 100 particles, indicated the main population in a diameter range of 5-10 nm; the largest was 70 nm. In the case of 5Ni/Z100, there were three sizes of particles, as shown in Figure 5.5b and 5.5e. The small one in the range below 5 nm appeared. Even though the amount of Ni<sup>0</sup> was smaller than the previous one, it had a broader distribution of Ni<sup>0</sup>. Excitingly, Ni<sup>0</sup> particles of 5Ni/S-1 in Figure 5.5c and 5.5f had small sizes (< 5nm) with a high population. Although some particle aggregation was obtained, it showed narrow particle size distribution in a smaller range than others.

Moreover, the diameter and volume of spherical Ni<sup>0</sup> particles from TEM images reveal the same trend as crystal size, as shown in Table 5.3. The averaged particle size was smaller when Al was not observed in support. Similarly, Bacariza et al. (2020) reported the influence of solvents and polarities on the size distribution of Ni<sup>0</sup> particles in an Al-rich zeolite prepared through the impregnation method. When organic solvents like ethanol were used instead of water, there was an increase in weak and medium basic sites. The result implies that matching the same polarity of the solvent to that of the zeolite enhances metal dispersion and reduces the size of metal particles. Therefore, the compatibility between the solvent and zeolite polarity became a crucial factor affecting the distribution of the metal. In this work, nickel precursor was dissolved in ethanol for the ZSM-5 support with a high Al content (5Ni/Z50) to prevent the dispersion of Ni metal.

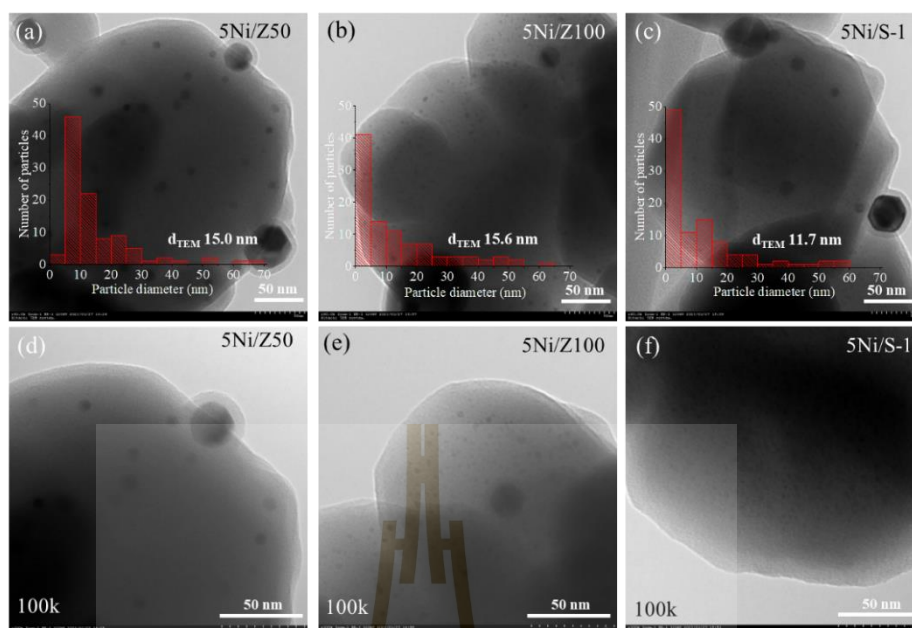


**Figure 5.5** Transmission electron microscopy (TEM) images of 5Ni/MFI catalysts with different Si/Al in support: (a-d) 5Ni/S-1, (b, e) 5Ni/Z100, (c, f) 5Ni/Z50.

Conversely, metal-support interactions were promoted when silicalite-1 was used (Xu et al., 2022). However, the behavior of nickel dispersion low aluminum support (5Ni/Z100) could be explained by referring to Figure 5.6. In this case, the  $\text{Ni}^{2+}$  ions, which carry a positive charge, prefer negatively charged oxygen atoms near the Al positions within the zeolite framework. When the number of  $\text{Ni}^{2+}$  ions and hydrophilic position of zeolite were not balanced,  $\text{Ni}^{2+}$  could induce hydrophilicity on the surface of zeolite and aggregated after calcination, resulting in the formation of larger  $\text{Ni}^0$  particles (Wei et al., 2021).

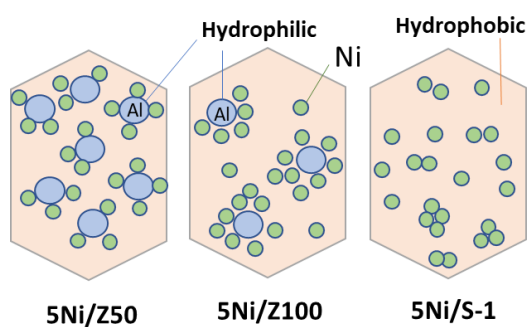


**Figure 5.6** The model for the hypothetical distribution of nickel in different polarity zeolites, including 5Ni/Z50, 5Ni/Z100, and 5Ni/S-1.

Nitrogen adsorption-desorption of bare zeolite supports and catalysts are shown in Figure 5.7a. The isotherms were type I without hysteresis loop (Figure 5.7b), the characteristic of microporous materials. The moderately large surface area ( $S_{\text{BET}}$ ), external surface area ( $S_{\text{ext}}$ ), and micropore volume ( $V_{\text{micro}}$ ) are summarized in Table 5.4. The  $S_{\text{BET}}$  and  $V_{\text{micro}}$  showed increasing trends in  $Z50 < Z100 < S-1$ , but a decreasing trend in  $5\text{Ni}/Z50 > 5\text{Ni}/Z100 > 5\text{Ni}/S-1$ . The difference in  $S_{\text{BET}}$  and  $V_{\text{micro}}$  between the zeolite and catalyst increases, while  $S_{\text{ext}}$  decreases as the Al content in the support reduces. Therefore, it is evident that a portion of the nickel particles diffused into the microporous structure which is particularly in the case of 5Ni/S-1 and it also dispersed on the external framework of the zeolite support, respectively (Mazaheri and Kalbasi, 2015).

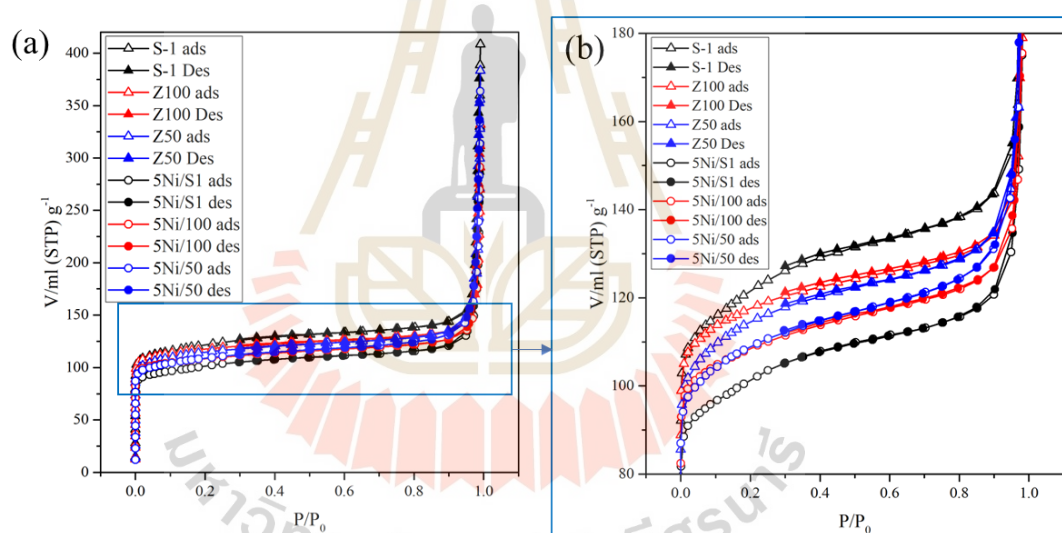


**Figure 5.7** Nitrogen adsorption (ads)-desorption (des) (a) isotherm and (b) hysteresis loop of 5Ni/S-1, 5Ni/Z100, 5Ni/Z50 catalysts.

**Table 5.4** Surface area and micropore volume of Ni/MFI catalysts.

Sample name	$S_{\text{BET}}$ (m <sup>2</sup> /g) <sup>a</sup>	Differential $S_{\text{BET}}$ (m <sup>2</sup> /g)	$S_{\text{ext}}$ (m <sup>2</sup> /g) <sup>b</sup>	Differential $S_{\text{ext}}$ (m <sup>2</sup> /g)	$V_{\text{micro}}$ (cm <sup>3</sup> /g) <sup>c</sup>	Differential $V_{\text{micro}}$ (cm <sup>3</sup> /g)
Z50	436		37		0.17	
5Ni/Z50	420	16	40	13	0.16	0.01
Z100	443		24		0.18	
5Ni/Z100	424	19	29	5	0.16	0.02
S-1	463		25		0.19	
5Ni/S-1	388	75	23	-2	0.16	0.03

<sup>a</sup> $S_{\text{BET}}$ : specific surface area calculated by the BET method., <sup>b</sup> $S_{\text{Ext}}$ : external surface area calculated by the *t*-plot method., <sup>c</sup> $V_{\text{Micro}}$ : micropore volume calculated by the *t*-plot method.

The H<sub>2</sub>-TPR profiles of catalysts in Figure 5.8 illustrates the reduction behavior of all catalysts. The nickel(II) ions in all samples were completely converted to metallic nickel below 850 °C. So, the suitable temperature for the reduction step in pretreatment should be 850 °C. Moreover, three peaks were observed in all samples, indicating three interactions between nickel and zeolite support (Hu et al., 2012). First two peaks at 300 and 470 °C correspond to bulk nickel with the highest and medium intensity, respectively. The large Ni<sup>0</sup> size should have a stronger interaction with nickel metal and a weaker interaction with support than the middle one, resulting in peak shift to a lower temperature (Yang et al., 2018). Moreover, the peaks around 640 °C might attest to the dispersed Ni<sup>0</sup> metal which has strong interaction with zeolite support. In the case of siliceous zeolite support, the peak area at 470 and 640 °C was larger than other rich Al samples, and the highest temperature range of dispersed catalyst shifts to 850 °C. The mentioned results indicated that most Ni species had strong interaction with support and good dispersion on zeolite surfaces (Hu et al., 2012). The possibility might be from the decreased interaction between some Ni<sup>2+</sup> and negative charge on the zeolite surface.

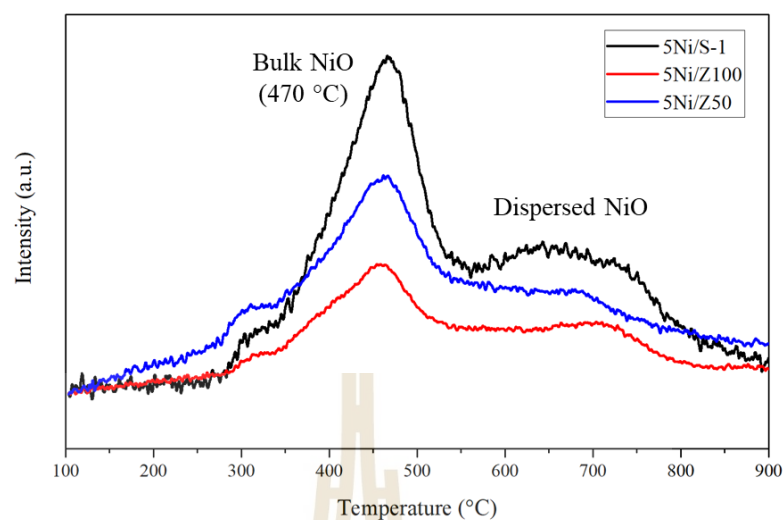


**Figure 5.8**  $H_2$ -temperature programmed reduction ( $H_2$ -TPR) profiles of 5Ni/S-1, 5Ni/Z100, 5Ni/Z50 catalysts.

The chromatogram in Figure 5.9a and 5.9b indicate the products from GC-TCD and GC-FID analysis measuring simultaneously. The small gas molecules, including hydrogen ( $H_2$ ), carbon monoxide (CO), methane ( $CH_4$ ), carbon dioxide ( $CO_2$ ) and nitrogen ( $N_2$ ) carrier gas, are observed by the TCD detector as shown in Figure 5.9a. The types of gas products were confirmed by matching with the retention time of gas standards from the same separation condition. Although methane over nickel-containing catalysts was noticed in the TCD signal, its peak area was small, corresponding to the small amount. Peak shifting to a retention time higher than 18 min becomes possible because of initiating a temperature program with a minor time inconsistency. Moreover, hydrocarbon products with one carbon atom were detected by the FID detector (Figure 5.9b). In the case of Ni catalysts, only a small peak of methane was observed at  $1.7 \text{ min}^{-1}$ , while methane ( $CH_4$ ), ethylene ( $C_2H_4$ ), acetone ( $(CH_3)_2O$ ), acetic acid ( $CH_3COOH$ ) were obtained over both zeolite supports. However, only the reaction testing over Z50 zeolite generates ethane ( $C_2H_6$ ) as a major product and other minor products with two carbon atoms ( $C_2$ ), such as acetaldehyde ( $CH_3CHO$ ) and ethanol ( $CH_3CH_2OH$ ).

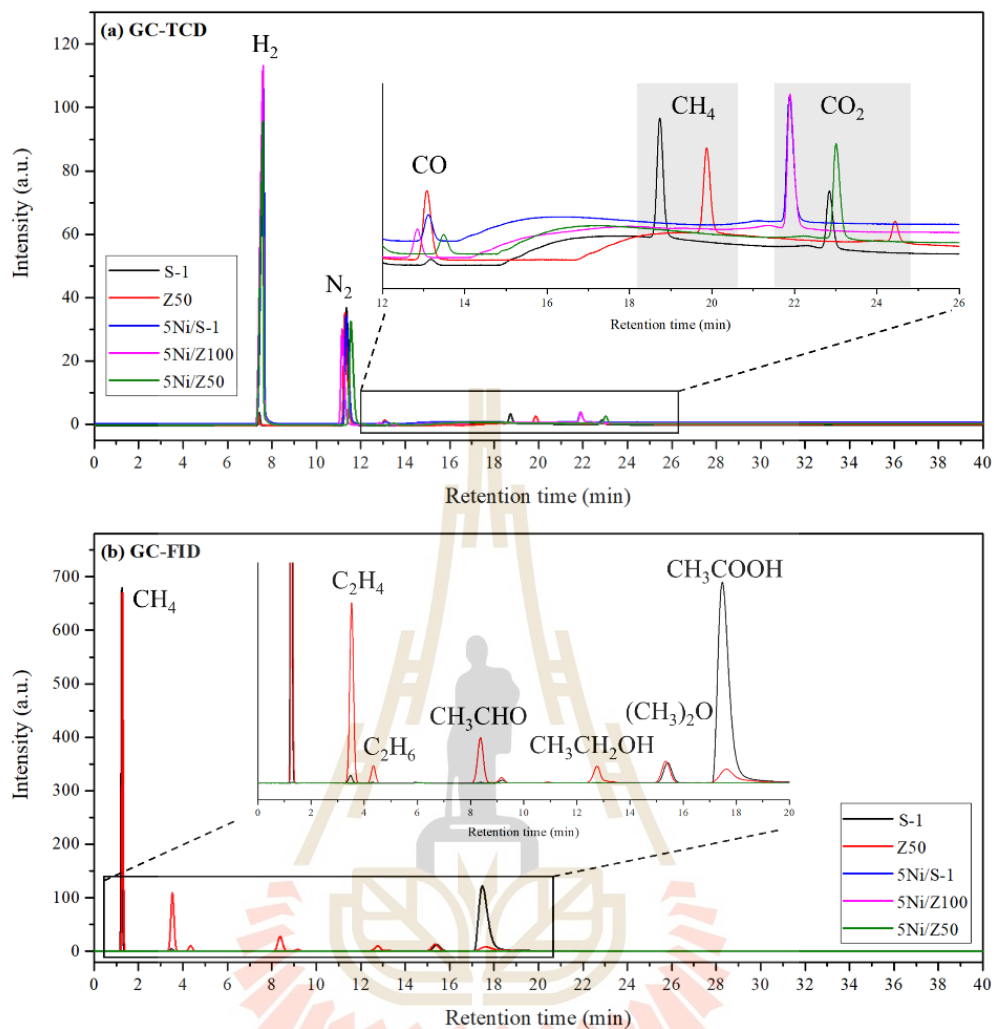


**Figure 5.9** GC chromatogram with (a) TCD and (b) FID detector over S-1, Z50, 5Ni/S-1, 5Ni/Z100, and 5Ni/Z200 catalysts with reaction condition about 700 °C, 1h, S/C ratio: 5.

The aim of this study is to investigate the impact of varying aluminum (Al) content in bare supports on the AASR reaction as a function of reaction time. Figure 5.10a presents the activity analysis of ZSM-5 zeolite with a Si/Al ratio of 50 (Z50). In the first hour, the yields and conversions of all mentioned carbon products in Figure 5.10 were calculated on a single-C atom basis, resulting in a 96% conversion of acetic acid (AcOH). The percentage yields of undesired products, which do not comply with Eq. 5.1-5.4, including C<sub>2</sub>H<sub>4</sub>, (CH<sub>3</sub>)<sub>2</sub>CO, C<sub>2</sub>H<sub>6</sub>, and other C<sub>2</sub> species (yield < 1%), are 13.1%, 5.1%, 1.4%, and 4.9%, respectively. As the reaction time increased, the conversion and

yield of all products tended to decrease, reaching a minimum of 2% AcOH conversion at 5 hours.

Conversely, silicalite-1 zeolite (S-1) provided a low conversion at 1 hour (Figure 5.10b) but showed an increasing trend at longer reaction times, reaching a peak of 72% at 5 hours. Encouragingly, there were only two byproducts, namely  $C_2H_4$  and  $(CH_3)_2CO$ , with C-yields of approximately 0.3% and 5.9%, respectively. The results suggested that the presence of Brønsted acid and  $Na^+$  counteraction in Al-ZSM-5 (Z50) enhanced the formation of methane, which served as an intermediate substance to produce hydrogen and the mentioned hydrocarbon species through different pathways (Phongprueksathat et al., 2019).

Under intermediate-rich conditions and without Ni as the active species,  $H_2$  was not produced, as shown in Figure 5.10c. The  $H_2$  yields over Z50 and S-1 were 0.4% and 0%, respectively. This observation highlighted that the generation of  $H_2$  gas depended on the presence of Ni. Consequently, the highly active surface of Al-ZSM-5 (Z50) could generate a substantial quantity of intermediates and undesired products, which could act as precursors for coke formation. The accumulation of coke in the used Z50 catalyst (Figure 5.10d) could potentially contribute to its deactivation after 1 hour of reaction time. Conversely, the relatively low amount of coke from spent S-1 catalyst correlated to the improved catalytic performance over an extended reaction period.

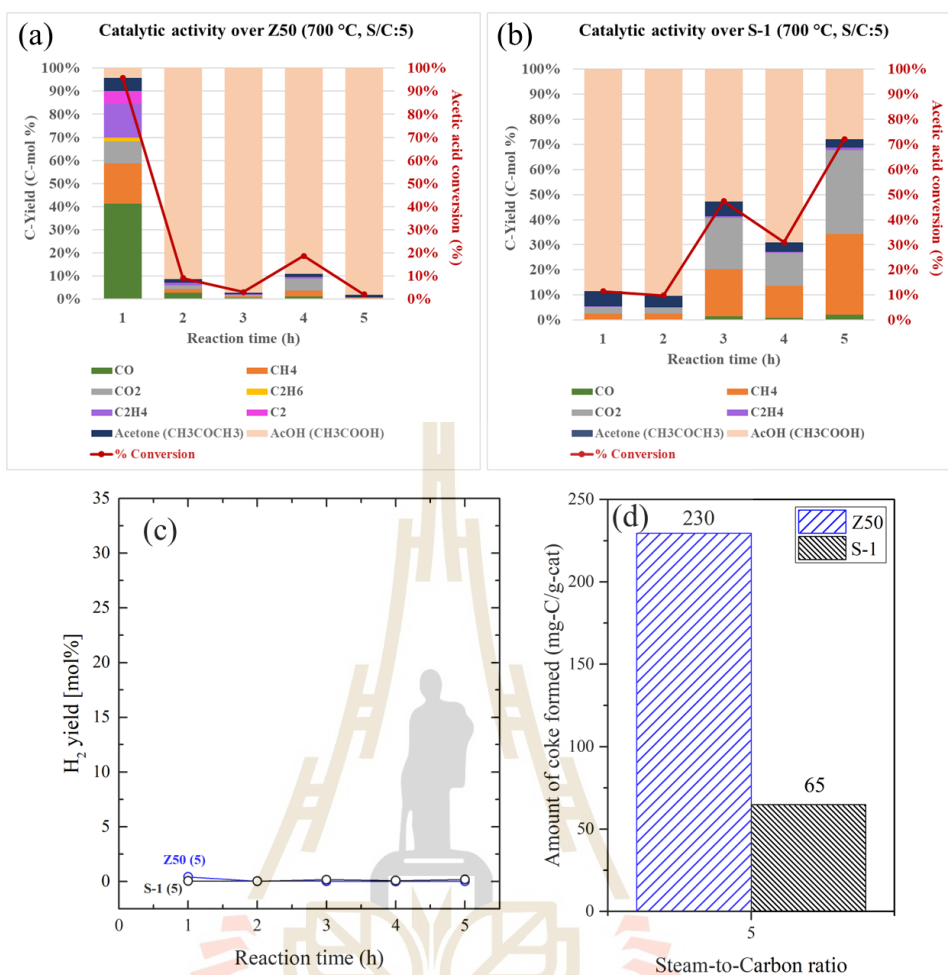


**Figure 5.10** %Acetic acid (AcOH) conversion, % C-yield over (a) S-1, (b) Z50 catalysts, and (c) % H<sub>2</sub>-yield over S-1, and Z50 with reaction condition about 700 °C, 1-5 h, S/C ratio: 5, and (d) carbon deposition on spent catalysts from TGA analysis.

The catalytic activity over Ni/MFI catalysts was a function of reaction time and S/C ratio. Figures 5.11a-b show the percent yield of CO<sub>2</sub> and CO over 5Ni/S-1 and 5Ni/Z100, close to mol% of thermodynamic equilibrium products and stable for 5 h. At the same initial reaction temperature, CO and CO<sub>2</sub> were produced via thermal decomposition. Then, this species was used in water gas shift and steam reforming reactions (Chen et al., 2017). In contrast, the percent yield of CO<sub>2</sub> and CO over 5Ni/Z50 was not stable. This might due complex sub-reaction from various active sites. In low Al support, the reaction progress was related only to the main reaction. As a result,

the amount of hydrogen increases for a longer time, as shown in Figure 5.11c. But in high Al conditions, a side reaction decreased hydrogenation and increased other hydrocarbons (Figure 5.11d-f). The amount of  $\text{CH}_4$  produced over 5Ni/Z50 was higher than 5Ni/Z100, and it was not observed in the case of 5Ni/S-1. Additionally,  $\text{C}_2\text{H}_6$  was only obtained in the reaction over 5Ni/Z50 catalyst.

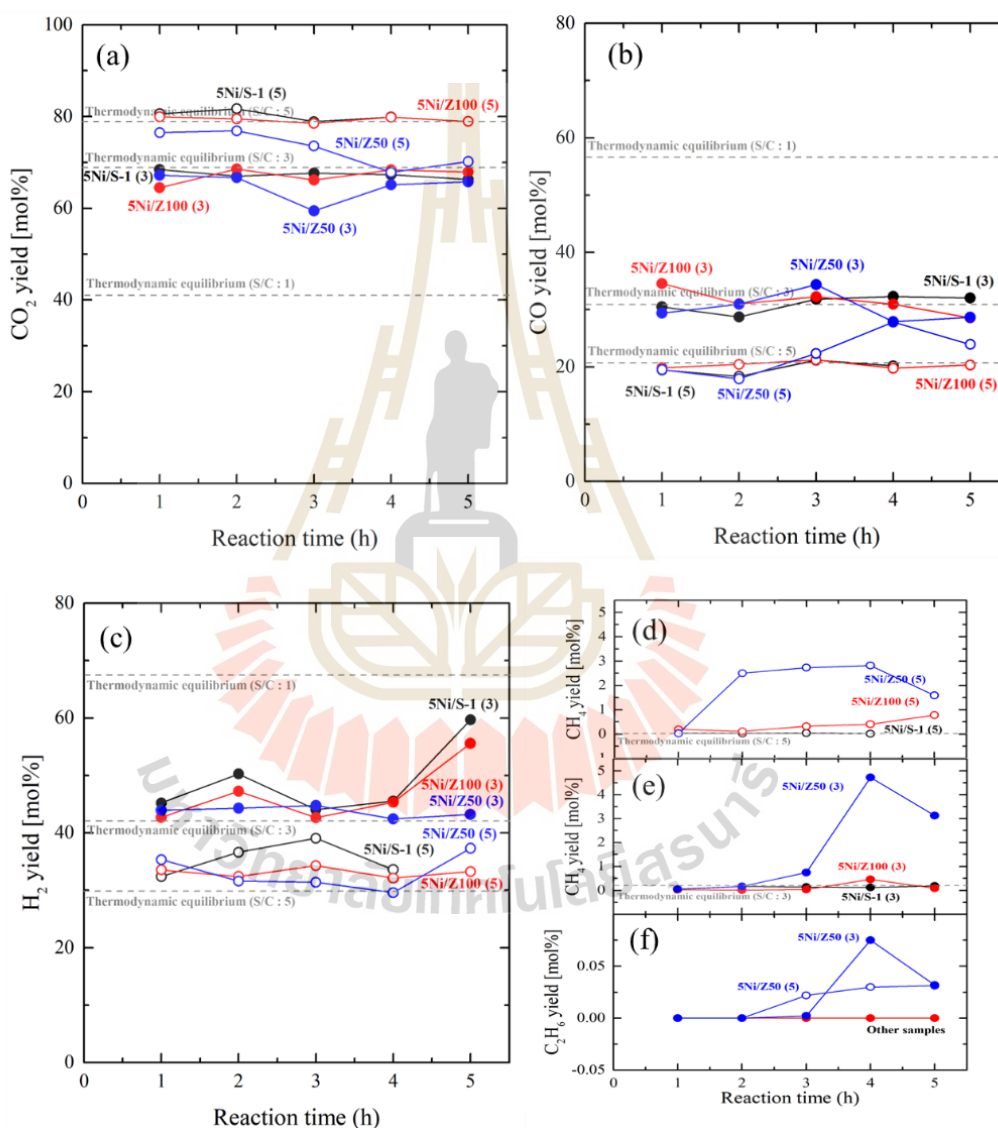


**Figure 5.11** (a) %  $\text{CO}_2$ -yield, (b) % CO-yield, (c) %  $\text{H}_2$ -yield, (d-e) %  $\text{CH}_4$ -yield, and (f) %  $\text{C}_2\text{H}_6$ -yield and the products at thermodynamic equilibrium (----) with different S/C ratio of (5), (3) over 5Ni/S-1, 5Ni/Z100, and 5Ni/Z200 catalysts after testing at 700 °C, 1h.

The change in the S/C ratio resulted in the same trend. However, each S/C ratio gave different product quantities corresponding to the thermodynamic calculated quantities at equilibrium with different amounts of steam. It is well known that steam decreases coke formation, which causes catalyst deterioration. Therefore, the high S/C ratio significantly reduced the byproducts from side reactions compared to the lower S/C ratio.

The weights of spent catalysts as a function of temperature and S/C ratio are shown in Figure 5.12a. All spent catalysts with S/C (5) had a single weight loss at 550 °C: about 0, 1, 17 wt. % for 5Ni/S-1 < 5Ni/Z100 < 5Ni/Z50, respectively. It was from the decomposition of coke (Fujitsuka et al., 2021). S/C (3) showed the same trend, but collective weight loss was higher than S/C (5) about 4, 7, 20 wt. %. The amount of coke formation in Figure 5.12b increased at a high S/C ratio and low Al-content in support. The carbon deposition was not observed in the spent 5Ni/S-1 with S/C (5). Li et al. (2021) explained the coke inhibition by oxidation of carbon with \*OH from water in high steam. Adequate levels of \*OH in the presence of a high S/C ratio promoted the conversion of carbonyl-containing species into gaseous forms, thereby minimizing coke formation. Moreover, the reaction over active zeolites like Z50, containing Al and Na<sup>+</sup> counter cation, promoted the side reaction and produced intermediates (coke precursors) by acidic site and ion-exchange ability (Z. Li et al., 2012).

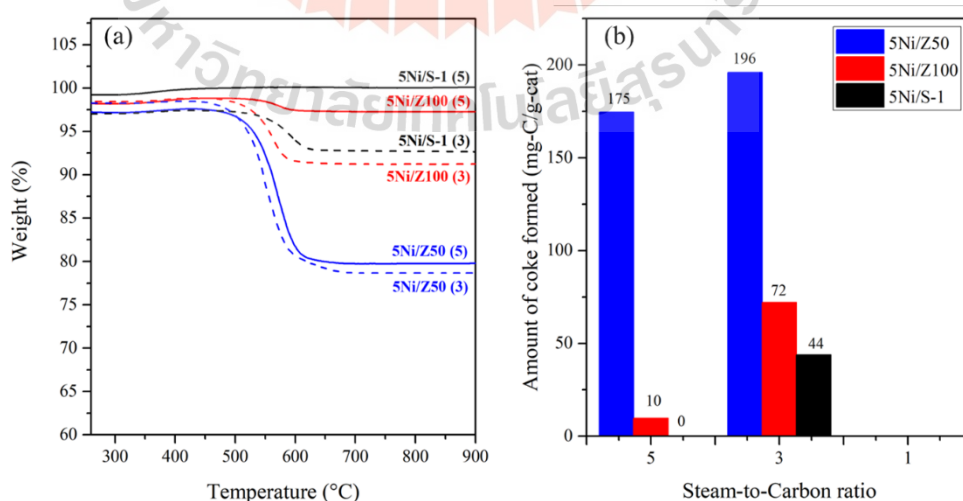


**Figure 5.12** (a) Thermogravimetric analysis (TGA) with different S/C ratio of (5), (3) and (b) carbon deposition on spent catalysts after testing at 700 °C, 1h.

Detailed descriptions of the TEM images of the fresh catalysts can be found in Figure 5.5. Additionally, to gain insights into the characteristics of the Ni particles after reaction testing, a comparison was made with the spent catalysts at various S/C ratios, as depicted in Figure 5.13. Following the examination conducted with an S/C ratio of 5, the aggregation of Ni particles was evident in Figure 5.13d-f. The averaged diameter and volume of Ni particles are presented in Table 5.5. The size of Ni particles tended to decrease with a decrease in Al content due to weaker interaction between Ni and support. Additionally, carbon nanotubes with the smooth outer surface (C. Zhang et al., 2018) was observed solely in the spent 5Ni/Z50 sample, which aligned with the coke quantity determined from TGA analysis.

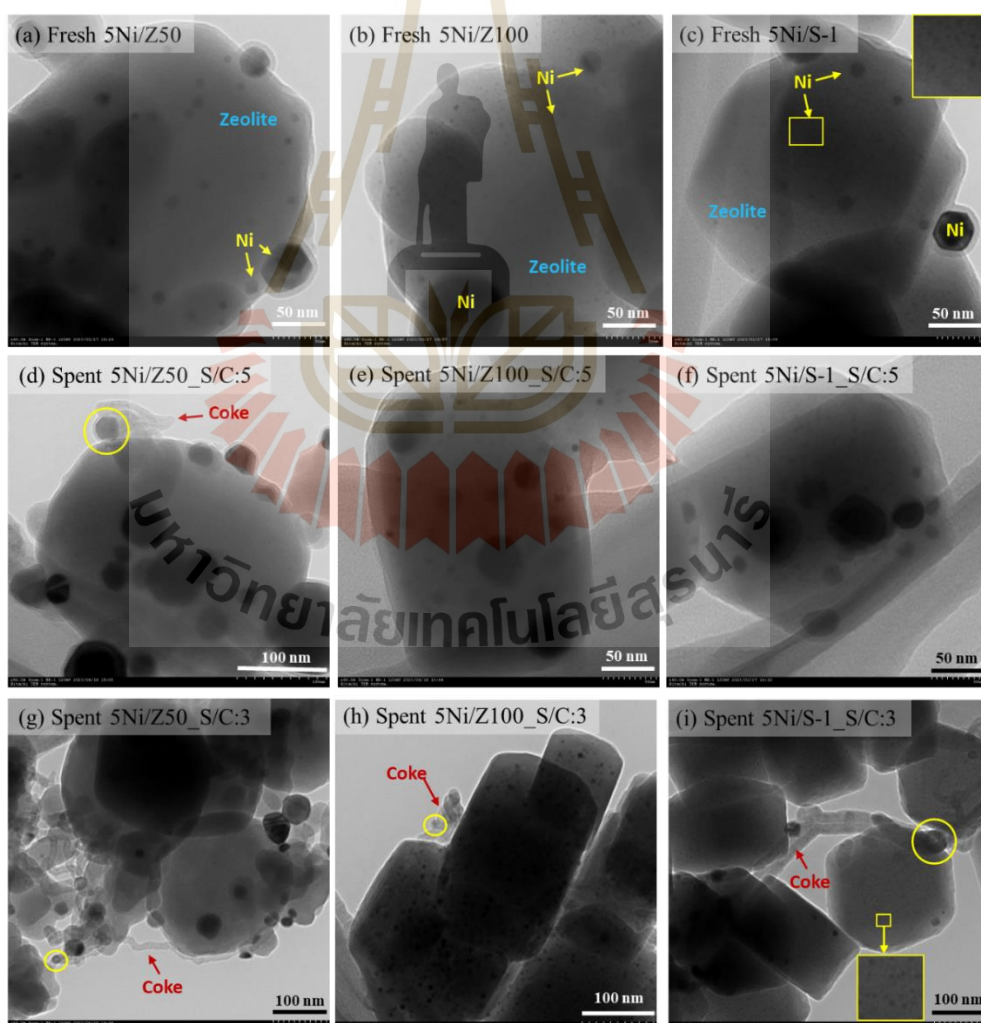


Figure 5.13 TEM images of (a-c) fresh and spent catalyst after testing with S/C ratio about (d-f) 5, (g-i) 3 at 700 °C, 1h.

In the case of S/C ratio of about 3, the size of aggregated Ni in different supports had the same trend as another S/C ratio (Table 5.5). It was observed that the low steam in the system significantly affected the sintering of Ni particles, leading to larger sizes and resulting in catalyst deactivation (Figure 5.13,g-i). Moreover, carbon nanotubes were observed in all spent catalysts corresponding to amounts of carbon. The carbon nanotubes had diverse sizes. Such characteristic could be linked to the distinct dimensions of the varied nickel particles acting as precursors for coke formation at the tips of Ni species in the yellow circles (X. Li et al., 2021).

While 5Ni/S-1 demonstrated remarkable AASR activity at 700 °C and S/C ratio of 5, Ni particle agglomeration occurred in fresh and spent catalysts. This agglomeration contributed to the catalyst deactivation over prolonged reaction periods. Consequently, the impact of Ni loading on its dispersion and AASR performance was further examined.

**Table 5.5** Diameter and spherical volume of Ni nano particles in fresh and spent Ni/MFI catalysts with different S/C ratios of reaction condition at 700 °C.

Sample name	catalyst usage	Steam-to-Carbon (molar ratio)	Ni particle diameter (nm) <sup>a</sup>	Ni particle volume (nm <sup>3</sup> ) <sup>a</sup>
5Ni/Z50	Fresh	-	15.0	7.3 × 10 <sup>3</sup>
	Spent	5	24.5	17.7 × 10 <sup>3</sup>
		3	25.8	19.3 × 10 <sup>3</sup>
5Ni/Z100	Fresh	-	15.6	14.2 × 10 <sup>3</sup>
	Spent	5	18.6	20.0 × 10 <sup>3</sup>
		3	20.0	25.6 × 10 <sup>3</sup>
5Ni/S-1	Fresh	-	11.7	6.1 × 10 <sup>3</sup>
	Spent	5	13.9	4.5 × 10 <sup>3</sup>
		3	15.9	5.3 × 10 <sup>3</sup>

<sup>a</sup>Averaged Ni particle diameter and volume from 100 particles are measured in TEM images.

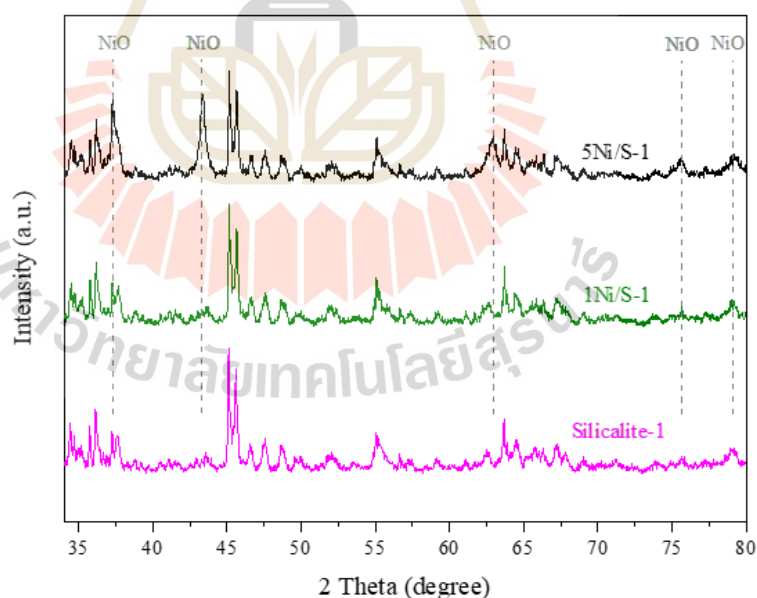
### 5.5.2 Effect of Ni weight

Table 5.6 displays the Ni loading and Si/Ni molar ratio of 5Ni/S-1 and 1Ni/S-1 from XRF analysis. The values corresponded to the initial Ni and Si loading. The zeolite structure remained intact following the metal impregnation process. However, Figure 5.14 reveals the absence of NiO XRD pattern in 1Ni/S-1, indicating the presence of small Ni particle diameters and excellent dispersion of Ni on the zeolite surface (Fujitsuka et al., 2021).

**Table 5.6** Ni loading Si/Ni molar ratio, and Ni particle diameter of 1Ni/S-1 and 5Ni/S-1 catalysts.

Sample name	Ni loading (wt.%) <sup>a</sup>	Si/Ni (mol ratio) <sup>a</sup>
5Ni/S-1	5.4	5.7
1Ni/S-1	1.2	23.8

<sup>a</sup>Averaged % weight of Ni, Al, Si are analyzed by XRF for 3 times.



**Figure 5.14** Powder XRD patterns of silicalite-1 zeolite, 5Ni/MFI, and 1Ni/MFI catalysts.

The catalysts with varying Ni loading exhibit identical  $N_2$  adsorption-desorption isotherms, characterized as microporous type I (Figure 5.15). They also possess similar surface areas and micropore volumes (Table 5.7), although these values

decrease compared to the bare S-1 support. However, the external surface area of 1Ni/S-1 shows a slight reduction compared to 5Ni/S-1, as the weight of the metal decreases.

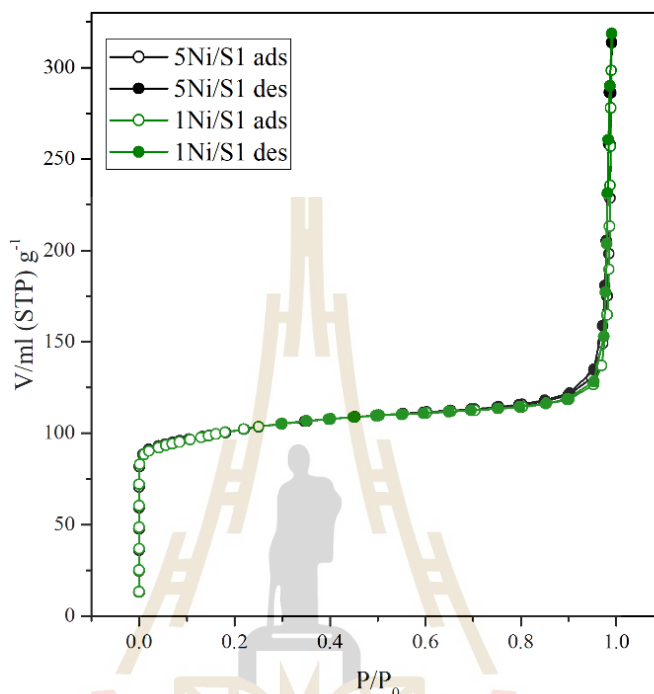


**Figure 5.15** Nitrogen adsorption (ads) -desorption (des) isotherm of 5Ni/S-1, 1Ni/S-1 catalysts.

**Table 5.7** Surface area and micropore volume of 5Ni/S-1 and 1Ni/S-1 from N<sub>2</sub> adsorption-desorption.

Sample name	$S_{\text{BET}}$ (m <sup>2</sup> /g) <sup>a</sup>	$S_{\text{ext}}$ (m <sup>2</sup> /g) <sup>b</sup>	$V_{\text{micro}}$ (cm <sup>3</sup> /g) <sup>c</sup>
S-1	463	25	0.19
1Ni/S-1	386	19	0.16
5Ni/S-1	388	23	0.16

<sup>a</sup> $S_{\text{BET}}$ : specific surface area calculated by the BET method., <sup>b</sup> $S_{\text{Ext}}$ : external surface area calculated by the  $t$ -plot method., <sup>c</sup> $V_{\text{Micro}}$ : micropore volume calculated by the  $t$ -plot method.

The reduction temperatures of both catalysts were compared and illustrated through H<sub>2</sub>-TPR profiles, as shown in Figure 5.16. For 5Ni/S-1, three distinct

stages were observed, corresponding to the reduction of bulk Ni with different sizes at 300 °C, 470 °C, and dispersed Ni at 640 °C, as mentioned in Figure 5.8. In contrast, the peaks from 1Ni/S-1 were at 230 °C, 600 °C, and 835 °C, respectively. This shift suggests a stronger interaction between the metal and support due to the smaller Ni particle size in 1Ni/S-1. Furthermore, the population of Ni species, as indicated by the intensity of the MS signal, differed significantly between the two catalysts due to their Ni loading. The majority of Ni in 5Ni/S-1 existed as bulk, whereas in 1Ni/S-1 dispersed with a stronger interaction with the support.

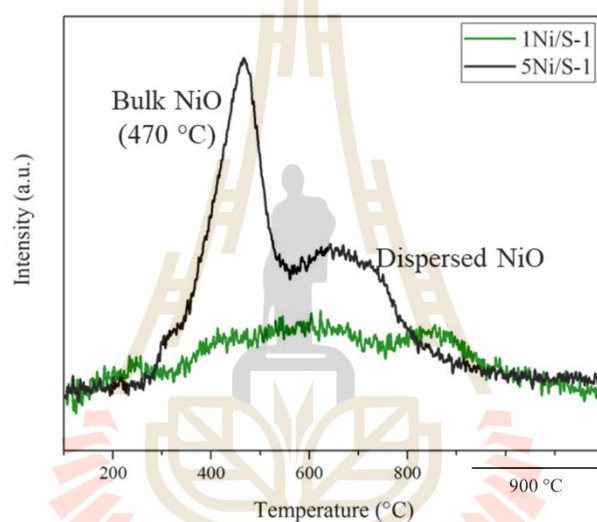
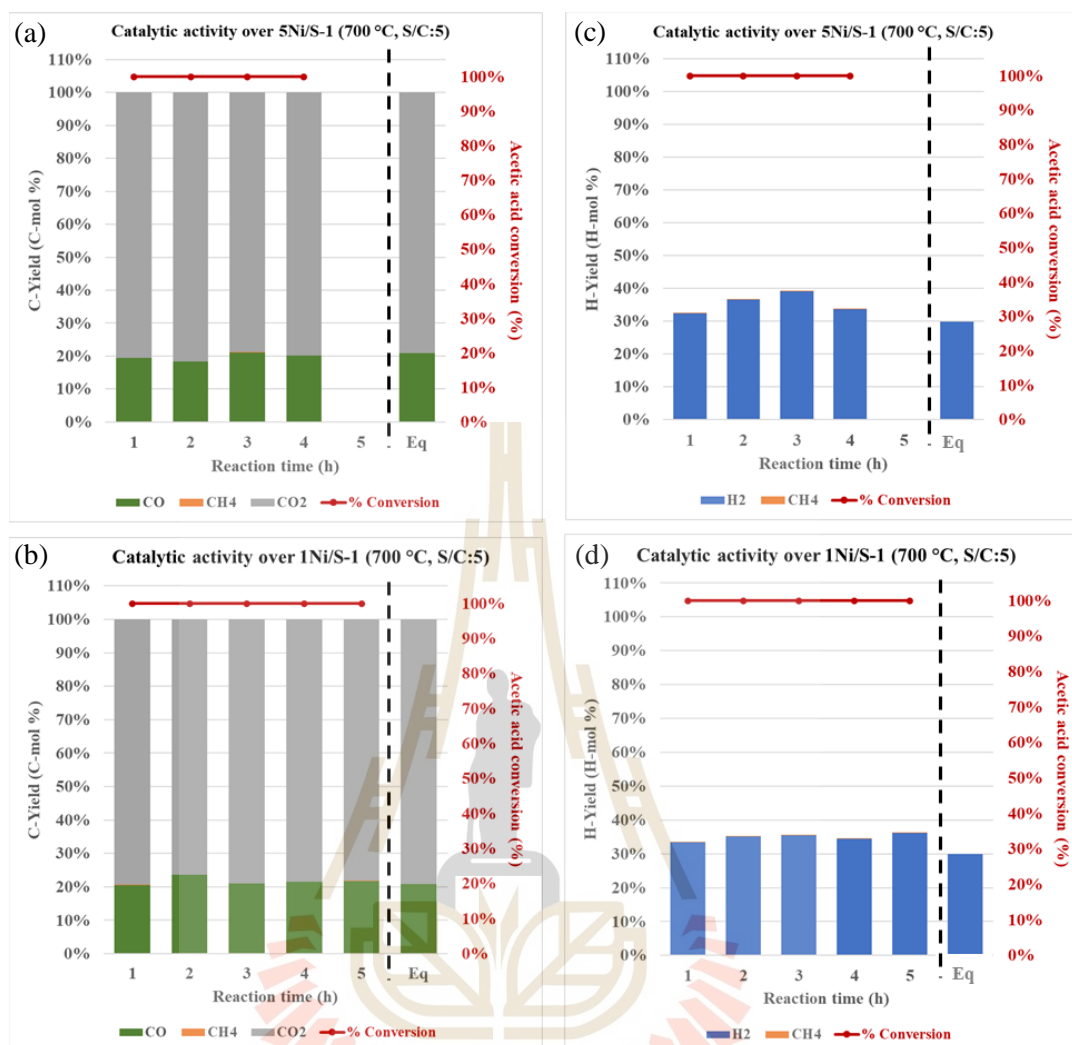


Figure 5.16 H<sub>2</sub>-TPR profiles of 5Ni/S-1 and 1Ni/S-1 catalysts.

Figure 5.17 reveals nearly complete conversions of acetic acid from all catalysts. The resulting gas products were CO, CH<sub>4</sub>, CO<sub>2</sub>, and H<sub>2</sub>, associated with the final products from water gas shift and reforming reactions. Furthermore, the percentages of carbon and hydrogen yields depicted in Figure 5.17a-b and 5.17c-d do not exhibit any significant deviation from the product achieved at thermodynamic equilibrium (Eq). Hence, this observation suggested that the reaction was nearly fully accomplished at 700 °C and a S/C ratio of 5.



**Figure 5.17** (a-b) % C-yield, (c-d) % H-yield over 5Ni/S-1, 1Ni/S-1 catalysts at 700 °C, 1h, S/C: 5, with different reaction time and the products at thermodynamic equilibrium (Eq)

Figure 5.18 compares the TEM images of fresh and spent 5Ni/S-1 and 1Ni/S-1 catalysts. The black spherical of Ni<sup>0</sup> particles dispersed on a coffin-like shape of MFI zeolite (Fujitsuka et al., 2021). While 5Ni/S-1 has three diameters of particles, including large (>30 nm) and middle (6-30 nm) bulk, and dispersed Ni (< 6 nm) as shown in Figure 5.18a, large bulk was not observed in 1Ni/S-1 catalyst as shown in Figure 5.18b. The particle distribution measuring from 100 particles in five TEM images shows the main population diameter range of 0-5 nm in both catalysts with different

numbers. Almost all of the particles of 1Ni/S-1 had diameter in this range. In addition, the largest size and averaged diameter (Table 5.8) of 5Ni/S-1 were higher than 1Ni/S-1, indicating narrow particle size distribution and good dispersion of Ni on the support surface due to the strong metal-support interaction.

After reaction testing, spent 5/S-1 and 1Ni/S-1 catalysts are investigated, as shown in Figure 5.18c-d. Agglomeration of Ni particles was observed in used 5Ni/S-1, while slightly found in spent 1Ni/S-1. The smaller size of the spent 1Ni/S-1 catalyst confirmed a good particle distribution in 1Ni/S-1. However, 1Ni/S-1 had some carbon deposition after the reaction testing. The lower loading of the metal active site produced a small amount of carbon nanotube with a smooth surface. However, it was considered efficient due to its high activity relative to its metal content.

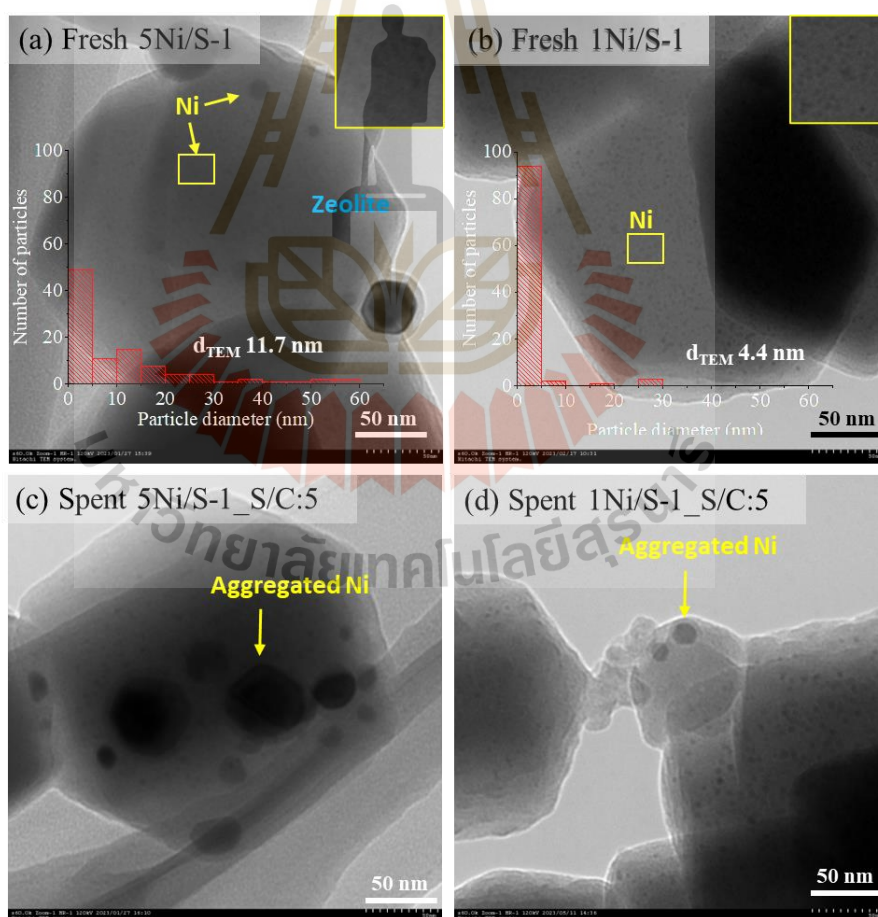


**Figure 5.18** TEM images of (a-b) fresh and (c-d) spent 5Ni/S-1, 1Ni/S-1 catalysts after testing with S/C ratio: 5, at 700 °C, 1h.

**Table 5.8** Ni particle diameter in fresh and spent 5Ni/S-1, 1Ni/S-1 catalysts.

Sample name	Ni particle diameter (nm) <sup>a</sup>		Amount of coke (mg C/1g-cat) <sup>b</sup>
	Fresh	Spent	
5Ni/S-1	11.7	13.9	0
1Ni/S-1	4.4	6.7	35

<sup>a</sup>Averaged Ni particle diameter and volume from 100 particles are measured in TEM images, <sup>b</sup>Measured by TGA analysis.

## 5.6 Conclusion

Ni supported on MFI zeolite through the impregnation method exhibits remarkable performance, yielding a 100% conversion of acetic acid and a 60% H<sub>2</sub> yield, surpassing the amount of H<sub>2</sub> predicted by thermodynamic equilibrium calculations at 700 °C. A low Al content in the zeolite support allows the formation of relative products at a stable rate for up to 5 hours. Moreover, incorporating a highly silicious zeolite with increased steam content in the system tends to lower the production of undesired hydrocarbons and coke formation on the spent catalyst. The carbon deposition was not observed over 5Ni/S-1 with S/C ratio of 5.

The Ni/S-1 catalyst demonstrates enhanced dispersion and smaller Ni particle size, attributed to the strong metal-support interaction. An optimal Ni loading of 1 wt.% significantly reduces the diameter of the fresh catalyst and effectively prevents Ni sintering during reaction testing.

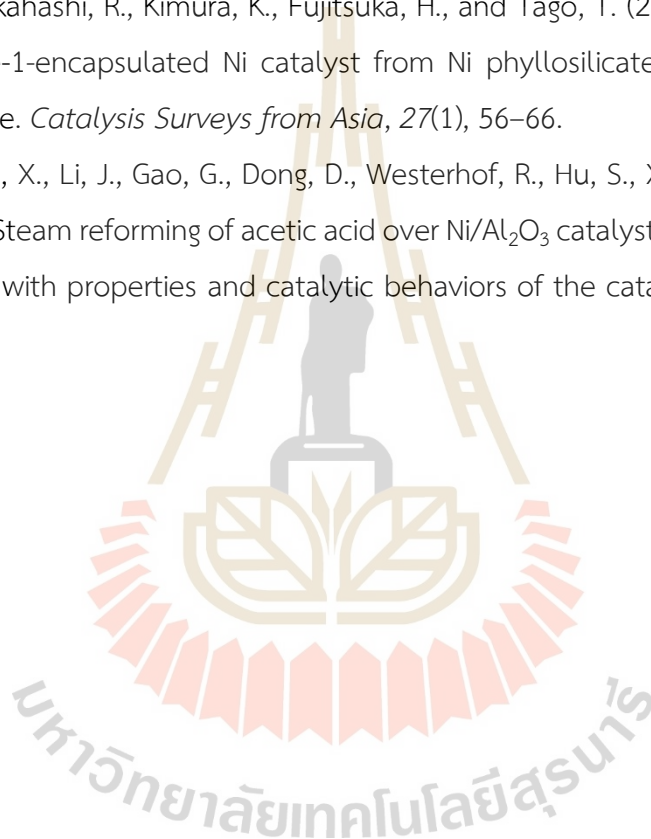
## 5.7 References

- Bacariza, M. C., Amjad, S., Teixeira, P., Lopes, J. M., and Henriques, C. (2020). Boosting Ni dispersion on zeolite-supported catalysts for CO<sub>2</sub> methanation: the influence of the impregnation solvent. *Energy & Fuels*, 34(11), 14656–14666.
- Chen, G., Tao, J., Liu, C., Yan, B., Li, W., and Li, X. (2017). Hydrogen production via acetic acid steam reforming: a critical review on catalysts. *Renewable and Sustainable Energy Reviews*, 79, 1091–1098.
- dos Santos, M. B., Vianna, K. C., Pastore, H. O., Andrade, H. M. C., and Mascarenhas, A. J. S. (2020). Studies on the synthesis of ZSM-5 by interzeolite transformation from

- zeolite Y without using organic structure directing agents. *Microporous and Mesoporous Materials*, 306, 110413.
- FAKEEHA, A. H., KHAN, W. U., AL-FATESH, A. S., and ABASAEED, A. E. (2013). Stabilities of zeolite-supported Ni catalysts for dry reforming of methane. *Chinese Journal of Catalysis*, 34(4), 764–768.
- Fujitsuka, H., Kobayashi, T., and Tago, T. (2021). Development of silicalite-1-encapsulated Ni nanoparticle catalyst from amorphous silica-coated Ni for dry reforming of methane: achieving coke formation suppression and high thermal stability. *Journal of CO<sub>2</sub> Utilization*, 53, 101707.
- Ghasemi, Z., and Younesi, H. (2012). Preparation of free-template nanometer-sized Na-A and -X zeolites from rice husk ash. *Waste and Biomass Valorization*, 3(1), 61–74.
- Guo, L., Li, X. B., Wang, Q., and Wang, S. R. (2012). Steam reforming of acetic acid for hydrogen production: thermodynamic calculations. *Advanced Materials Research*, 534, 141–145.
- Hong, D.-Y., Kim, H. S., Zhang, H., Kang, S. K., Tikue, E. T., and Lee, P. S. (2021). Si-OH nest and Al distribution of silicalite-1 core/Al-ZSM-5 shell zeolites for methane dehydroaromatization reaction. In *Crystals* (Vol. 11, Issue 6).
- Hu, X., and Lu, G. (2010). Comparative study of alumina-supported transition metal catalysts for hydrogen generation by steam reforming of acetic acid. *Applied Catalysis B: Environmental*, 99(1), 289–297.
- Hu, X., Zhang, L., and Lu, G. (2012). Pruning of the surface species on Ni/Al<sub>2</sub>O<sub>3</sub> catalyst to selective production of hydrogen via acetone and acetic acid steam reforming. *Applied Catalysis A: General*, 427–428, 49–57.
- Ibrahim, S. A., Ekinici, E. K., Karaman, B. P., and Oktar, N. (2021). Coke-resistance enhancement of mesoporous  $\gamma$ -Al<sub>2</sub>O<sub>3</sub> and MgO-supported Ni-based catalysts for sustainable hydrogen generation via steam reforming of acetic acid. *International Journal of Hydrogen Energy*, 46(77), 38281–38298.
- Isahak, W. N. R. W., Hisham, M. W. M., Yarmo, M. A., and Yun Hin, T. (2012). A review on bio-oil production from biomass by using pyrolysis method. *Renewable and Sustainable Energy Reviews*, 16(8), 5910–5923.

- Li, X., Zhang, Z., Zhang, L., Gao, G., Wei, T., Zhang, Z., Zhang, S., Chen, G., Li, C., and Hu, X. (2021). Availability of steam impacts coke properties in steam reforming of acetic acid. *International Journal of Hydrogen Energy*, 46(10), 7195–7210.
- Li, Z., Hu, X., Zhang, L., Liu, S., and Lu, G. (2012). Steam reforming of acetic acid over Ni/ZrO<sub>2</sub> catalysts: effects of nickel loading and particle size on product distribution and coke formation. *Applied Catalysis A: General*, 417–418, 281–289.
- Mazaheri, O., and Kalbasi, R. J. (2015). Preparation and characterization of Ni/mZSM-5 zeolite with a hierarchical pore structure by using KIT-6 as silica template: an efficient bi-functional catalyst for the reduction of nitro aromatic compounds. *RSC Advances*, 5(43), 34398–34414.
- Ojeda, M., Osterman, N., Dražić, G., Fele Žilnik, L., Meden, A., Kwapinski, W., Balu, A. M., Likozar, B., and Novak Tušar, N. (2018). Conversion of palmitic acid over Bi-functional Ni/ZSM-5 catalyst: effect of stoichiometric Ni/Al molar ratio. *Topics in Catalysis*, 61(15), 1757–1768.
- Qiao, H., Wei, Z., Yang, H., Zhu, L., and Yan, X. (2009). Preparation and characterization of NiO nanoparticles by anodic arc plasma method. *Journal of Nanomaterials*, 2009, 795928.
- Reeve, J., Mahmud, T., Twigg, M. V., and Dupont, V. (2022). The kinetics of acetic acid steam reforming on Ni/Ca-Al<sub>2</sub>O<sub>3</sub> catalyst. *International Journal of Hydrogen Energy*, 47(84), 35709–35722.
- Wei, L., Haije, W., Kumar, N., Peltonen, J., Peurla, M., Grenman, H., and de Jong, W. (2021). Influence of nickel precursors on the properties and performance of Ni impregnated zeolite 5A and 13X catalysts in CO<sub>2</sub> methanation. *Catalysis Today*, 362, 35–46.
- Xu, S., Slater, T. J. A., Huang, H., Zhou, Y., Jiao, Y., Parlett, C. M. A., Guan, S., Chansai, S., Xu, S., Wang, X., Hardacre, C., and Fan, X. (2022). Developing silicalite-1 encapsulated Ni nanoparticles as sintering-/coking-resistant catalysts for dry reforming of methane. *Chemical Engineering Journal*, 446, 137439.
- Yang, F., Liu, D., Zhao, Y., Wang, H., Han, J., Ge, Q., and Zhu, X. (2018). Size dependence of vapor phase hydrodeoxygenation of m-Cresol on Ni/SiO<sub>2</sub> catalysts. *ACS Catalysis*, 8(3), 1672–1682.

- Yao, D., Yang, H., Chen, H., and Williams, P. T. (2018). Investigation of nickel-impregnated zeolite catalysts for hydrogen/syngas production from the catalytic reforming of waste polyethylene. *Applied Catalysis B: Environmental*, 227, 477–487.
- Zhang, C., Hu, X., Zhang, Z., Zhang, L., Dong, D., Gao, G., Westerhof, R., and Syed-Hassan, S. S. A. (2018). Steam reforming of acetic acid over Ni/Al<sub>2</sub>O<sub>3</sub> catalyst: correlation of calcination temperature with the interaction of nickel and alumina. *Fuel*, 227, 307–324.
- Zhang, Y., Takahashi, R., Kimura, K., Fujitsuka, H., and Tago, T. (2023). Development of silicalite-1-encapsulated Ni catalyst from Ni phyllosilicate for dry reforming of methane. *Catalysis Surveys from Asia*, 27(1), 56–66.
- Zhang, Z., Hu, X., Li, J., Gao, G., Dong, D., Westerhof, R., Hu, S., Xiang, J., and Wang, Y. (2018). Steam reforming of acetic acid over Ni/Al<sub>2</sub>O<sub>3</sub> catalysts: correlation of nickel loading with properties and catalytic behaviors of the catalysts. *Fuel*, 217, 389–403.



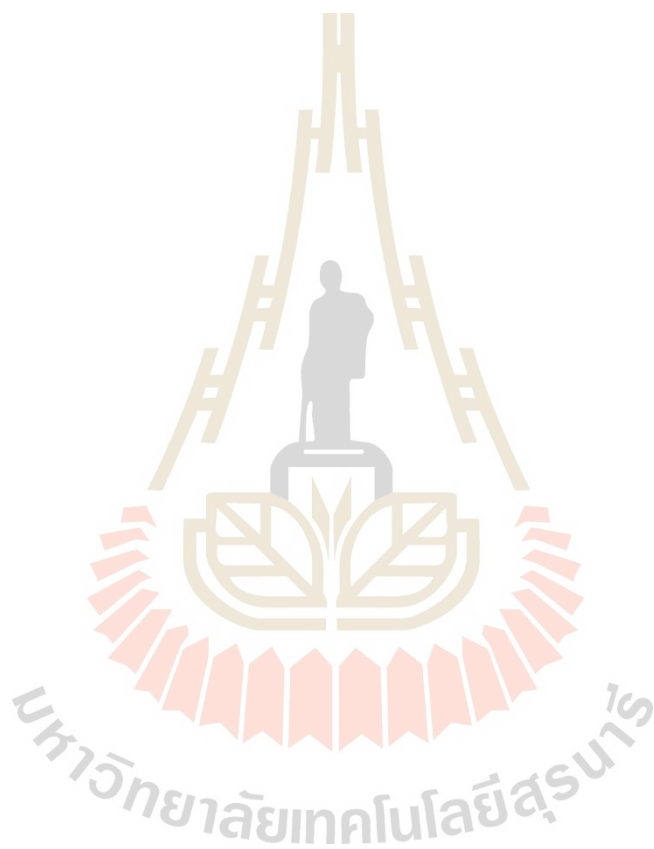
## CHAPTER VI

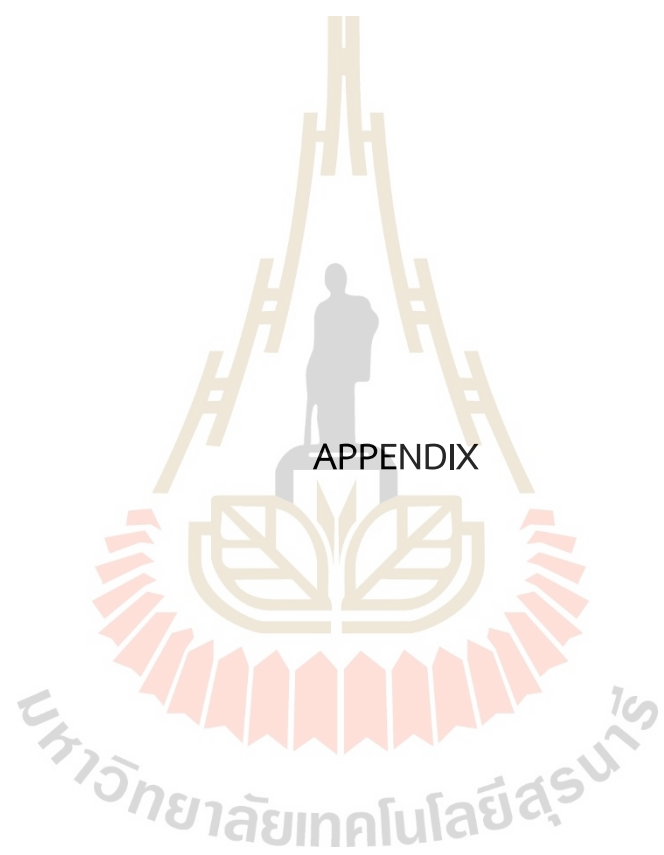
### CONCLUSIONS

Zeolite NaP2 is synthesized from the gel of zeolite NaY by microwave-assisted (MH) and conventional hydrothermal (CH) methods. Microwave provides a pure phase NaP2 from the synthesis in an hour. The catalytic activities of the NaP2 from both heating methods are compared to zeolite NaX in transesterification of palm oil. After impregnation with potassium acetate, both zeolite structures collapse. Aluminosilicate, sodium, and potassium species are leached from the structure and observed on zeolite particles. The collapse increases when sonication is applied in the catalyst preparation. However, MH-catalysts show high performance in the prevention of structure collapse. Although K/MHX has a stronger structure, it provides lower biodiesel yield compared with K/CHX due to different types of carbonate active species and catalyst basicity. Even though K/CHX and K/CHX-U have similar active carbonate specie (free carbonate), K/CHX-U gives a lower yield because of the structure collapse. Noticeably, the yield from the collapsed NaX catalyst is close to the overall activity of zeolite NaP2 catalysts. In the case of NaP2 catalysts, the reaction occurs on the zeolite external surface. Thus, the collapse of the NaX structure forces the reaction to take place only outside the zeolite cavity. That proves the performance of high porosity NaX zeolite.

Furthermore, zeolite catalysts are applied in acetic acid steam reforming (AASR). Five weight percent of nickel dispersed on MFI zeolite is prepared by impregnation. Hydrogen gas was not produced over the bare zeolite. The presence of nickel in catalysts can generate hydrogen gas, and catalytic activity is almost complete at high temperatures, resulting in high acetic acid conversion and hydrogen yield. At a longer reaction time, Si-rich catalyst produce related products which obtain stable rates. It also tends to provide less undesired hydrocarbon product, carbon deposition, and nickel sintering due to the absence of acidic sites and stronger metal-support interaction, respectively. Likewise, increasing steam in reaction testing reduces coke, and it is not observed at the highest ratio of five because of the oxidizing ability of

water. Although siliceous zeolite support improves the mentioned weakness, coke and nickel aggregation are observed in five weight percent of nickel. Finally, decreasing nickel weight to one percent enhances metal-support interaction, resulting in smaller particle size and low nickel aggregation.





APPENDIX

## APPENDIX

### CALCULATION: PRODUCTS IN AASR FROM EXPERIMENT AND PREDICTION AT EQUILIBRIUM CONDITION

#### 1. Calculation of % yield from experiment

The percent yield of products ( $H_2$ ,  $CO_2$ ,  $CO$ ,  $CH_4$ ) obtained from gas chromatography with a thermal conductivity detector (GC-TCD) is determined by comparing the area of each sample with the calibration curve in Figure A-1. Y and X axes are the volume (mL/min) and area of each gas. These are minused with nitrogen carrier gas as, using as internal standard, and results in ratio of volume and area. The other hydrocarbon products, such as methane from gas chromatography with a flame ionization detector (GC-FID) are calculated from the amount of methane in GC-TCD and compare the proportion of gas with mass balance of single carbon and hydrogen.

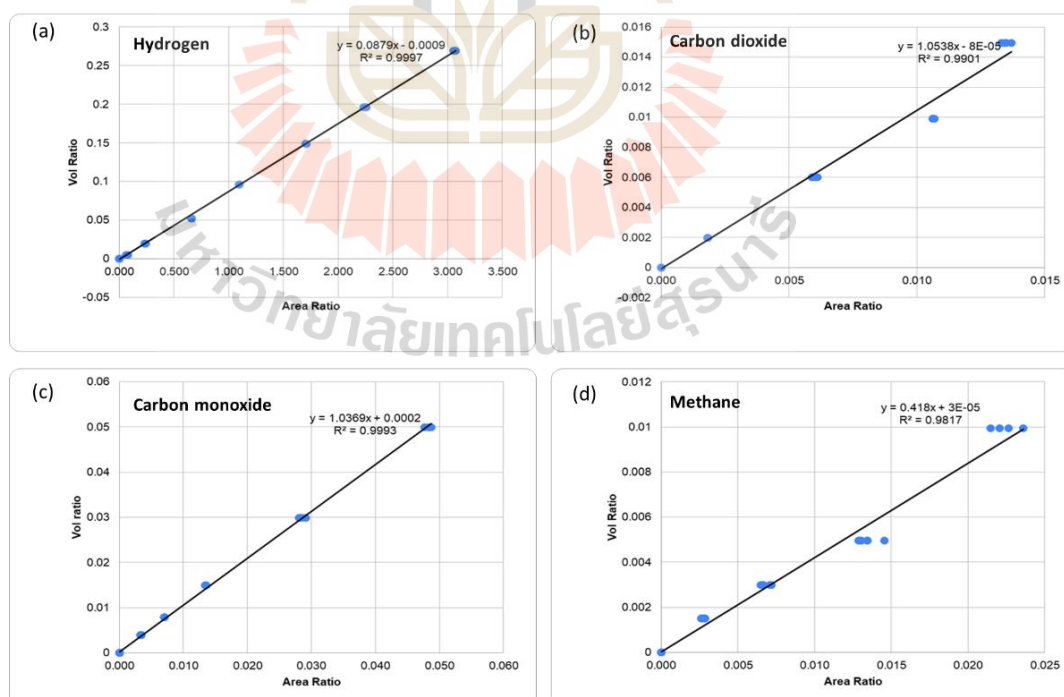
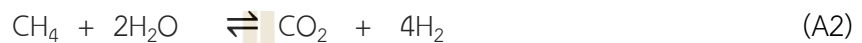


Figure A-1 standard calibration curve of (a) hydrogen, (b) carbon dioxide, (c) carbon monoxide, and (d) methane.

## 2. Calculation of % yield at thermal equilibrium

All acetic acid can convert to products to achieve 100 percent acetic acid conversion that depends on catalytic activity. However, the yield of desired products can be predicted via two main reactions of acetic acid steam reforming reactions: water gas shift reaction (A1) and methane steam reforming (A2), which is a rate-determining step due to the dissociation of CH<sub>4</sub>.



The reaction constant (K) and Gibbs free energy ( $\Delta G_R$ ) of each reaction can calculate following equations A3-A5 by using the data in Table A-1. When A, B, C, D and a, b, c, d are the type and mole of precursors and product from Eq. A1-A2.

$$\Delta G_R = \Delta H_R - T\Delta S_R, \quad dG = -SdT + Vdp \quad (\text{A3})$$

$$\frac{d}{dT} \left( \frac{\Delta G_R}{RT} \right) = \frac{T \frac{d\Delta G_R}{dT} - \Delta G_R}{RT^2} = \frac{-T\Delta S_R - (\Delta H_R - T\Delta S_R)}{RT^2} = -\frac{\Delta H_R}{RT^2} \quad (\text{A4})$$

$$\ln K = \ln K^\circ + \int_{T_0}^T \frac{\Delta H_R}{RT^2} dT = \ln K^\circ + \frac{(\Delta H_R^\circ - \Delta C_{pR,A}T_0 - \Delta C_{pR,B}T_0^2/2 - \Delta C_{pR,C}T_0^3/3 - \Delta C_{pR,D}T_0^4/4)}{R} \quad (\text{A5})$$

$$\times \left( -\frac{1}{T} + \frac{1}{T_0} \right) + \frac{\Delta C_{pR,A}}{R} \ln \left( \frac{T}{T_0} \right) + \frac{\Delta C_{pR,B}}{2R} (T - T_0) + \frac{\Delta C_{pR,C}}{6R} (T^2 - T_0^2) + \frac{\Delta C_{pR,D}}{12R} (T^3 - T_0^3)$$

Subsequently, reaction constant (K) and Gibbs free energy ( $\Delta G$ ) are used to calculate mole fraction (partial pressure,  $p$ ) of each gas at 973.15 K following Eq. A6. The complete reaction should be as Eq. A7. All precursors transform to products with mole fraction of 0.666 and 0.333 for CO<sub>2</sub> and H<sub>2</sub>, respectively. When sub-reactions (Eq. A1-A2) reach equilibrium, the new mole fraction of each gas product is recalculated by the combination of partial pressure of mixed gas (CH<sub>4</sub>, CO<sub>2</sub>, CO, H<sub>2</sub>O, H<sub>2</sub>), which are 0.0072, 0.1365, 0.1944, 0.2088, 0.4531, respectively. If the steam-to-carbon (S/C) ratio on feeding is changed by adjusting water, the partial pressure proportion of gas products should be changed. Percent of H-yield and C-yield are calculated considering as single atoms by Eq. A8-A9, respectively.

**Table A-1** Stoichiometric coefficient, enthalpy change ( $\Delta H$ ), Gibbs free energy ( $\Delta G$ ), entropy change ( $\Delta S$ ), and Heat capacity ( $C_p$ ).

Gas	Stoichiometric coefficient		$\Delta H_f^\circ$ [kJ/mol]	$\Delta G_f^\circ$ [kJ/mol]	$S^\circ$	$C_{p,A}$	$C_{p,B}$	$C_{p,C}$	$C_{p,D}$
	A1	A2							
CH <sub>4</sub>	1	0	-74.905	-50.872	186	19.252	0.052	1.2E-05	-1.132E-08
CO <sub>2</sub>	-1	-1	-393.79	-394.67	213.6	19.796	0.073	-5.6E-05	1.7154E-08
CO	0	1	-110.62	-137.38	197.56	30.871	-0.013	2.8E-05	-1.272E-08
H <sub>2</sub> O	2	1	-242.01	-228.78	188.72	32.244	0.002	1.1E-05	-3.597E-09
H <sub>2</sub>	-4	-1	0.00	0.00	130	27.144	0.009	-1.4E-05	7.6455E-09
Steam reforming (Methaneization)	-2		-165.135	-113.761	-170.16	-44.633	-0.054	1.4.E-04	-6.625.E-08
Water gas shift reaction		0	41.158	28.513	42.68	16.174	-0.094	1.1.E-04	-4.111.E-08

$$K = \frac{\left(\frac{p_C}{p^\circ}\right)^c \left(\frac{p_D}{p^\circ}\right)^d}{\left(\frac{p_A}{p^\circ}\right)^a \left(\frac{p_B}{p^\circ}\right)^b} = \exp\left(-\frac{\Delta G_R}{RT}\right) \quad (\text{A6})$$



$$\% \text{ H-Yield of H}_2 = \frac{\text{Partial pressure of H}_2 \text{ at equilibrium}}{\sum (\text{Partial pressure of H-products} \times \text{H atom})} \times 100 \quad (\text{A8})$$

$$= \frac{p_{\text{H}_2}}{2p_{\text{CH}_4} + p_{\text{H}_2\text{O}} + p_{\text{H}_2}} \times 100$$

$$\% \text{ C-Yield of CH}_4, \text{CO, CO}_2 = \frac{\text{Partial pressure of CH}_4, \text{CO, CO}_2 \text{ at equilibrium}}{\sum (\text{Partial pressure of C-products} \times \text{C atom})} \times 100 \quad (\text{A9})$$

$$= \frac{p_{\text{CH}_4}}{p_{\text{CH}_4} + p_{\text{CO}} + p_{\text{CO}_2}} \times 100$$

Furthermore, another easy way to calculate yield of gas products at thermal equilibrium is the NASA Computer program CEA (Chemical Equilibrium with Applications). The type and molar ratio of initial chemicals, type of final product, reaction temperature, and pressure are required to complete the calculation.

## CURRICULUM VITAE

**Name** Pimwipa Tayraukham  
**Address** 39/12, Fai Kwang Sub-district, Chiang Kham District, Phayao,  
56110

### Education

2013 - 2016 B.Sc. (Chemistry) with First class honors, Khon Kaen University,  
Thailand  
2017 - present Ph.D. candidate in Chemistry, Suranaree University of  
Technology, Thailand

### Publications

1. **Tayraukham, P.**; Jantarit, N.; Osakoo, N.; Wittayakun, J. Synthesis of pure phase NaP2 zeolite from the gel of NaY by conventional and microwave-assisted hydrothermal methods. *Crystals* 2020, 10, 1–11.
2. Jantarit, N.; **Tayraukham, P.**; Osakoo, N.; Föttinger, K.; Wittayakun, J. Formation of EMT/FAU intergrowth and nanosized SOD zeolites from synthesis gel of zeolite NaX containing ethanol. *Mater. Res. Express* 2020, 7, 75011.
3. Krukkratoke, P.; Keawkumay, C.; **Tayraukham, P.**; Prompiputtanapon, K.; Khemthong, P.; Prayoonpokarach, S.; Wittayakun, J. Strategic Synthesis to Disperse Zeolite NaY in Lead Tree Wood. *Cryst.* 2022, 12.

### Scholarship and Fellowship

2013 – 2022 Science Achievement Scholarship of Thailand (SAST) supported by the Office of the Ministry of Higher Education, Science, Research and Innovation, Thailand  
2022 – 2023 Scholarship for an exchange program at Tokyo Institute of Technology from Suranaree University of Technology, Thailand